POLITECNICO DI TORINO

Master's Degree Thesis in Mechanical Engineering

Design of a rule-based controller for improved electrodynamic levitation system performance

Supervisors

Prof. Nicola AMATI

Dr. Marius PAKŠTYS

Dr. Eugenio TRAMACERE

Candidate

Luca CHIARELLO

December 2023

Abstract

Mankind's willingness for rapid travel has always powered relentless research in transportation. This led to the persistent revolution over a few decades that made it possible for humanity to safely move from one point to another on the planet in a matter of hours. Electrodynamic levitation technology has seen increasing interest over the years for the possibility of being employed in a new revolution of public transportation. Hyperloop TT has envisioned a maglev technology based on passive magnets arranged in a Halbach array arrangement. The use of only passive components renders the concept particularly appealing from the energy consumption and the reliability standpoint. Furthermore, the use of Hyperloop capsules inside near-vacuum tubes allows for nearly friction-less movement and very high speeds. However, electrodynamic levitation shows inherent instability when used to levitate a single degree of freedom system. Instability problems are solved by separating the levitated body into two masses. Regardless, external excitations such as ground irregularities or even changes in track slope may result in unwanted oscillatory behavior that, if not controlled, may result in an unpleasant ride for passengers. In this context, this thesis work aims to investigate the dynamic identity of an electrodynamically levitated system by resorting to a quarter car model in order to study its stability, and the effects that variations in the major parameters produce on its dynamic behavior. Subsequently, the main focus is to improve passenger ride quality by developing a controller based on fuzzy logic, proving the effectiveness of such control approach on a levitated system. Control will be materially exerted by a voice coil actuator whose quickness in responding to rapidly changing input signals renders it particularly well suited for the job. Conventional fuzzy logic controllers are designed to work on a specified range of inputs which is rarely supposed to exceed predefined bounds. In a real context, however, given the possibility for random inputs to occur, it is not feasible to solely rely on an estimated range of variation of inputs and it is even less feasible to define fuzzy membership functions over a very broad range as the number of rules would grow exponentially. It is for this reason that a novel approach to fuzzy logic control is presented, which involves real-time estimation of the magnitude of the phenomena in order to dynamically re-scale the rules associated with the fuzzy controller and ensure a consistent and constant level of control resolution. The extensive use of lookup tables and the necessity for small sets of rules paves the way to heavy optimization. Moreover, working with normalized fuzzy control spaces renders it possible to develop an algorithm to train a fuzzy inference system starting from the behavior of another one, essentially translating the actions taken by the training system into rules based on different input states. This approach becomes particularly convenient when only a restricted number of states are known in real-time and when they do not allow for an easy and reliable definition of fuzzy rules. The information provided to the fuzzy controller is enriched by state estimations obtained from a Kalman filter that has been optimized to operate with a reduced form of the mathematical model representing the system.

Acknowledgements

Desidero anzitutto ringraziare il Professor Nicola Amati per avermi dato l'opportunità di sviluppare questo stimolante progetto di tesi.

Un grazie speciale è rivolto a Marius Pakstys per il suo costante supporto durante lo sviluppo di questa tesi e per il suo infaticabile entusiasmo che ha alimentato ogni fase di questo lavoro.

Non posso non esprimere la mia più profonda gratitudine ai tre pilastri più importanti della mia vita: mia madre, mio padre e mio fratello. Con il loro costante sostegno e incoraggiamento hanno reso possibile ogni passo di questo lungo e tortuoso percorso accademico. Senza di loro, questo traguardo sarebbe stato irraggiungibile. Grazie per essere, oggi come sempre, la mia più grande fonte di ispirazione.

Un caloroso ringraziamento si estende anche a tutti i familiari, vicini e lontani, che sono stati a mio fianco, grazie a tutti gli zii e i cugini.

Non posso non ringraziare, poi, tutti quanti i miei amici, coloro che ho conosciuto prima e durante questo viaggio. La loro amicizia sincera è stata determinante per superare ogni sfida.

Infine, un ringraziamento molto speciale è rivolto al compianto professor Elvio Bonisoli, il quale mi ha trasmesso la sua gioia di imparare e di vivere ed il cui ricordo e insegnamenti continueranno a ispirarmi e rimarranno per sempre indelebili nella mia vita.

First and foremost, I wish to express my gratitude to Professor Nicola Amati for giving me the opportunity to undertake this stimulating thesis project

A heartfelt thanks is owed to Marius Pakstys for his unwavering support during the development of this thesis and for his tireless enthusiasm that fueled every stage of this work.

I want to express my deepest gratitude to the three most significant pillars in my life, my mother, my father and my brother. I acknowledge that their constant support and encouragement have made every step of this long and challenging academic journey possible. Without them, this achievement would have been unattainable. Thank you for being, as always, my greatest source of inspiration. A heartfelt thanks also extends to all my relatives, near and far, who have stood by my side. Thanks to all my dear uncles and cousins for their support

I want to thank all my friends, those I met before and during this academic journey. Their genuine friendship has been crucial in overcoming every challenge

Finally, a very special thanks goes to the late Professor Elvio Bonisoli, who shared with me his joy for learning and living. His memory and teachings will continue to inspire me and will remain indelible in my life

Table of Contents

List of Tables

List of Figures

Nomenclature

L	Inductance component of the electric circuit	H
R	Resistance component of the electric circuit	Ω
E	Back electromotive force (BEMF)	V
E_d	Direct component of BEMF	V
E_q	Quadrature component of BEMF	V
i	Current flowing in the electric circuit	A
i_d	Direct component of the current	A
i_q	Quadrature component of the current	A
ω_p	Pole frequency of electrodynamic circuit	$\mathrm{rad\,s^{-1}}$
ω	Excitation frequency	$\mathrm{rad\,s^{-1}}$
Λ	Flux linkage	Wb
Λ_0	Amplitude of flux linkage	Wb
z_p	Unsprung mass vertical displacement (air gap)	m
$z_{p,0}$	Nominal unsprung mass vertical displacement (nominal air gap)	m
v	Longitudinal velocity	$\mathrm{m\,s^{-1}}$
γ	Magnetic pole pair pitch ratio	m
F	Force (with the subscript specifying the type)	N
N_b	Number of branches in the equivalent electrodynamic circuit	-
m_s	Sprung mass of the quarter-car model for the system	kg

m_p	Unsprung mass of the quarter-car model for the system	kg
m_t	Total mass of the quarter-car model for the system	kg
k_s	Intermediate suspension stiffness	$\mathrm{N\,m^{-1}}$
c_s	Intermediate suspension damping coefficient	$\mathrm{N\,s\,m^{-1}}$
c_{sky}	Skyhook damping coefficient	$\mathrm{N\,s\,m^{-1}}$
c_{gr}	Groundhook damping coefficient	$\mathrm{N\,s\,m^{-1}}$
z_R	Vertical road profile at a spatial coordinate	m
A_R	Amplitude of road profile	m
Ω	Spatial frequency or wave number	$\mathrm{rad\,m^{-1}}$
Ω_0	Reference spatial frequency or wave number	$\mathrm{rad\,m^{-1}}$
x	Longitudinal distance	m
x_0	Longitudinal distance travelled	m
λ	Wavelength	m
λ_f	Wavelength for filter in ISO profile generation	m
λ_f	Frequency for filter in ISO profile generation	Hz
t	Time	s
Z_{HA}	Vertical displacement of Halbach array on the HTT test track	m
Z_D	Amplitude pertaining to mechanical loading	m
λ_L	Wavelength pertaining to mechanical and thermal loading	m
$Z_{\Delta T}$	Amplitude pertaining to thermal loading	m
Z_S	Amplitude pertaining to effect of linear synchronous motor	m
λ_S	Wavelength pertaining to effect of linear synchronous motor	m
$\Phi(\Omega)$	One sided power spectral density (PSD)	$\mathrm{m^2/(rad/m)}$
ξ	Spatial shift pertaining to auto-correlation function	m
$R(\xi)$	Auto-correlation function in spatial domain	$\mathrm{m^2}$

σ^2	Variance of random profile	m^2
$\Delta\Omega$	Wave number discretisation	$\mathrm{rad\,m^{-1}}$
N	Number of sine waves or wave numbers	-
w	Waviness	-
A_i	Amplitude of sine wave in sinusoidal approximation	m
G_r	Roughness coefficient	$\mathrm{m\,rad}$
$TF(s)$	Transfer function for ISO profile generation	-
J	Quadratic cost function	$\mathrm{E\,U}^2$
$\boldsymbol{x}$	State vector	E U
u	Control input	N
R	Control input penalisation	-
r	State penalisation	-
$\boldsymbol{K}$	State gain matrix	N/E U
k_p	Equivalent stiffness of pad	$\mathrm{N\,m^{-1}}$
z_s	Sprung mass vertical displacement	m
$\dot{z}_s$	Sprung mass vertical velocity	$\mathrm{m\,s^{-1}}$
$\ddot{z}_s$	Sprung mass vertical acceleration	$\mathrm{m\,s^{-2}}$
$\dot{z}_p$	Unsprung mass vertical velocity	$\mathrm{m\,s^{-1}}$
B_r	Remanence flux of permanent magnet	T
μ_{pm}	Recoil permeability of permanent magnet	-
ρ_t	Resistivity of track	Ωm
z_{in}	Input profile	m
D_t	Average diameter of test bench track	m
L_p	Length of pad with Halbach array	m

Chapter 1

Introduction

1.1 History

The first pioneering efforts aimed at finding suitable technology for rapid transportation can be traced back to no less than the belle époque, an era marked by significant advancements in travel and the development of grand transatlantic steamships and railway systems. The concept of vactrain was conceptualized by Robert Goddard in the same era in the early 1900s[1] . Goddard envisioned the potential for swift connections between great Britain and the United States, connection that was at the time dominated by very slow steam ships which, avoiding misinterpretation, were already engineering marvels for their time. Remember that in those years the world of transportation was much different than what we know now. Even if they were real marvels and often used as flags to testify the power of the nation they were from, ships still used to sink quite often and by the way the sea wasn't and isn't a safe place to be both then and now. The main transportation mean for commutation on land was yet railed transportation which guaranteed safety, "speed" and reliability for the time. Thus, during those years, trains remained the optimal, quickest and most dependable means of travel from one point to another, given that they tralveled on land. Airplane transportation was still a vision, with the first flight taking off in 1906 through the pioneering efforts of the Wright brothers. By any means, it was at the time unimaginable that this entirely novel and unreliable-looking flying machine would become the predominant mean of transportation. Many regarded the flying machine as too dangerous and, for many years, it was. Planes remained in the domain of the military and of the wealthy for quite a period. Despite the scarce confidence in the aviation world, it is very important not to be mislead. It was a fact during this era that human kind was deeply fascinated by flying ships, better known as zeppelins that started to gather increasing attention.

The constant seek for innovation also interested the already well established railway transportation. Engineers of the time had a multitude of new concepts in this field. Among the visionary ideas, the one conceptualized by Goddard, the "vactrain", stands out by all means as the ancestor of modern Hyperloop technology. In Goddard's vision, the "vactrain" would have achieved speeds of up to 1600 km/h. To put it into perspective, during that era, conventional trains were far from reaching the significant milestone of 100km/h. It is easy to imagine that Mr Goddard may have drawn inspiration from the fusion of two well-established technologies of his era. Firstly, the railway, and secondly the pneumatic post system which was in widespread use during his time and which involved delivering mail inside pods or capsules that traveled within tubes, driven forward by air pressure differential. (Pneumatic post was also subject to an hypothesis to be converted in to passenger transport in 1799 by George Medhurst but was very far away from the concept of vactrain). This ingenious method of efficiently and quickly transporting mail within urban areas would have certainly intrigued someone like Goddard, who was exploring novel ways to revolutionize transportation. Indeed, while Goddard may have drawn some inspiration from the pneumatic post, his concept of the vactrain was significantly different and far more ambitious. The "vactrain" was envisioned to utilize magnetic interaction both for levitation and propulsion as it was able to bypass all the implications involved with friction. The vactrain was designed to operate within vacuum tubes, effectively eliminating air resistance. The knowledge about his work came out only after his death when his projects were found. It is indeed a matter of some regret that this early anticipation of such groundbreaking technology remained confined within the pages of Mr. Goddard's notebook, particularly considering that he was just a university student when he first envisioned it. The concept reappeared in the 1930s when the two german engineers Hermann Kemper and Emile Bechelet, brought the idea back to life. During this period they patented the groundbreaking concept of electro-dynamic suspension which is by the way the main subject of interest of this thesis.

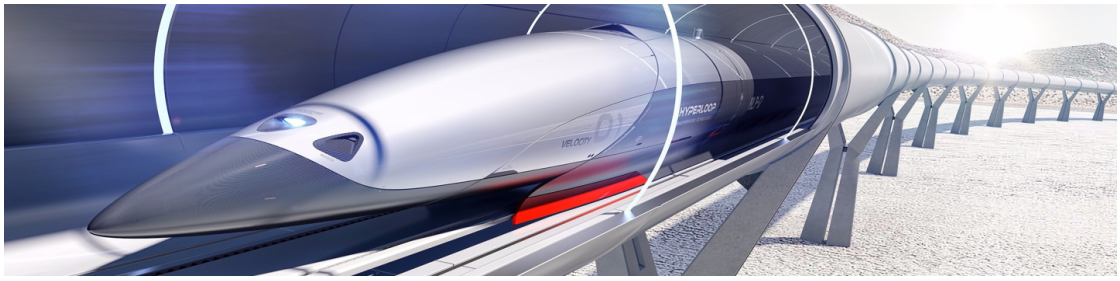

Figure 1.1: Hyperloop capsule rendering. Source: www.hyperlooptt.com

This innovative method hinged on the utilization of superconducting magnets

and electromagnetic induction. It not only allowed for the levitation of the train but also provided the means for propulsion. The induction of EDS marked a significant leap forward in MagLev technology, bringing the dream of high-speed, friction-less transportation closer to reality. This early work laid the foundation for the subsequent developments and advancements in MagLev technology that we witness today. While many application of this novel MagLev technology emerged all over the world, Japan was the one nation that truly took the lead in advancing this innovative mode of transportation from the very beginning. Remember that at the moment we are referring about MagLev trains that do not make use of vacuum tubes but that anyway laid the technology that will be used in hyperloop tracks.

1.2 Modern days

The pioneering efforts of Japanese engineers in the 1960s marked a significant turning point. The development of the ML100 (Superconducting MagLev) train set the stage for a remarkable achievement. It was in fact some years later, in 1972 that the ML100 completed its first test run, during which it reached the groundbreaking speed of 517km/h. This record breaking speed proved the leading position of the Japanese in the field of MagLev technology and propelled the nation to the front of high speed rail innovation on global scale. The last record, at the time this thesis is being written, was broken in 2015 with the SCMagLev reaching a speed of 603km/h. Almost simultaneously, the German research counterpart was also at work on its own MagLev train, known as "Transrapid System", which found also great success and was introduced in china as the Shanghai MagLev Train (2004). This latter is able to reach speeds of up to 500km/h.

(a) (b)

Figure 1.2: (a) SCMagLev train (Source: Central Japan Railway Company.), (b) German Transrapid in the Shangay MagLev line (Credit: Alex Needham)

Both the Japanese SCMagLev and the German Transrapid, serve as examples of

how magnetic levitation and propulsion technology has already reached remarkable results. SCMagLev line is currently on its way to be constructed with the first opening expected in 2027. Indeed, this form of transportation technology holds the potential for groundbreaking speeds, however, a significant concern arises due to the escalation of air resistance with rising speed, based on the fundamental aerodynamic principles, air drag increases in a quadratic way with speed. In practical terms, this implies that a MagLev train operating at twice the speed of a more conventional railed train like the bullet train has an energy consumption of up to four times due to intensified air resistance. This substantial rise in required energy impacts not only the environmental sustainability of the technology, but also raises concerns over the prospect of it becoming economically convenient. In this context, Hyperloop concept emerges as a promising alternative. The term "Hyperloop" was first heard in 2012 and it was introduced by the south African entrepreneur Elon Musk who initiated research into this concept. Today, the companies "Hyperloop One", "Hyperloop Transportation Technologies" and "Transpod" are carrying on research. Modern day technology offers solutions to the challenges that hindered progress

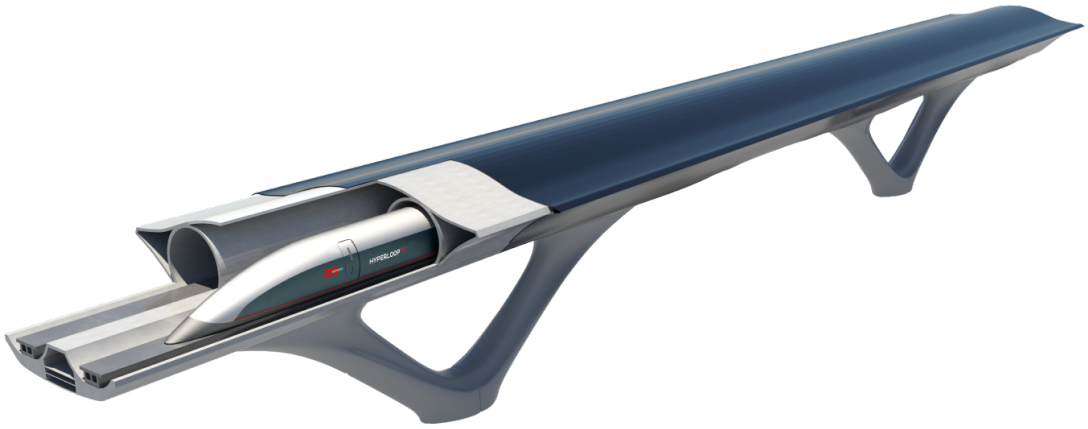

Figure 1.3: Hyperloop TT rendering Source www.hyperlooptt.com

during the early conception of this kind of transportation. These solutions include the development of machinery that is able to mantain low pressure within the tubes and the development and improvement of magnetic suspension technology as mentioned earlier. Hyperloop technology is furtherly fueled by the concept of adopting permanent magnets suspension systems that, unlike super conducting magnets, do not require cooling, since super conductivity is not needed in this context. This makes the system more cost-effective and robust. The application of permanent magnets in electrodynamic suspension is currently subject of research, particularly with the goal of achieving high speed stability through active control

strategies. It is in this very field that this work is going to aim to investigate and contribute to this exciting and rapidly evolving field of transportation technology.

1.3 Technology

1.3.1 Magnetic levitation

While the primary technology employed in the Hyperloop TT project is based on the principle of electrodynamic levitation, it is beneficial to take a closer look at the various MagLev technologies at the current state. First and foremost, when speaking of rail-based vehicles, it is important to acknowledge that operation is based on a fundamental trio of forces: Propulsion, Levitation and guidance as visible on figure 1. This trio is applied, in traditional trains, thanks to geometric

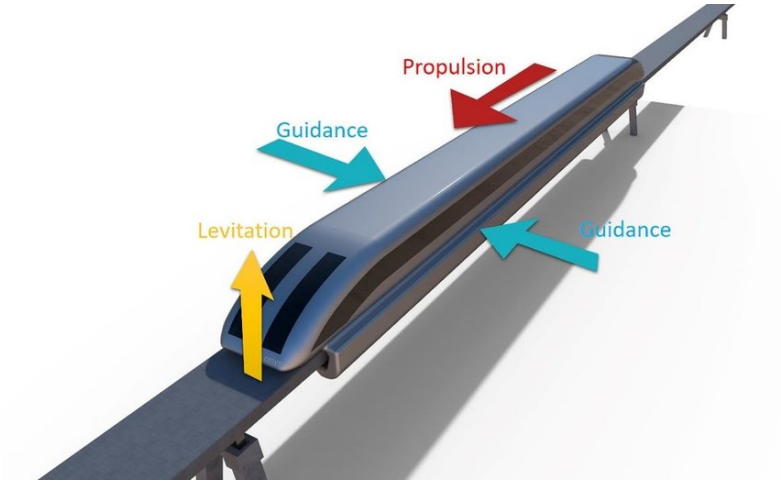

Figure 1.4: Propulsion Levitation and Guidance

contact between the wheels and the rail. In a MagLev train, this actions are guaranteed by magnetic repulsive forces. In the context of MagLev systems, there are three main technologies implied in producing levitation forces and they are summarized as follows [2]:

- Electromagnetic Suspension (EMS)
- Electrodynamic Suspension (EDS)
- Hybrid Electromagnetic Suspension (HEMS)

Electro Magnetic Suspension (EMS)

In an electromagnetic suspension (EMS) system, levitation is achieved by exploiting the acctractive forces between the guideway and electromagnets. However, due to the inherent instability of this system it is imperative to incorporate active control mechanisms to maintain stability. Anyway, it is worth to note that while they require active controls for stability, EMS are of easier implementation with respect to electrodynamic suspension (EDS). On the other hand they result less energy efficient. This technology is capable of levitating the carriage at zero speed, which is physically impossible for an electrodynamic suspension. Typically, the nominal air gap for EMS trains ranges between 10 and 15mm. It is quite trivial to notice that this kind of technology requires some level of electrical current flowing through the electromagnet windings, resulting in some degree of energy loss. The economic and environmental viability of this type of system is indeed significantly impacted by these losses. Reducing these losses by improving design, materials and controls is an important pursuit, and many studies are being conducted on superconducting materials at high temperatures. In an EMS suspension Guidance and levitation electromagnets can be integrated such as in the Korean UTM technology or separated such as in the aforementioned Transrapid German system. The separated technology requires more controls to maintain the air gaps in their nominal range but is more favorable than the coupled counterpart at higher speed due to the reduced interference between guidance and levitation controls [2].

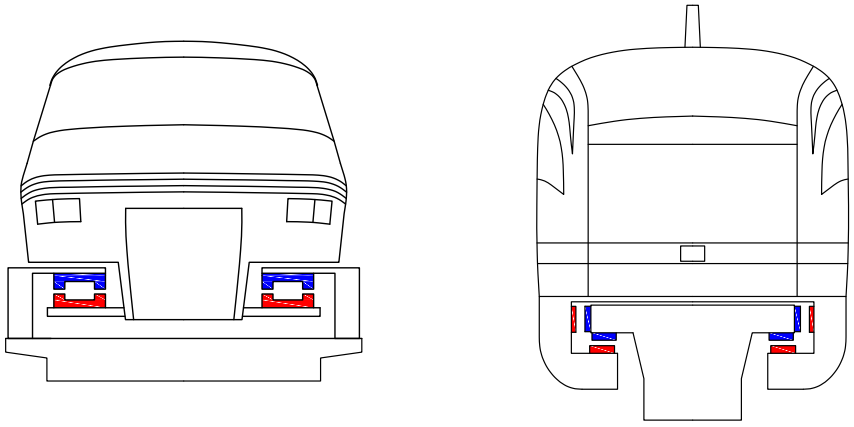

(a) (b)

Figure 1.5: Electromagnetic Suspension (a) Levitation and guidance integrated - HSST system scheme, (b) Levitation and guidance separated - Transrapid system scheme

Electro Dynamic Suspension (EDS)

Electrodynamic suspension (EDS) operates following the principle of induced current within a conductive track. As the carriage, equipped with magnets, moves forward, it exposes the track to a continuous change of magnetic flux. One can envision this continuous conductive track as an infinite series of overlapping conductive rings along the length of the track. While the magnetic field moves together with the pod that generates it, it transitions from one ring to the next. This transition translates in a change of concatenated magnetic flux which, in accordance with Ampere's law, generates an induced current. This induced current, according to Lenz's law, has the effect of opposing to the cause that generated it, thus, an opposing magnetic field will appear and it generates a vertical lift force on the carriage, producing the desired levitation effect. Trains employing EDS technology do typically operate at around 100mm air-gap. This feature makes them very suitable for very high speed operation due to bigger clearance with respect to EMS trains. However, a limitation of EDS trains is the requirement to attain a certain speed before levitation can commence. This is because the repulsive force generated is directly related to the rate of change of the concatenated magnetic flux with respect to the track. To address the issue, retractable wheels, resembling those of airplanes, are installed beneath the carriage and are employed during the initial acceleration phase to allow for speed buildup before the benefits of EDS levitation can be realized[2].

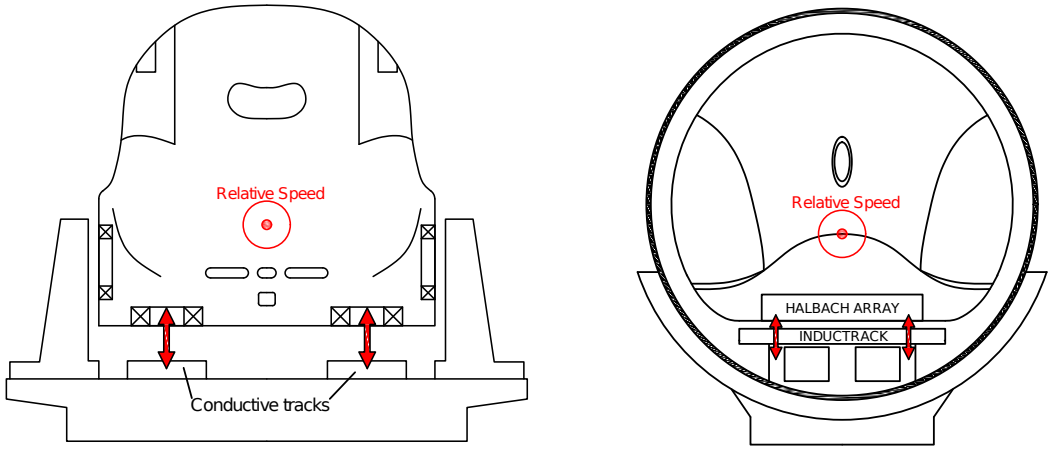

(a) (b)

Figure 1.6: Electrodynamic Suspension (a) using super conducting magnets as the SCMagLev train, (b) using permanent magnets as HyperloopTT capsule

Magnets

The success of electrodynamic magnetic levitation hinges on the strength of the generated magnetic field. This magnetic field can be produced either by using Superconducting Magnets (SCM) or Permanent Magnets (PM). In the case of SCMs, as seen in the SCMagLev levitation system, there's a significant challenge as, currently, there are no materials capable of superconducting at room temperature. Consequently the SCMagLev employs Niobium Titanium electromagnets that have to be cooled with liquid helium to achieve superconductivity. It is trivial to note that this cooling can raise concerns about the economic and environmental sustainability of such a system as the energy resources needed for the continuous cooling of such electromagnets can be significant. Efforts are ongoing in material science to develop materials capable of superconductivity at higher temperatures. This would be a turning point for magnetic levitation and many other fields too. Indeed, a more promising approach would be that of seeing Permanent Magnets employed to obtain levitation. This transition to PM brings numerous advantages that can significantly improve the convenience of MagLev systems. PMs do not require any cooling and neither the flow of any electrical current. This factors make PMs inherently more rugged and a simple technology which would require considerably less maintenance and operate in a more cost effective and ecologic way. In present days, the adoption of PM-based electrodynamic suspension working in Halbach array is being explored. PM EDS is the pivotal technology that will be further focused on in this thesis.

Figure 1.7: Side capsule view source www.hyperlooptt.com

Hybrid ElectroMagnetic Suspension (HEMS)

Hybrid electromagnetic suspension (HEMS) Is a combination of EMS and EDS technology, strategically fused to minimize power consumption. In the HEMS configuration, EMS assists levitation until a certain steady state air gap is reached, at which point, EDS system takes over providing support to the pod independently. A major drawback of HEMS lies in the necessity for HEMS electromagnets to operate at higher current amplitude than those working in EMS systems. This has to be attributed to the permanent magnets having a permeability like air's, thus necessitating a stronger electromagnetic field to achieve the desired levitation effect. [2]

1.3.2 Thrust and Guidance

While this work does not deal with longitudinal nor lateral dynamics in depth, it is still valuable to provide a brief overview of how these types of vehicles move and how they are guided to keep track. The thrust in magnetic levitation trains is achieved through linear induction motors (LIMs) which operate on the same principle as conventional rotary induction motors. The idea at the base is that of unrolling a rotary motor into two magnetic flat sheets that slide past each other as visible in figure 1.8. This configuration together with changing polarity of the track magnets generates a longitudinal force that propels the train. It is important to note, however, that this thesis does not extensively explore the linear actuation technology and, so, the propulsion aspect will not be examined further. It's worth to mention that due to the nearly friction less environment the pods are in, propulsion may not be necessary along the entire track length and could be limited to a partial extent. In addition, as mentioned earlier in this chapter, the

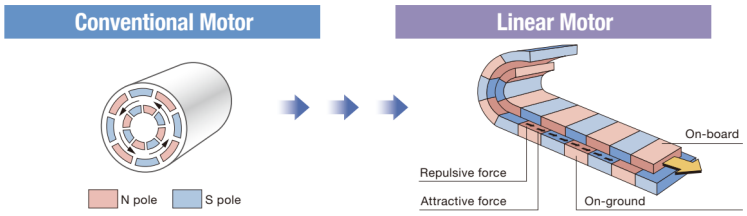

Figure 1.8: Rotary vs Linear motor

guidance system can be integrated with the levitation magnetic circuit or remain uncoupled. The non coupled version of guidance system is preferred for high speed operations as it minimizes interference between guidance gap control and vertical stability control of the pad.

Chapter 2

Mathematical Models For Electrodynamic levitation

2.1 Electrodynamic suspension Modeling

In this section of the work, the primary focus is centered on enlightening the various assumptions that lay beneath the mathematical Modeling of the electrodynamic levitation physics. In this pursuit, [3] and [4] articles will broadly be referred to. The physical foundation employed in this analysis is that of the quarter car model. This kind of model is widely recognized and extensively employed in dynamic modeling of mechanical systems as it effectively well represents the dynamics of wheeled vehicles. The quarter car model approach splits a vehicle separating the masses that belong to the wheel assembly from those that are comprised with the cabin. The latter mass is referred to as "sprung" mass since it is connected to the former "unsprung" mass and, thus, does not feature contact with the terrain. The pursuit of this work is to enhance the passengers' comfort within the sprung mass. Cars' suspension system is represented as a parallel combination of a dashpot and a spring between the sprung and unsprung mass. This configuration has confirmed to truthfully reproduce the behavior of a real shock absorber. With this model is possible to very easily tune the parameters of the suspension in order to get the desired performance at the wanted passenger comfort level. It is important to note that this relatively simple model solely focuses on the vertical vehicle's dynamics and does not account for any of the lateral nor longitudinal dynamics. Those latter effects are more comprehensively addressed in more advanced models. It is worth to evidence that these more advanced models are not aligned with the scope this work is aiming to, scope that revolves around achieving vertical dynamic stabilization. In addition, given the interest for active control, while larger scale models could potentially provide more comprehensive results, they may not be

feasible for live experimentation.

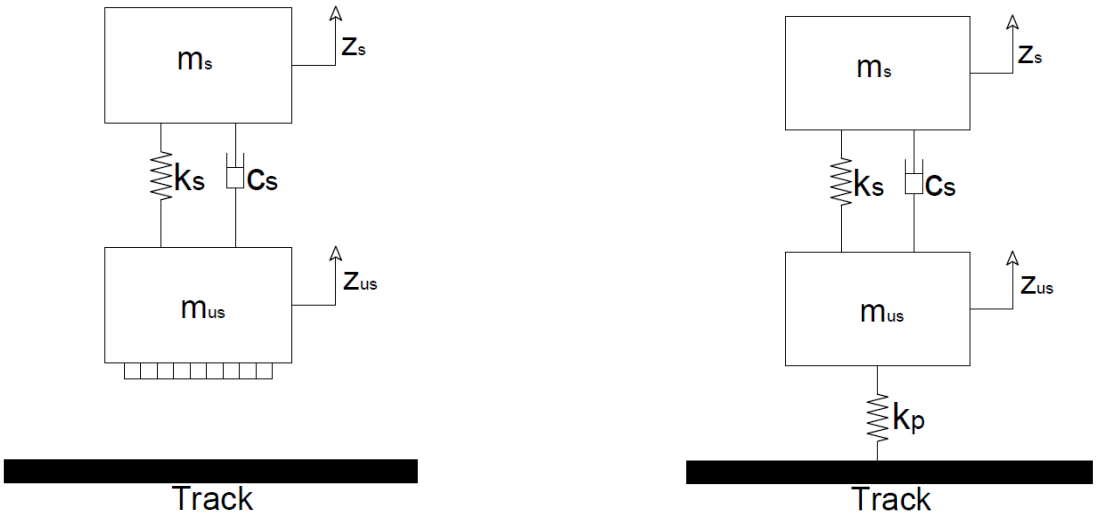

(a) (b)

Figure 2.1: (a) Passive EDS suspension modeled with a QCM, Includes the non linear lift force generated by the interaction of the Halbach array with the track. (b) Simplified version of QCM using a linear spring instead of levitation physics

Some words must now be spent on how to apply a model which is proper of wheeled vehicles to something that does not even feature wheels, which is instead levitating on a magnetic cushion.
Classical quarter car models traditionally feature a spring connection between the unsprung mass and the ground. This component is particularly well suited for representing the vertical dynamics of a pneumatic. The quarter car model (from now on referred to as QCM) is a relatively simple 2 degree of freedom system. Its equations of motion yield a pair of second order differential equations with constant parameters. These equations, in turn, produce a dynamic matrix that remains valid at all speeds. However, an EDS system, as introduced in Chapter 1, can only provide support to the carriage above a certain speed range. Consequently, any element used to connect the unsprung mass with the ground must exhibit varying characteristics. The complexity is further enhanced by non-linearity of these characteristics. Therefore, linearization becomes a necessity, and it must be confined to a very well specified point of the velocity-lift curve and hold for a very small range around that point. To have a glance on the meaning of the previous sentence is useful to look at Figure 2.2. Heavy non linearity subsists in the low speed range for all air gaps. While at higher speed, lift appears to be more linear.

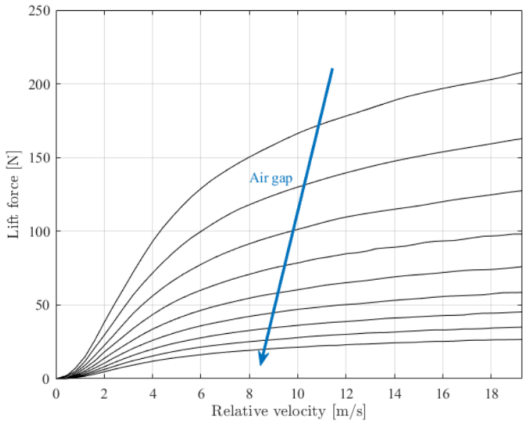

Figure 2.2: Lift force vs relative velocity plot for varying air gaps

2.2 Halbach array

Before moving into the discussion of the problem's dynamics, it is beneficial to introduce the characteristics of the levitation pad, which plays the most important role in the entire system's operation. An Halbach array is an arrangement of permanent magnets assembled in such a way that the mutual interaction between each magnetic field results in a significantly higher magnetic flux density on one side than on the other. This is accomplished by adopting a specific magnetization pattern for each magnet within the array. It must be specified that magnets in an Halbach configuration are not in a state of equilibrium when arranged together. If left unconstrained, they would naturally align themselves so that each pole of a magnet touches the opposite one of the fellow one. Thus, to maintain the Halbach array's desired effect, these magnets are secured in place to constrain motion, typically through adhesive bonding or other methods. Halbach arrays find applications in various fields, including brush-less DC motors, voice coils and particle accelerators. However, the most interesting application, particularly in the context of this work, lies in its usefulness in achieving electrodynamic levitation.

While it's theoretically possible to create Halbach array with an infinite number of magnets, with infinitesimally varying magnetization direction, the configurations of practical interest are two. The first involves placing magnets so that the polarization direction is at a 90° angle shift from their neighbors. The second, which is the one adopted in the test-bench, employs a 45° angle of rotation as illustrated in Figure 2.3. As will be seen later in the discussion of the test bench,it's worth noting that the 90° configuration has been utilized for conducting the quasi-static analysis whereas a 45° configuration will be adopted for the purpose of dynamic stabilization.

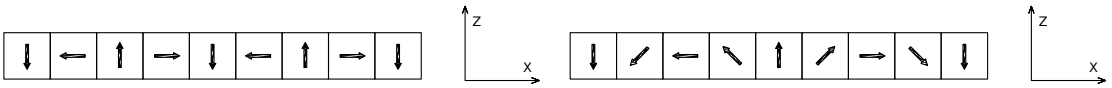

(a) (b)

Figure 2.3: (a) 90 degrees Halbach array (b) 45 degrees Halbach array

2.2.1 FEM Magneto-static Analysis

To achieve a more concrete understanding of what previously stated about the Halbach array, a Finite Element Method (FEM) analysis was carried out using COMSOL Multiphysics. This analysis focused on a 45-degree Halbach array, closely resembling the one employed in the test bench, and exhibiting the parameters listed in Table 2.1[5]

Material	**Parameter**	**Symbol**	**Value**
N45UH-NdFeB	Number of magnets	N_m	8
	Magnet side length	a_m	12.7mm
	Magnet in-plane depth	d_m	63.5mm

Table 2.1: 45 degrees Halbach array parameters used for FEM analysis

In figure 2.4 the lateral view of a 45-degree Halbach array, equivalent to that shown in Figure 2.3 (b) can be observed. The color map illustrates the magnetic flux density norm [T]. It is evident that the flux density is significantly higher beneath the Halbach array compared to the top. The curved shape of the Higher magnetic flux zone is primarily attributed to the limited length of the array. This latter "zone" appears wider in proximity of the central magnets of the array. It is important to underline that the influence of side effects is widely neglected in the following parts, this is equivalent to assume that the array features an infinite in-plane depth, which is indeed far from reality. Thus, in order to provide a more comprehensive view of what happens nearby the edges, Figure 2.5 depicts the top view of the same array in Figure 2.4.

2.3 FEM EDS Modeling

In order to obtain a model for the electromagnetic interaction between the pad and the track, Maxwell equations have to come into play together with Lorents'law.

Notice that in this part equations at the base of the FEM analysis are briefly discussed and they are anyway valid also for the magneto-static analysis performed

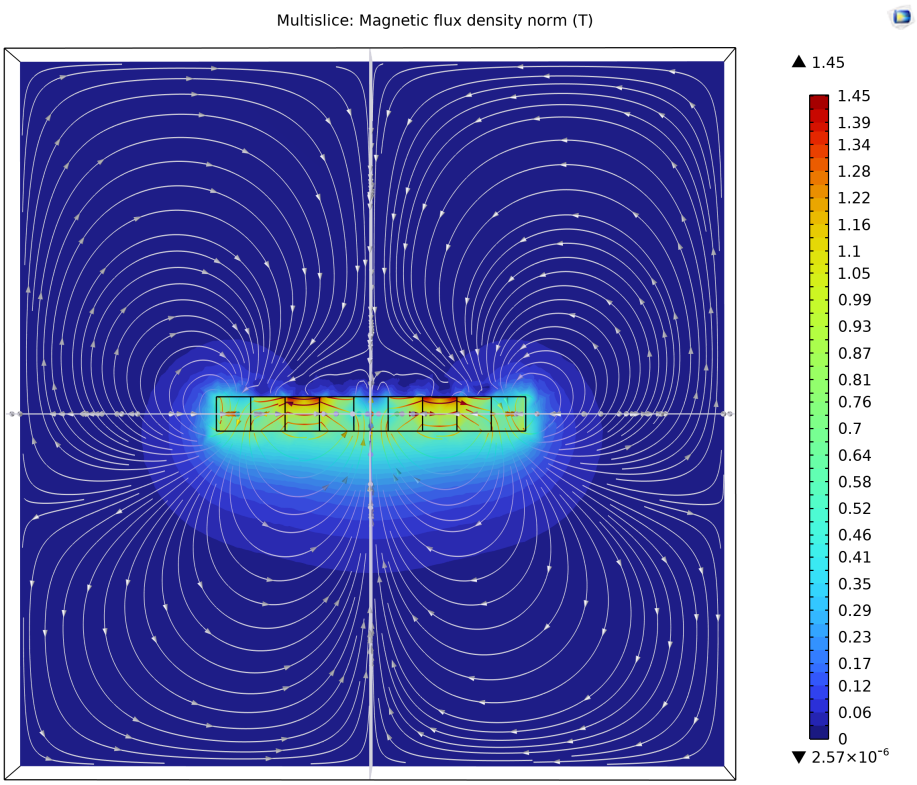

Figure 2.4: Magnetic flux density norm (T) Lateral view.

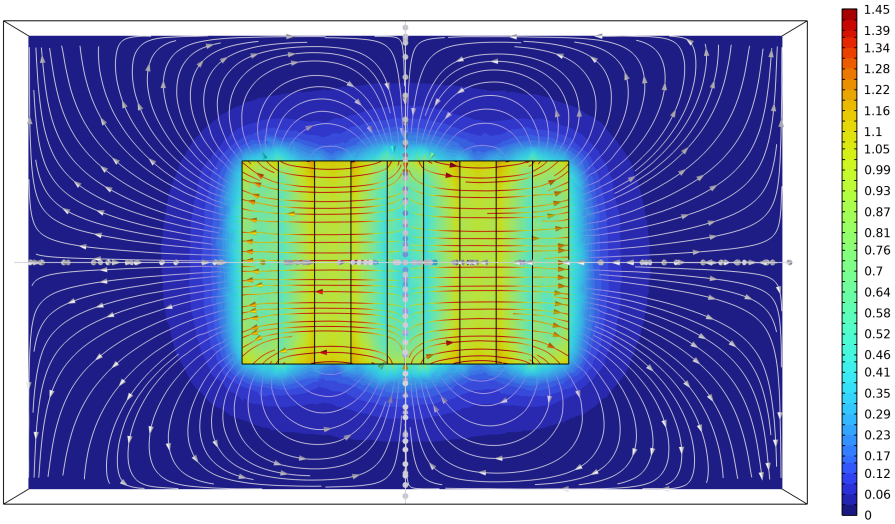

Figure 2.5: Magnetic flux density norm (T) Top view.

for the Halbach magnet array in Figure 2.4/2.5. In that case anyway the Lorent's interaction is nil due to the absence of relative velocities.

Firstly, a magnetic vector potential **A** is introduced. By definition of potential:

$$\boldsymbol{B} = \nabla \times \boldsymbol{A} \tag{2.1}$$

Let's also recall that, by the local formulation of Ampère Maxwell's law:

$$\nabla \times \boldsymbol{H} = \boldsymbol{J} \tag{2.2}$$

Remember that in this context $\boldsymbol{B}$ is the magnetic flux density, $\boldsymbol{H}$ is the magnetic field and $\boldsymbol{J}$ is the current density. The constitutive law for homogeneous isotropic materials relates the magnetic flux density to the magnetic field as follows

$$\boldsymbol{B} = \mu_0 \mu_r \boldsymbol{H} \tag{2.3}$$

Where $\mu_0 = 4\pi \cdot 10^{-7}$ is the magnetic permeability of the vacuum and μ_r is the relative permeability of the mean. The electrodynamic interaction is simulated with the relative movement of the track at velocity $\boldsymbol{v}$ with respect to the Halbach array that is instead fixed. The induction of a current density $\boldsymbol{J}$ within the track is due to the track moving in a magnetic field and is governed by Lawrence forces. Thus, Lawrence's law can be substituted in the place of $\boldsymbol{J}$ in equation 2.2 to produce the following.

$$\nabla \times \boldsymbol{H} = \sigma(\boldsymbol{v} \times \boldsymbol{B}) \tag{2.4}$$

As previously mentioned, the geometry has a sufficiently high in-plane depth to allow neglecting the edge effect of the eddy currents [3]. These equations lay the base to perform a magneto-dynamic analysis, which cannot be performed by hands but requires a FEM approach. Results will allow the effects of the relative movement between the track and the array to be shown and color maps are reported in the paper in [3]. A few words may be spent on the results such analysis has provided. Under the electrodynamic interaction a vertical force facing the $+z$ direction guarantees the levitation above a certain speed, while a drag force arises along the horizontal $-x$, hindering the forward motion. Current density plots were obtained for very low speed ($1m/s$) and high speed ($340m/s$). The low speed simulation shows eddy currents following the shape of the magnetic vector potential and extending to the whole length of the track, while at very high speed the skin effect arises and current density is restricted to a very thin layer of the track facing the magnets.

2.4 Lumped Parameter approach

While conducting such kind of analyses is undoubtedly interesting, utilizing a Finite Element Method approach to model the entire system and then to extract

results for every speed is very resource consuming. Moreover, this approach is not suitable to obtain a state space model representing the real model as it wouldn't allow for a set of equations to be written depending on the state variables. Indeed, when dealing with mechanical system dynamics, a more direct and straightforward approach is looked after. It is actually very common in dynamics to simplify complex systems that could be analyzed using FEM into much more basic systems that can many times reduce the complexity by orders of magnitude. This is precisely why the quarter car model, introduced earlier in this chapter, exists. In fact, just as the QCM simplifies the vehicle suspension, the approach proposed by *Galluzzi*[3] simplifies the electrodynamic interaction ruled by equations 2.4 and 2.1 into the dynamics of a relatively simple RL circuit. The equivalent circuit is

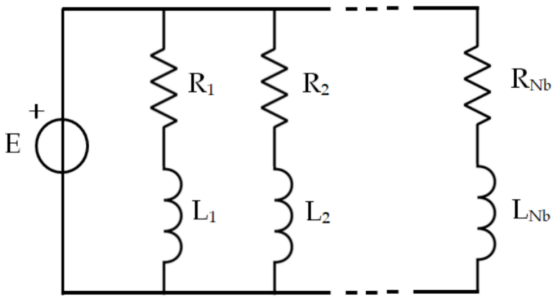

Figure 2.6: Lumped parameter system representing the levitation dynamics

displayed in Figure 2.6. The idea is to approximate the lift and drag force behavior shown in Figure 2.2 by increasing the number N_b of branches. Each one of the branches will be characterized by a different value of inductance L_k and resistance R_k. Although the approach exposed by *Galluzzi*[3] makes use of a number of 3 electrical branches, in *Bosica's* work[5], it was proved enough to use a two-branched electrical subsystem for the speed range of interest. This turns of course beneficial from the point of view of the dimensions on the state space matrices. Being all branches installed in parallel, the following equation holds for a generic k-th branch.

$$L_k \frac{di_k}{dt} + R_k i_k + E = 0 \tag{2.5}$$

The flux linkage term between two orthogonal coils within the track continuum can be expressed as follows

$$\lambda = \Lambda e^{j\omega t} \quad with \quad \Lambda = \Lambda_0 e^{\frac{z_p}{\gamma}} \tag{2.6}$$

Where γ is the pole pitch ratio

$$\omega = v/\gamma \tag{2.7}$$

$$\gamma = \frac{N_m a_m}{2\pi} \tag{2.8}$$

v is the relative speed between the pad and the track and ω is the track's rotational speed, while Λ_0 is the amplitude of the excitation, which was set to one in previous works while tuning the other parameters. Remembering Faraday's law of electromagnetic induction, the Electromotive force produced in the track is equal to the time derivative of the magnetic flux linkage λ expressed in equation 2.6. This Electromotive force is referred to as **B**ack **E**lectro**M**otive **F**orce (BEMF) and has an in phase (α) and a quadrature (β) component given the rotating vector notation that is being exploited.

$$E = \frac{d\lambda}{dt} = E_\alpha + jE_\beta = \frac{\partial \Lambda}{\partial z_p}\dot{z}_p e^{j\omega t} + j\omega\Lambda e^{j\omega t} \tag{2.9}$$

Replacing the 2.9 in the 2.5 and remembering that the current in the rotating reference frame can be expressed as

$$i_k = i_{r,k} e^{j\omega t} \tag{2.10}$$

The following equation can be obtained.

$$L_k \frac{di_{r,k}}{dt} + R_k i_{r,k} + j\omega L_k i_{r,k} + \frac{\partial \Lambda}{\partial z_p}\dot{z}_p + j\omega\Lambda = 0; \tag{2.11}$$

The last equation can be divided in to a direct and a quadrature component of the current remembering that $i_{r,k} = i_{d,k} + ji_{q,k}$.

$$\begin{cases} \frac{di_{d,k}}{dt} = -\omega_{p,k} i_{d,k} + \omega i_{q,k} - \frac{E_d}{L_k} \rightarrow Direct \quad component \\ \frac{di_{d,k}}{dt} = -\omega_{p,k} i_{d,k} + \omega i_{q,k} - \frac{E_d}{L_k} \rightarrow Quadrature \quad component \end{cases} \tag{2.12}$$

where

$$E_d = \frac{\partial \Lambda}{\partial z_p}\dot{z}_p \quad and \quad E_q = \Lambda\omega \tag{2.13}$$

Remark that the two equations 2.12 represent a voltage balance (divided by L) and so, by multiplying the first by $i_{d,k}$ and the second by $i_{q,k}$ and summing the two, the equation can be resorted to a power balance. Understanding each one of the power terms will determine which one is advocate of lift and drag forces. The resulting equation is the following:

$$L_k i_{d,k}\frac{di_{d,k}}{dt} + L_k i_{q,k}\frac{di_{q,k}}{dt} + R_k i_{d,k}^2 + R_k i_{q,k}^2 + E_d i_{d,k} + E_q i_{q,k} = 0 \tag{2.14}$$

Now it is quite evident what at least the first two pairs correspond to. The two terms containing the inductance express the power turns into stored magnetic energy, while the second couple is easily identifiable as a power consumption by Joule effect. The last two terms are instead those of interest, showing the mechanical power

involved with the levitation system. Lift and drag forces can be easily obtained by dividing the mechanical power by the related speed. The mechanical power coming from the direct components will produce the lift force equation dividing it by the vertical velocity of the pad $\dot{z}_p$, while the drag force will be obtained by dividing the power term containing the in quadrature component by the tangential speed of the track v.

$$\begin{cases} F_{lift} = \frac{E_d}{\dot{z}_p} \sum_{k=1}^{N_b} i_{d,k} = \frac{\partial \Lambda}{\partial z_p} \sum_{k=1}^{N_b} i_{d,k} \\ F_{drag} = -\frac{E_q}{v} \sum_{k=1}^{N_b} i_{q,k} = -\frac{\Lambda}{\gamma} \sum_{k=1}^{N_b} i_{q,k} \end{cases} \tag{2.15}$$

In static conditions, when the vertical position of the pad is fixed and the velocity remains constant, the derivative terms in the differential equations 2.12 become regular algebraic equations, thus the 2.15 can be explicitly determined. By making the substitutions one can obtain what follows.

$$\begin{cases} F_{lift} = \frac{\Lambda_0^2}{\gamma} e^{-2z_p/\gamma} \sum_{k=1}^{N_b} \frac{\omega^2/\omega_{p,k}^2}{L_k(1+\omega^2/\omega_{p,k}^2)} \\ F_{drag} = \frac{\Lambda_0^2}{\gamma} e^{-2z_p/\gamma} \sum_{k=1}^{N_b} \frac{\omega/\omega_{p,k}}{L_k(1+\omega^2/\omega_{p,k}^2)} \end{cases} \tag{2.16}$$

The assumptions behind these equations will be referred to in the discussion about the quasi-static analysis in the following chapter. These equations can be computed at varying track velocity and for varying rotational speed to obtain what shown in figure 2.7.

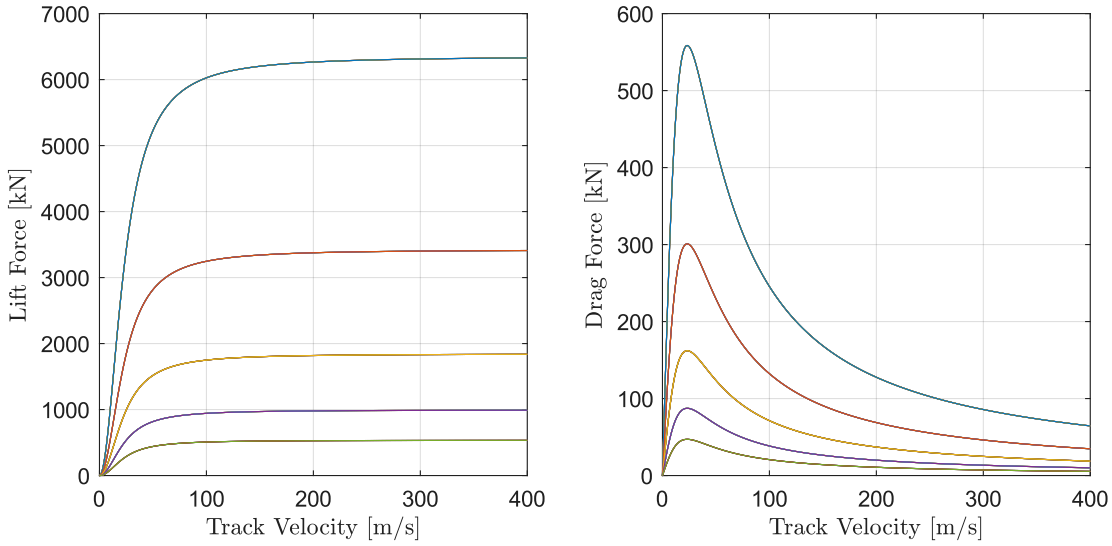

Figure 2.7: Static Drag and Lift force for varying air gap. Air gap values in order from top to bottom curves: 10mm, 15mm, 20mm, 25mm, 30mm

This formulation of the levitation physics is not suitable to be introduced into a state space set of equations due to its non linear formulation. Linearization must be performed to build a state space system.

2.4.1 Linearization

Once that the non linear equations for lift and drag force have been obtained, the interest is to linearize them around a certain a vertical displacement of interest $z_{p,0}$. By first order Taylor expansion of equation 2.6 one can obtain

$$\bar{\Lambda} = \Lambda_0 e^{z_{p,0}/\gamma} - \frac{\Lambda_0}{\gamma} e^{-z_{p,0}/\gamma}(z_p - z_{p,0}) \tag{2.17}$$

Hence, the linearized equations for the direct and in quadrature current components are written as follows:

$$\begin{cases} \frac{di_{d,k}}{dt} = -\omega_{p,k} i_{d,k} + \omega i_{q,k} - \frac{\Lambda_0}{\gamma L_k} e^{-z_{p,0}/\gamma} \dot{z}_p \\ \frac{di_{q,k}}{dt} = -\omega_{p,k} i_{q,k} + \omega i_{q,k} - \frac{\omega \Lambda_0}{L_k \gamma} e^{-z_{p,0}/\gamma}(z_p - z_{p,0}) - \frac{\omega}{L_k} \Lambda_0 e^{-z_{p,0}/\gamma} \end{cases} \tag{2.18}$$

And the lift force can be expressed as follows:

$$-\bar{F}_{lift} = \sum_{k=1}^{N_b} \left(\frac{\Lambda_0^2}{\gamma L_k} e^{-2z_{p,0}/\gamma} + \frac{2\Lambda_0}{\gamma} e^{-z_{p,0}/\gamma} i_{d,k} \right) \tag{2.19}$$

Notice that the linearization point is not random but is well defined for each operating speed. The issue with the linearization is that the system's accuracy is depleted the further the real speed is from the linearization point. There is an air gap value that satisfies the static balance between vertical lift force and weight of the pad. Being m_t the total mass to be levitated, the equilibrium air gap is simply obtained as follows.

$$F_{lift} = m_t \cdot g \xrightarrow{2.16} z_{p,0}(\omega) = -\frac{\gamma}{2} ln(\frac{m_t g \gamma}{\Lambda_0^2 \Gamma(\omega)}) \tag{2.20}$$

Where

$$\Gamma(\omega) = \sum_{k=1}^{N_b} \frac{\omega^2/\omega_{p,k}^2}{L_k(1 + \omega^2/\omega_{p,k}^2)} \tag{2.21}$$

Finally, having linearized the behavior of the electrodynamic suspension, such system can be treated as a spring-suspended 2dof model, particularly, this process led to a simplified version of the levitated carriage that is by all means a Quarter Car Model with a tire stiffness that is obtained as follows.

$$k_p = \frac{\partial F_{lift}}{z_p} = \frac{2\Lambda_0^2}{\gamma^2} e^{-2z_p/\gamma} \Gamma(\omega) \rightarrow k_p = \frac{2 m_t g}{\gamma} \tag{2.22}$$

Though it may seem very straight forward to substitute the levitation mechanism with an equivalent spring, a significant limitation arises from the assumption of such spring to have constant stiffness at all speeds. This approach is not suitable to

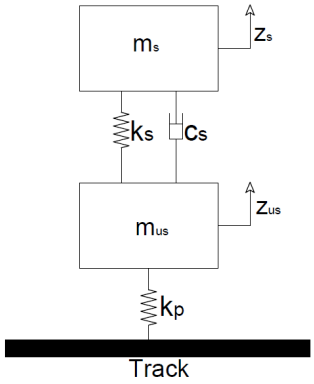

Figure 2.8: Simplification of the Electrodynamic suspension

perform dynamic analyses of the system, which will be instead performed using the linearized version containing the two-branched electrical subsystem. The derivation of this formulation of k_p was not vain as it will turn out useful in the Kalman filtering for the estimation of the states, since it provides a smaller system that is good enough for that purpose. It is important then to enlighten that the analyses in the following chapter will make extensive use of the linearized model containing the RL branches.

2.4.2 Single Degree of Freedom stability

With the purpose of seeing how this kind of model can be implemented in state space equations and in order to prove that the Electrodynamic Levitation Suspension technology is intrinsically unstable, the following section aims at the derivation of the full state space matrices describing a 1 dof levitated system and to perform a stability analysis via root locus plot. Equations 2.18, obtained earlier can be put

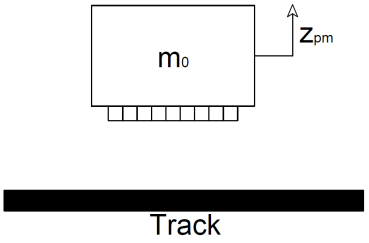

Figure 2.9: Single degree of freedom levitated system

together with the system's dynamic equation [3].

$$m_0 \ddot{z}_{pm} = f_{pm} + f_{lift} \tag{2.23}$$

where f_{pm} is a generic external force acting on the pad and comprising the weight. The following system of equations can be arranged

$$\begin{cases} \frac{di_{d,1}}{dt} = -\omega_{p,1} i_{d,1} + \omega i_{q,1} - \frac{\Lambda_0}{\gamma L_1} e^{-z_{pm,0}/\gamma} \dot{z}_{pm} \\ \frac{di_{q,1}}{dt} = -\omega_{p,1} i_{q,1} + \omega i_{q,1} - \frac{\omega \Lambda_0}{L_1 \gamma} e^{-z_{pm,0}/\gamma}(z_{pm}) - \frac{\omega}{L_1} \Lambda_0 e^{-z_{pm,0}/\gamma} \\ \frac{di_{d,2}}{dt} = -\omega_{p,2} i_{d,2} + \omega i_{q,2} - \frac{\Lambda_0}{\gamma L_2} e^{-z_{pm,0}/\gamma} \dot{z}_{pm} \\ \frac{di_{q,2}}{dt} = -\omega_{p,2} i_{q,2} + \omega i_{q,2} - \frac{\omega \Lambda_0}{L_2 \gamma} e^{-z_{pm,0}/\gamma}(z_{pm}) - \frac{\omega}{L_2} \Lambda_0 e^{-z_{pm,0}/\gamma} \\ \dot{z}_{in} = \dot{z}_{in} \\ \ddot{z}_{pm} = \frac{f_{pm}}{m_0} - \frac{2\Lambda_0}{\gamma m_0} e^{-z_{p,0}/\gamma} i_{d,1} - \frac{2\Lambda_0}{\gamma m_0} e^{-z_{p,0}/\gamma} i_{d,2} \\ \dot{z}_{pm} = \dot{z}_{pm} \end{cases} \tag{2.24}$$

This system of equation (2.24) is written in such a way that the translation in state space equation is very straight forward if the state vector 2.25 is adopted

$$\mathbf{z} = \begin{bmatrix} i_{d,1} & i_{q,1} & i_{d,2} & i_{q,2} & z_{in} & \dot{z}_{pm} & z_{pm} \end{bmatrix}^\top \tag{2.25}$$

The state space matrices **A**, **B**, **C**, **D** together with input and output vectors **u** and **y** are explicitly reported in Appendix A.1. The resulting state space system is a 7 states, 2 inputs and 1 output system that can be expressed in equation 2.26.

$$\begin{cases} \dot{Z}_{EDS} = A_{EDS} \cdot Z_{EDS} + B_{EDS} \cdot U_{EDS} \\ Y_{EDS} = C_{EDS} \cdot Z_{EDS} + D_{EDS} \cdot U_{EDS} \end{cases} \tag{2.26}$$

The root locus plot displayed in Figure 2.10 depicts the poles of the system for

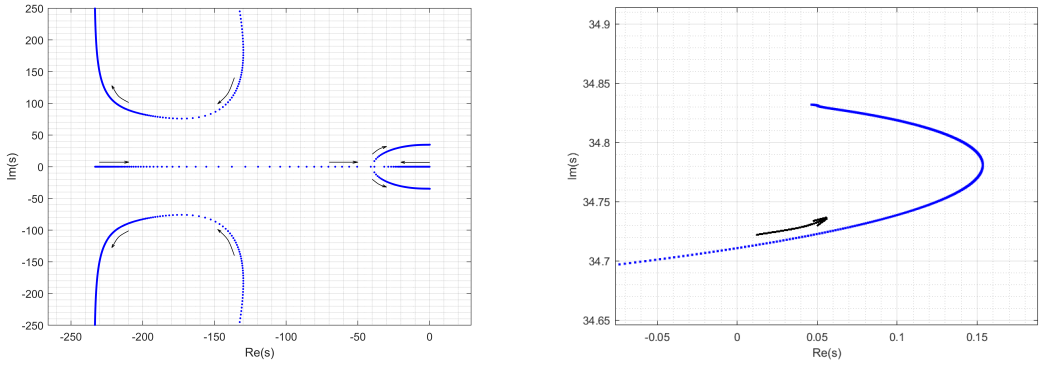

(a) (b)

Figure 2.10: (a) Root locus of the Electrodynamic suspension system using test bench parameters (b) Zoom into the instability region

varying rotational speed of the track. Notice that each set of poles corresponds to

Parameter	**Symbol**	**Value**	**Unit**
First Branch Resistance	R_1	25.28	Ω
Second Branch Resistance	R_2	257.79	Ω
First Branch Inductance	L_1	108.4	mH
Second Branch Inductance	L_2	179.9	mH
First Branch Pole Frequency	$w_{p,1}$	233.17	rad/s
Second Branch Pole Frequency	$w_{p,2}$	1432.43	rad/s
Track Rotational Speed	ω	500	rpm
Pad Mass	m_0	20.02	kg
Magnetic Flux linkage amplitude	Λ_0	1	—
Pole pitch ratio	γ	0.0162	m
Equilibrium air gap at $\omega[rpm]$	$z_{p,0}$	10.7	mm

Table 2.2: Parameters used for the SDOF stability analysis

a different formulation of the state space matrices as the mechanical characteristics of the system change with varying speed, as discussed when talking of equivalent levitation stiffness. As visible from Figure 2.10, the system eventually becomes unstable. The dynamic analysis shows that, such instability happens in the mechanical domain and is reached at a relative speed of around 4.78m/s which is well below the normal operating range of the test bench. This proves that the Electrodynamic levitation system as proposed needs some sort of active stabilization in order to work properly.

2.4.3 Two-Degree of freedom stability

The analysis conducted on the one degree of freedom system was brought to demonstrate how the mathematical model for the EDS suspension derived in the previous paragraphs could be formulated in a state space-representation. Furthermore, such analysis established that EDS system exhibits inherent instability already at very low speeds. For the evaluation of two degrees of freedom stability, a similar approach can be exploited, using bigger state space matrices. Detailed modeling and results concerning this analysis can be found in *Galluzzi*'s paper in reference [3]. It is therefore unnecessary to deal with this model's derivation in this work. A more complex model containing the 2-DOF physics adapted to the test bench characteristics is covered in the following sections. Nonetheless it is interesting to briefly discuss the results obtained in *Galluzzi*'s paper. A root locus was generated containing poles referring to systems with different track rotational speed and suspension damping. In absence of damping the root locus of both the sprung and unsprung masses resembles what seen for the 1-DOF stability, crossing the imaginary axis already at very low speed. Introduction of damping induces a shift of all the poles towards the left, in the stability region of the Aargand plane, thus enhancing stability. The beneficial effect of increasing damping is limited by an optimal damping value after which some poles tend again towards the unstable region. While, as said, the detailed analysis is omitted here, it is worth to include a plot coming from *Galluzzi* that represent what has just been said.

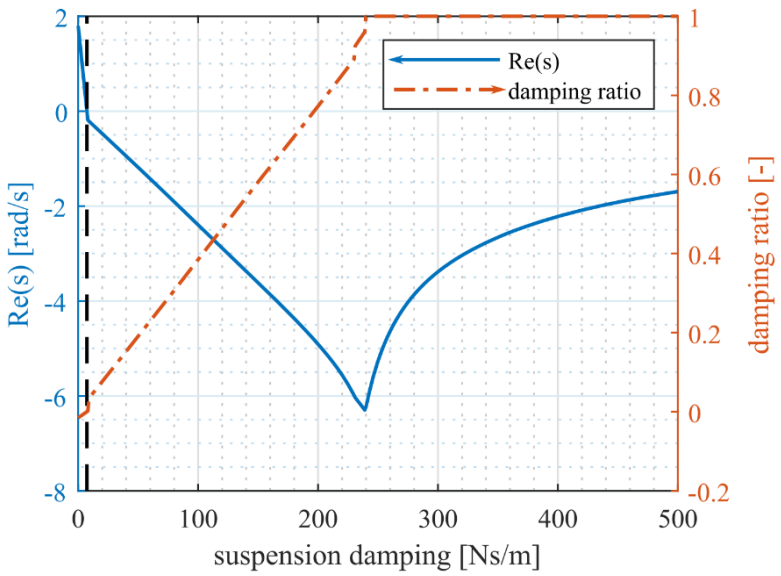

Figure 2.11: Credit:[3] An increase in suspension damping drives the real part of the poles further into the stability region up to a certain optimal damping. After such damping the trend is inverted

Chapter 3

Test Bench for Electrodynamic Levitation Suspension

In this chapter, some insights on the test-bench structure and characteristics are provided. This test-bench is used with the dual purpose of system dynamic characterization and testing of control strategies. The very same test bench was set up and analyzed in previous thesis works [6],[7], quasi static analysis have already been conducted and the parameters defining the mathematical model have been determined in *Bosica*'s work [5].

3.1 Main Bench

The test bench is designed to replicate the motion of the pad's Halbach array gliding over a conductive copper track. This motion is achieved by making the circular copper track move beneath the stationary Halbach array, which is solidal to the measuring device. This configuration is diametrically opposed to the real application where, instead, the pad moves along a static track. Surprisingly, though, this "unnatural" approach yields significant benefits. In fact, this setup with reversed kinematics, allows to neglect the aerodynamic drag forces acting on the pad, which is a realistic assumption if working with Hyperloop trains, given that they travel in a near-vacuum environment. A visual perspective of the external appearance of the test bench is provided inf Figure 3.1 in which a 3d CAD model can be seen. Notably, no moving parts can be spotted in this figure as they are enclosed within a protective PVC-aluminum cover. The test bench comprises a table made of aluminum girders acting as foundation. On top of this foundation lays an housing

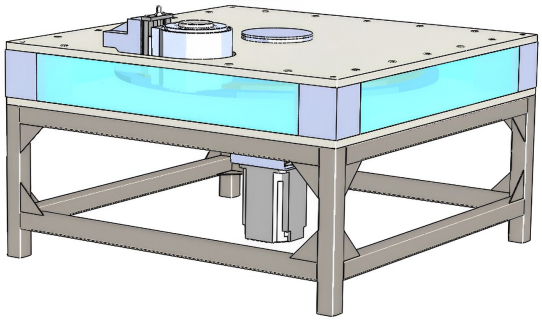

Figure 3.1: Exterior view of the Test-bench

made of two aluminum slabs, one on top and one at the bottom acting as roof and floor of the housing, and transparent PVC side walls allowing both protection in case of failure at high rotational speeds and for a view to the rotating track, depicted in figure 3.2. The "roof" of the enclosure is sustained by 4 aluminum blocks, one on each corner. The core of the setup lays within the enclosure. Figure 3.2 provides a cut view of the test bench. Here one can observe the copper track of the electrodynamic suspension, which as a ring shape and is attached to an aluminum disk. This aluminum disk is then solidal to the vertical shaft, highlighted in green, which is sustained in vertical position by a couple of ball bearings on its edges, assuring smooth operation of the system. The shaft is then connected with the electric motor (highlighted in red) (*Kollmorgen AKM74L*[8]) which is located beneath the table and which responsible of the movement of the track. The connection between the shaft and the motor is achieved by means of a torsional joint (colored in black). All the joint structure is enclosed within a protective plastic casing. Having talked about the track structure is now the time to discuss about how to simulate the train. The assembly simulating the levitation from now

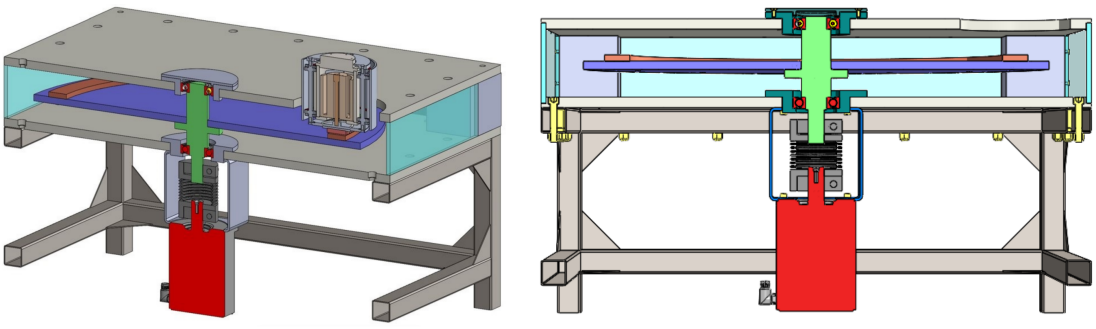

(a) (b)

Figure 3.2: (a) Cut 3D model of the Test Bench (b) Test Bench cross section

on referred to as measuring device is installed in an ellipsoidal hole obtained in the ceiling of the enclosure. The measuring device's structure will be discussed in the next paragraphs, for the moment we can distinguish two types of measuring device, being the quasi-static measuring device and the dynamic measuring device. The former, applied for quasi static analysis and parameters evaluation, the latter utilized for stability analysis and control. Whether of the two it is, the measuring device is installed atop of the aluminum ceiling to an aluminum support which can be adjusted in height with micrometric precision thanks to a micrometric stage. Table 3.1 provides an idea of the dimension of the test-bench. Dimensions that are notably quite big, being the aluminum disk more than 1 meter wide. Figure 3.3 (a) shows a real picture of the test-bench. Note that in Figure 3.3 (b) shows the top view of the hole for the measuring device. The measuring device is not installed but the support with micrometric stage is visible.

Feature	**Dimension [m]**
Test Bench overall width	1.30
Test Bench overall depth	1.30
Test Bench overall height	0.73
Copper track thickness	0.015
Copper Track inner diameter	0.88
Copper Track outer diameter	1.00
Aluminum disk diameter	1.10
Aluminum disk thickness	0.0185

Table 3.1: Test bench dimensions

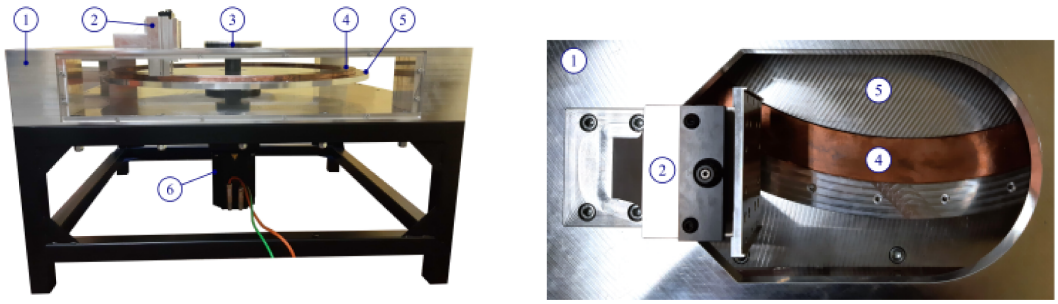

(a) (b)

Figure 3.3: [9](a) Lateral view of the test bench (b) top view of the measuring device hole. Features: 1. Test bench walls 2.; Measuring device support with micrometric stage; 3. Shaft; 4. Copper Track; 5. Aluminum disk; 6. Servo motor.

3.1.1 Copper track irregularities

It is trivial to say that the real world copper tracks, including those used in practical electrodynamic levitation systems, won't be anywhere close to geometric perfection. Imperfections of the track may also be large and may heavily influence the system performance and passengers' comfort. Provided that the pursuit is that of enhancing such comfort, an understanding of the entity of such irregularities is necessary and crucial to be able to perform accurate numerical simulations. Such characterization was conducted in *Andrea Bo*'s thesis by means of a centesimal dial gauge placed to cover 5 different concentric circumferences spanning the width of the copper track. Since the employed model fits a one-dimensional track displacement, the whole set of measurements is condensed in an averaged value, following the approach used in previous works by *Pakstys M.* [9] and *Bosica L.* [5]. A three-dimensional graphical representation of such irregularities along the track is provided in Figure 3.4, along with a two-dimensional representation in Figure 3.5 of the track vertical displacement and speed in time when the disk is rotating at a speed of 500rpm. To obtain such plots, the experimental data has been approximated thanks to Fourier's transform in to a sum of 5 sine waves. Thus a double approximation is involved with this track representation, the first one coming from considering the same vertical displacement for the whole track's width and the second related with this representation of the real data with a sum of sinusoids. Figure 3.6 shows a case study in which a 5mm copper slab is put on the track to check the performance of the system when a sudden impulsive excitation occurs. The circumferential extent of such step is equal to the length of the Halbach array. This input profile will be used later on in this work.

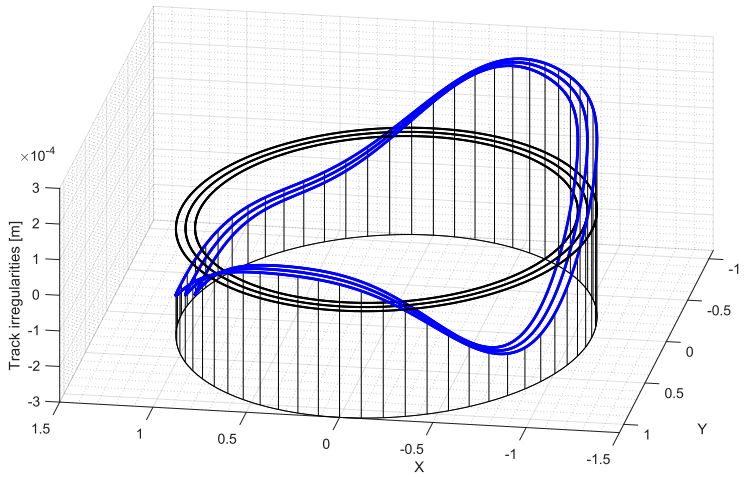

Figure 3.4: Copper track irregularities 3D plot. In blue the real track height; in black the ideal track height. Remark: out of scale dimensions

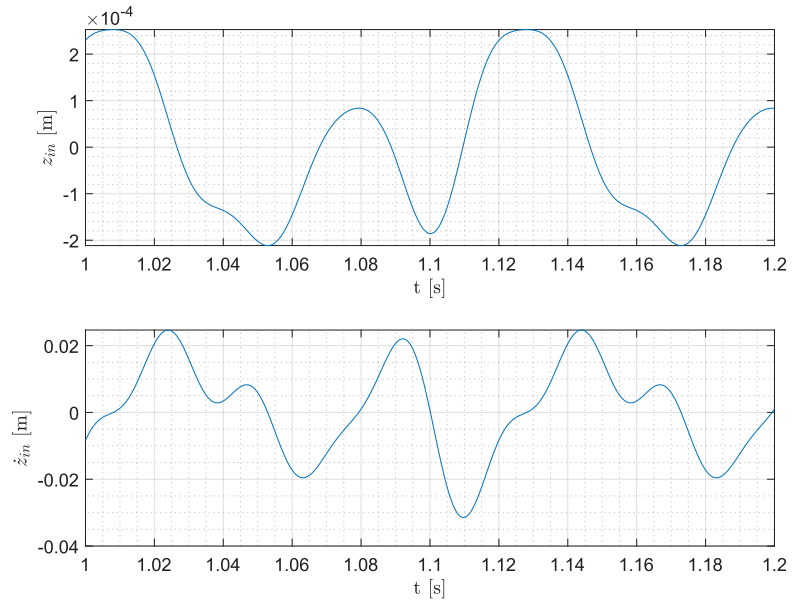

Figure 3.5: (top) Track vertical displacement $z_{in}[m]$ vs time; (bottom) track profile vertical velocity $\dot{z}_{in}[m/s]$ at 500rpm rotational speed

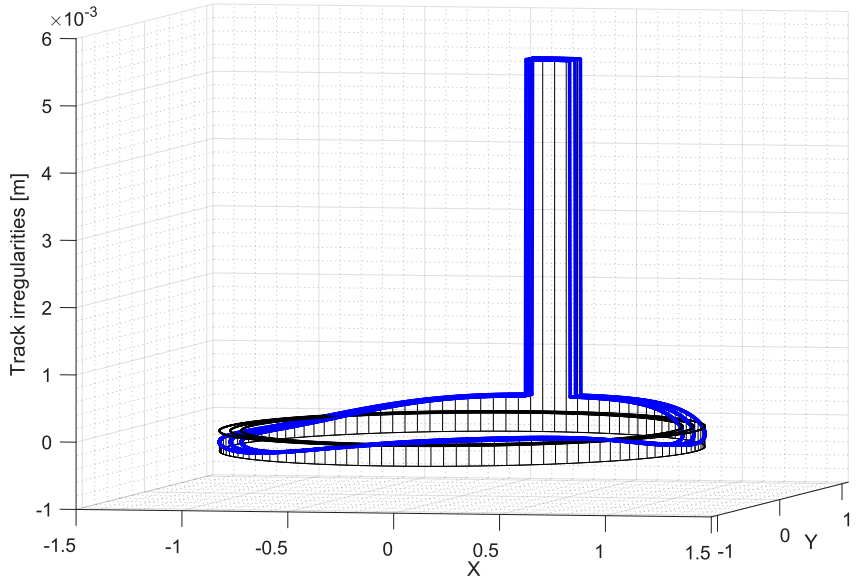

Figure 3.6: Copper track irregularities with slab 3D plot. In blue the real track height; in black the ideal track height. Remark: out of scale dimensions

3.2 Quasi static measuring device

This discussion brings some insights on how electrical parameters were obtained. Anyway, the quasi-static testing has deeply been dealt with in previous works, thus, only the numerical results concerning the 45 degrees configuration of the Halbach array is provided. As mentioned in the previous chapter, the derivation of equations for lift and drag force using the lumped parameters approach, relied on the assumption of static conditions. Such assumption implies a constant air gap and velocity, without considering any dynamic effect. This simplification transformed the original differential equations, expressing the behavior of lift and drag forces, into an algebraic form by eliminating time derivatives. Such equations ultimately led to plot what visible in Figure 2.15. The Quasi-Static measuring device is utilized to experimentally reproduce such curves so that, by overlapping the experimental data with the theoretical one, the parameters of the electrical subsystem used to model the track, can be tuned. These parameters include the number of electrical branches n, the resistance of each branch R_k, the branch inductance L_k and the branch pole frequency $\omega_{p,k}$.
The measuring device has a quite simple structure, as visible in Figure 3.7. An aluminum support structure is connected with a micro-metric linear stage, useful to adjust the air gap thickness. The Halbach array is connected to the structure by means of two pairs of flexural hinges. These hinges (in orange) serve the purpose decoupling the drag force contribution from the lift force contribution while measuring, conducting to more reliable results. Between these hinges and the

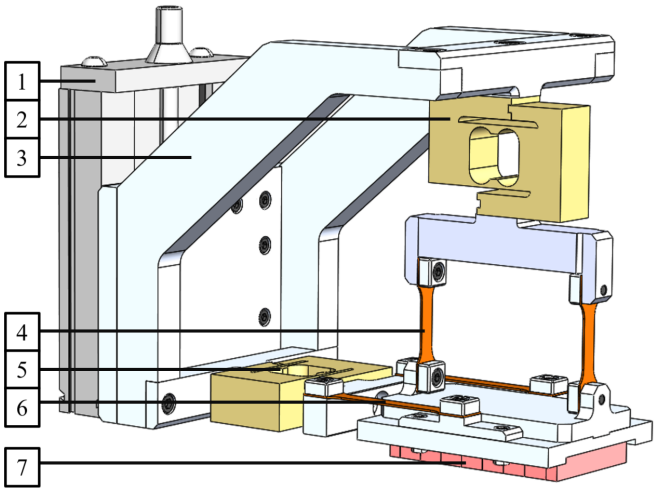

Figure 3.7: Quasi-Static Measuring Device. (1) Micro-metric Linear Stage; (2) Vertical load cell for lift force measurement; (3) Aluminum support structure; (4) Vertical flexural springs; (5) Horizontal load cell for Drag force measurement; (6) Horizontal flexural springs; (7) Halbach array.

structure, two load cells measure the lift and drag force. Various non-ideal factors come in to play with the presented measuring set up, reason why it is referred to as "Quasi-Static" measuring device. To begin, the pad's alignment with the copper track is far from perfection, presenting yaw, roll and pitch angles that contribute to deviations from the static assumption. Furthermore, the air gap thickness is not perfectly determined as errors may arise from imperfection of the micro-metric stage as well as from inaccuracy in the readings. Most importantly, as explained in the previous paragraph, the copper track exhibits irregularities, which introduce a dual negative effect on the static assumption since a constant air gap is not achievable and since the variation of track elevation arises dynamic effects and thus vibration of the pad. As mentioned in *Bosica*'s work [5], for the problem being, a two branched electrical subsystem can be adopted to have an acceptable error, in contrast with what adopted in *Galluzzi*'s work [3] which featured a three-branched electrical subsystem. The data was already collected in Table 2.2.

3.3 Dynamic measuring device

The dynamic measuring device constitutes the fulcrum of any dynamic analysis and control of the electrodynamic levitation system. This device has a quite more intricate structure than the quasi-static device, since it is designed to replicate the considerably more complex dynamic phenomenon. Figure 3.8 displays a three-dimensional cross section view of the device. The same micro metric linear stage, solidal with the test bench, used for the quasi-static measuring device, is utilized to control the system's initial air gap thickness. Mounted on this support, a complex arrangement of nested cylinders reproduces a physical system that can be represented by means of a quarter car model. Though it may not seem trivial from the figure, a sprung mass, simulating the train's cabin is decoupled from an unsprung mass that comprehends the levitation pad. The outermost cylinder serves as stator as it is solidal to the support structure. Moving inside such cylinder, a set of eight flexural springs (in red) resembles a sprung connection between the unsprung mass and the stator, a feature that does not appear in the classical quarter car model. What constitutes the unsprung mass are the two disks located at the top and at the bottom of the device, together with the vertical girders that connect the two. The Halbach array is also part of the unsprung mass. Moving deeper inside the device, the sprung mass can be identified as a cylindrical capsule housing the voice coil actuator assembly. The sprung mass is connected to the unsprung mass by means of eight flexural springs (highlighted in green in Figure 3.8). The voice coil actuator is the active part of the system, it is constituted by copper windings concentrically wound around movable rod. When an electrical current flows through the voice coil's windings, it generates a magnetic field that

pushes the moving rod outside or inside the assembly depending on the direction of the current, exerting a force on the unsprung mass and an equal and opposite force on the sprung mass. This force will be exploited to stabilize the system. It must be highlighted that the voice coil's masses are divided between the sprung and unsprung masses. In particular, the winding assembly's mass is attributed to the sprung mass, while the moving rod is part of the unsprung mass, being it solidal with the levitation pad.

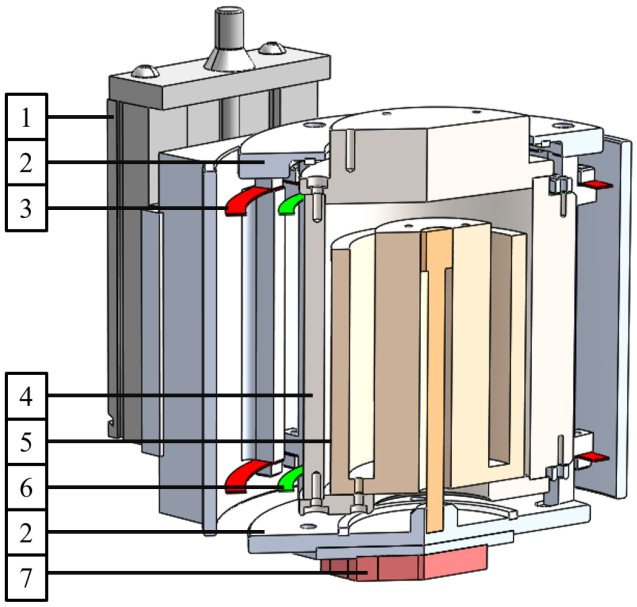

Figure 3.8: Dynamic Measuring Device. (1) Micro-metric linear stage; (2) Unsprung mass; (3) Unsprung mass to stator flat spring; (4) Sprung mass; (5) Voice coil assembly; (6) Sprung to unsprung mass flat springs; (7) Halbach array.

3.3.1 Voice coil actuator modeling

In order to control a very fast evolving dynamic phenomenon, an at least as fast computation and actuation must be adopted. While the computational part, thanks to modern days technology, can be dealt most of the times with ease and, if not, one can act by simplifying the algorithm, the actuating hardware part is the barrier as it needs to react very fast to rapidly changing inputs and also to produce quite big amounts of force. In this context, voice coil actuators are a key element. A voice coil actuator is a highly precise and controllable electrical actuator, which is suitable for short stroke actuation [10] [11]. Voice Coil Actuators (VCAs) allow for very fast operation thanks to their low electrical inductance and small moving masses. Acceleration can reach up to peaks of 500 g. Direct proportionality between

current and force makes them very easily applicable in control systems. These advantages come together with a relative simplicity which makes the system more rugged and reliable. A voice coil assembly is a cylindrical shaped object containing a shell of cylindrical permanent magnets and copper windings. A conductive rod acts as a plunger as it is able to move in or out of the hollow space in the center of the cylinder. The working principle revolves once again around Lorentz's forces and exploits the effect of current induced varying magnetic field. The electrical current flowing through the coil windings produces a magnetic flux that, depending on the direction of such current, pushes the plunger in or out of the shell. The permanent magnets increase the value of such magnetic field in a preferential direction and contrast the coil's magnetic field in the other direction. The voice coil actuator is a sort of solenoid that can be precisely controlled to generate the desired amount of force and displacement. The voice coil adopted in the dynamic measuring device, as announced in the previous paragraph, is attached to the sprung mass body, the movement of the plunger produces a couple of equal and opposite forces on the sprung and unsprung mass. Being such device electrically controlled by an input voltage (or current), it effectively acts as interface between the real test bench and any kind of in-software developed algorithm and control strategy. Given the dual essence of the voice coil actuator, which has both an electrical and mechanical aspect, any model describing it must resort to both these domains. The proposed model is probably the simplest dynamic model one can write down for a voice coil actuator, exploiting base equations of electronics and mechanics. It may not be the most accurate way to represent such system but it was deemed enough as a balance between complexity and efficacy.

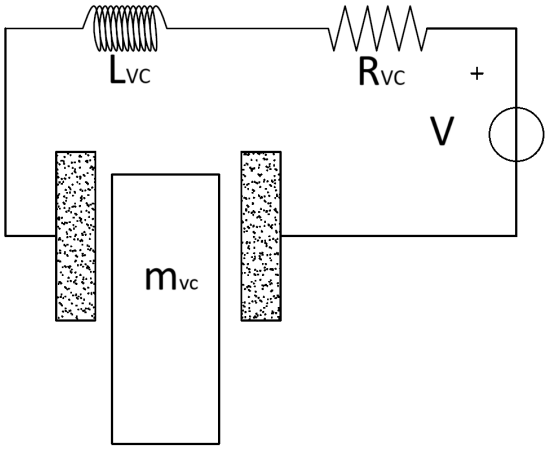

Figure 3.9: Voice coil mechanical and electrical domains

3.3.2 VCA mechanical domain

Given a local coordinate system z expressing the vertical displacement of the voice coil's plunger, the mechanical domain can be resorted to a simple one degree of freedom dynamic equation. It can be evidenced that no elastic force can be spotted. The actions involved with the voice coil can be distinguished in passive and active forces. While the active force is clearly the researched effect, a not so evident dissipative viscous force exists. When the ferromagnetic plunger gets within the voice coil, the reluctance of the magnetic circuit changes. The permanent magnets' magnetic field finds in the ferromagnetic body a preferential way, thus, an increase in magnetic flux density is experienced in the core of the voice coil. This will, in turn, produce, by Faraday's induction law, a current whose effect is that of opposing to the cause that generated it (Lenz's law). Thus, a new magnetic field pushing out the ferromagnetic body arises and its intensity is proportional to the speed of the body. Therefore, this interaction can be schematized by introducing an "ignorance" damping coefficient c_{vc}. Thus, the passive viscous forces can be expressed as follows

$$F_{passive} = c_{vc} \cdot z \tag{3.1}$$

The active force exerted by the VCA is directly proportional to the circulating current, as specified by the producer. The Mechanical Voice Coil Constant K_m is the constant of proportionality involved in this relation. This equation holds quite well for every displacement as can be seen in the technical sheet [11]. The active force can be expressed as follows.

$$F_{active} = K_m \cdot i_{vc} \tag{3.2}$$

Considering the weight force and the inertia effect one can derive the following equation

$$\begin{aligned} m_0\ddot{z} + F_{passive} &= F_{active} - m_0 g \\ m_0\ddot{z} + c_{vc}\dot{z} &= K_m i_{vc} - m_0 g \end{aligned} \tag{3.3}$$

3.3.3 VCA electrical domain

A classical RL circuit can be used to model the electrical domain of the VCA, as visible in Figure 3.9. The viscous damping effect cited in the mechanical domain discussion is coupled with a flowing current within the voice coil's windings. This effect must be then assessed also in the electrical domain as an induced Back ElectroMotive Force Voltage (ΔV_{BEMF}). While the active force was modeled resorting to a proportionality with the voice coil current i_{vc} using the mechanical voice coil's constant K_m, the back electromotive force voltage is written similarly and, instead, uses as constant of proportionality the voice coil's velocity constant K_v.

$$\Delta V_{BEMF} = K_v \dot{z} \tag{3.4}$$

Applying Kirchhoff's law to the electrical subsystem, the following equation can be written.

$$L_{vc}\frac{di_{vc}}{dt} + R_{vc} \cdot i_{vc} + K_v \dot{z} = V \tag{3.5}$$

In conclusion, the two equations that model the voice coil sub-system have been obtained and are collected below

$$\begin{cases} m_0 \ddot{z} + c_{vc}\dot{z} = K_m i_{vc} - m_0 g \\ L_{vc}\frac{di_{vc}}{dt} + R_{vc} \cdot i_{vc} + K_v \dot{z} = V \end{cases} \tag{3.6}$$

Table 3.2 contains all the parameters that will be used also in the full model. Remark the very low value of voice coil inductance. This property along with low mechanical inertia properties allow for very rapid actuation.

Parameter	**Symbol**	**Value**	**Unit**
Voice Coil Resistance	R_{vc}	1.77	Ω
Voice Coil Inductance	L_{vc}	$15.17 \cdot 10^{-3}$	H
Mechanical Force Constant	K_m	25	N/A
Electrical Velocity Constant	K_v	25	Vs/m
Voice Coil Damping Coefficient	c_{vc}	220	Ns/m

Table 3.2: Voice coil parameters

3.4 Dynamic measuring device full system modeling

Once that the theoretical approach to model, the levitation physics and the electromechanical action counterpart has been discussed, a full model, comprehensive of every trait of the dynamic measuring device can be resorted to. Figure 3.10 displays a schematic representation of the dynamic measuring device setup. Everything that was discussed in this and in the previous chapter is hereby collected. The two-branched electrical circuit is symbolically placed on the copper track. The full

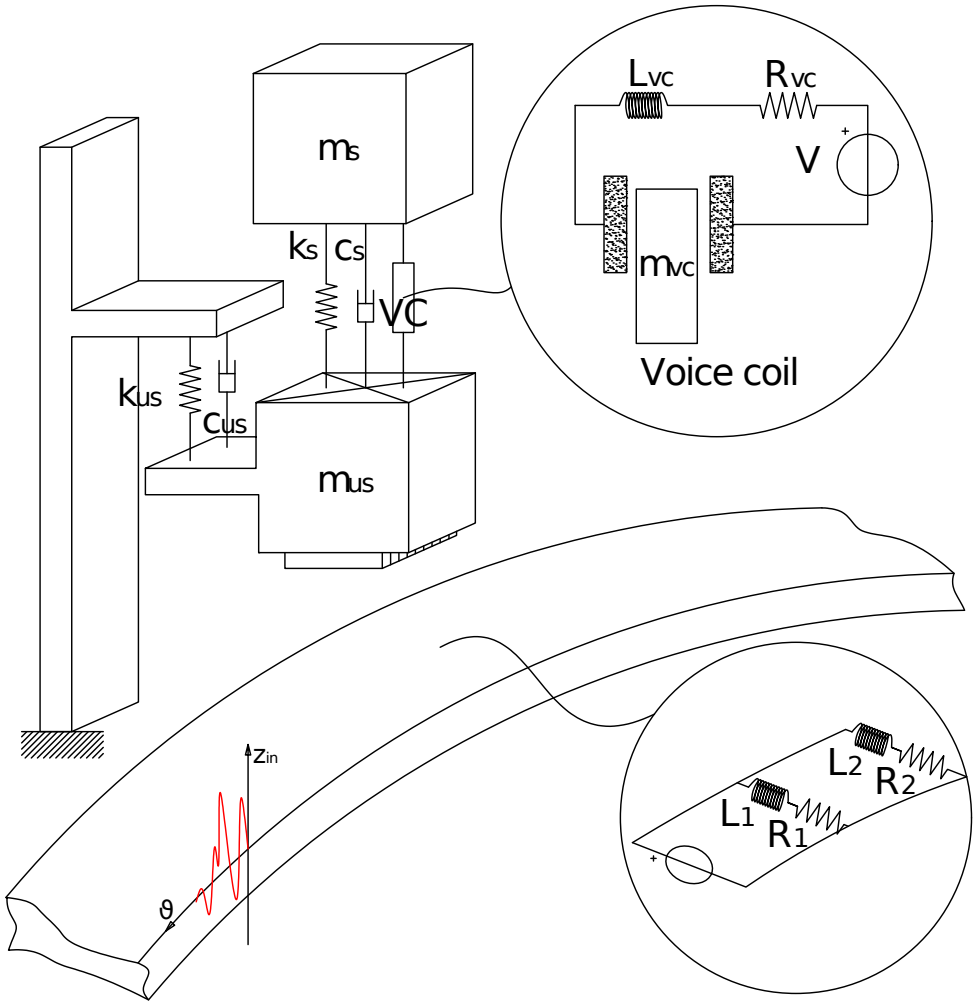

Figure 3.10: Schematic drawing of the full model for the electrodynamic levitation suspension measuring device. The following features can be spotted: Quarter car model with connection of the unsprung mass with the stator; Voice coil sub-system; Halbach array; Two-branched electrical subsystem; Track irregularities reference frame

model for the dynamic measuring device will be obtained exploiting the matrices obtained in the previous chapter for the one degree of freedom levitated system. What that system is missing is the full description of the mechanical and voice coil domain, which will be instead obtained in the following rows. Two vertical reference frames z_s and z_{us} can be fixed for the sprung and unsprung mass, conventionally having upward direction. Assuming that a positive value of current produces a downward force on the unsprung mass and an equal upward force on the sprung mass, one can set up the free body diagram to derive the following equations. The detailed derivation of such equations is very simple and can be found on any book of mechanical systems dynamics [12].

$$\begin{cases} m_{us}\ddot{z}_{us} + (c_s + c_{us})\dot{z}_{us} - c_s\dot{z}_s + (k_s + k_{us}) = f_{tot,us} \\ m_s\ddot{z}_s - c_s\dot{z}_{us} + c_s\dot{z}_s - k_s z_{us} + k_s z_s = f_{tot,s} \end{cases} \tag{3.7}$$

Where $f_{tot,s}$ and $f_{tot,us}$ represent the sum of any real external force acting on the respective mass summed to the voice coil actuator's force. This latter force can be detached and brought to the right member. Also, recalling equation 3.5, the following system can be set up.

$$\begin{cases} m_{us}\ddot{z}_{us} + (c_s + c_{us})\dot{z}_{us} - c_s\dot{z}_s + (k_s + k_{us}) + K_m i_{vc} = f_{us} \\ m_s\ddot{z}_s - c_s\dot{z}_{us} + c_s\dot{z}_s - k_s z_{us} + k_s z_s - K_m i_{vc} = f_s \\ \frac{di_{vc}}{dt} = -\frac{R_{vc}}{L_{vc}} i_{vc} + \frac{K_v}{L_{vc}}(\dot{z}_{us} - \dot{z}_s) + \frac{V}{L_{vc}} \end{cases} \tag{3.8}$$

The previous equation can be rearranged to be easily converted in state space form as follows

$$\begin{cases} \ddot{z}_{us} = -\frac{(c_s+c_{us})}{m_{us}}\dot{z}_{us} + \frac{c_s}{m_{us}}\dot{z}_s - \frac{(k_s+k_{us})}{m_{us}} - \frac{K_m}{m_{us}} i_{vc} + \frac{f_{us}}{m_{us}} \\ \dot{z}_{us} = \dot{z}_{us} \\ \ddot{z}_s = \frac{c_s}{m_s}\dot{z}_{us} - \frac{c_s}{m_s}\dot{z}_s + \frac{k_s}{m_s} z_{us} - \frac{k_s}{m_s} z_s + \frac{K_m}{m_s} i_{vc} + \frac{f_s}{m_s} \\ \dot{z}_s = \dot{z}_s \\ \frac{di_{vc}}{dt} = -\frac{R_{vc}}{L_{vc}} i_{vc} + \frac{K_v}{L_{vc}}(\dot{z}_{us} - \dot{z}_s) + \frac{V}{L_{vc}} \end{cases} \tag{3.9}$$

As discussed earlier, this model is representative of the mechanical subsystem of the dynamic measuring device. This includes both the sprung and unsprung masses, together with the connection of the unsprung mass ad the stator. In addition, the model incorporates the physics regarding the voice coil actuator discussed in the paragraphs above. The full model can be derived by assembling together the electrodynamic levitation theory applied to the one degree of freedom levitated system, expressed in Equation 2.24, with the newly obtained model in Equation 3.9. This passage is equivalent to the "wedding" between the quarter car model

and the levitation pad. The resulting system of equations is expressed below.

$$\begin{cases} \frac{di_{d,1}}{dt} = -\omega_{p,1} i_{d,1} + \omega i_{q,1} - \frac{\Lambda_0}{\gamma L_1} e^{-z_{us,0}/\gamma} \dot{z}_{us} \\ \frac{di_{q,1}}{dt} = -\omega_{p,1} i_{q,1} + \omega i_{q,1} - \frac{\omega \Lambda_0}{L_1 \gamma} e^{-z_{us,0}/\gamma}(z_{us}) - \frac{\omega}{L_1} \Lambda_0 e^{-z_{us,0}/\gamma} \\ \frac{di_{d,2}}{dt} = -\omega_{p,2} i_{d,2} + \omega i_{q,2} - \frac{\Lambda_0}{\gamma L_2} e^{-z_{us,0}/\gamma} \dot{z}_{us} \\ \frac{di_{q,2}}{dt} = -\omega_{p,2} i_{q,2} + \omega i_{q,2} - \frac{\omega \Lambda_0}{L_2 \gamma} e^{-z_{us,0}/\gamma}(z_{us}) - \frac{\omega}{L_2} \Lambda_0 e^{-z_{us,0}/\gamma} \\ \dot{z}_{in} = \dot{z}_{in} \\ \ddot{z}_{us} = -\frac{(c_s + c_{us})}{m_{us}} \dot{z}_{us} + \frac{c_s}{m_{us}} \dot{z}_s - \frac{(k_s + k_{us})}{m_{us}} - \frac{K_m}{m_{us}} i_{vc} + \frac{f_{us}}{m_{us}} - \frac{2\Lambda_0}{\gamma m_{us}} e^{-z_{us,0}/\gamma} i_{d,1} + \\ \quad - \frac{2\Lambda_0}{\gamma m_{us}} e^{-z_{us,0}/\gamma} i_{d,2} \\ \dot{z}_{us} = \dot{z}_{us} \\ \ddot{z}_s = \frac{c_s}{m_s} \dot{z}_{us} - \frac{c_s}{m_s} \dot{z}_s + \frac{k_s}{m_s} z_{us} - \frac{k_s}{m_s} z_s + \frac{K_m}{m_s} i_{vc} + \frac{f_s}{m_s} \\ \dot{z}_s = \dot{z}_s \\ \frac{di_{vc}}{dt} = -\frac{R_{vc}}{L_{vc}} i_{vc} + \frac{K_v}{L_{vc}} (\dot{z}_{us} - \dot{z}_s) + \frac{V}{L_{vc}} \end{cases} \tag{3.10}$$

Such operation can be translated in a matrix assembly as shown in the following illustration. The matrices for the EDS suspension must be computed for the desired

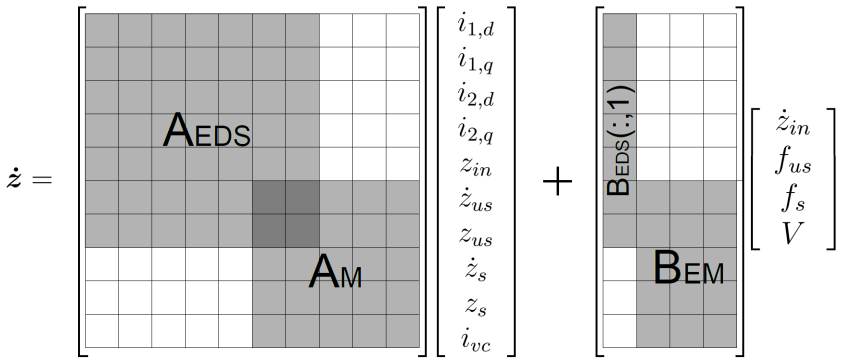

rotational speed ω. The final full model matrices so obtained are written explicitly in Appendix A.3 and the model is a a four input three output and ten states state space that can be written as follows.

$$\begin{cases} \dot{Z}_{full} = A_{full} \cdot Z_{full} + B_{full} \cdot U_{full} \\ Y_{full} = C_{full} \cdot Z_{full} + D_{full} \cdot U_{full} \end{cases} \tag{3.11}$$

3.4.1 Data

Having established the theoretical foundation of the device, and having highlighted the underlying assumptions both in this and in the preceding chapter, the numerical analysis can be carried on. The first step is to list all the data that will be input in

MATLAB in order to build a working mathematical model. Table 3.3 resumes all the necessary data and, for convenience, includes some that has already been cited in previous tables.

Parameter	**Symbol**	**Value**	**Unit**
Mutual induction coefficient amplitude	Λ_0	1	Wb
Number of magnets	N_m	8	—
Single magnet width	a_m	12.7	mm
Pole pitch ratio	γ	0.0162	m
First Branch Resistance	R_1	25.28	Ω
Second Branch Resistance	R_2	257.79	Ω
First Branch Inductance	L_1	108.4	mH
Second Branch Inductance	L_2	179.9	mH
First Branch Pole Frequency	$w_{p,1}$	233.17	rad/s
Second Branch Pole Frequency	$w_{p,2}$	1432.43	rad/s
Copper track mean radius	r_m	0.47	m
Sprung mass	m_s	15.82	kg
Unsprung mass	m_{us}	4.20	kg
Voice Coil Resistance	R_{vc}	1.77	Ω
Voice Coil Inductance	L_{vc}	$15.17 \cdot 10^{-3}$	H
Mechanical Force Constant	K_m	25	N/A
Electrical Velocity Constant	K_v	25	Vs/m
Voice Coil Damping Coefficient	c_{vc}	220	Ns/m
Suspension stiffness	k_s	4422	N/m
Unsprung mass to stator stiffness	k_{us}	9700	N/m

Table 3.3: Complete data characterizing the dynamic measuring device model

Chapter 4

Test Bench Numerical Analysis

In this chapter, numerical analyses will be carried on the model described previously. All the model data and matrices were loaded in Matlab and time simulations were carried on Simulink environment. The system's dynamic characteristics will be evidenced through root loci plots and its performance, varying some of the major parameters, will be highlighted. Variations of the parameters of the system will be also simulated by the active contribution of the voice coil. In this first stage, the easiest possible feedback line is set in place to check the feasibility of retro-actuating the system. Such line will consist of a simple static gain wanting to simulate the effect of an additional damper.

4.1 Parametric Stability Analysis

At this point, it is important to gain some insights into the dynamic behavior of the measuring device. Dynamics that can be comprehensively understood by using one of the many tools such as Frequency Response Functions (FRFs), time domain responses, sensitivity analyses and so on. One of the most effective tools to assess systems' stability is the Root Locus plot. A Root Locus Plot provides a visual representation of the system's dynamic characteristics, effectively showing the system's "dynamic identity" and providing information about its stability or instability. Moreover, it allows to distinguish between strong and marginal stability and, perhaps most importantly, a root locus plot provides a visual depiction of how changes in systems' parameters can impact its stability either by improving it or by depleting it and at what rate. Figure 4.1 contains a portion of the root locus plot characterizing the full system. It contains poles regarding both the mechanical and electrical subsystems. In particular, in figure 4.1 (a) the poles identifying

the dynamics of the first electrical branch, the unsprung and sprung mass can be seen. Reading from left to right, the first two U-shaped loci represent the first electrical branch showing how, increasing the track rotational speed, the poles tend to asymptotically reach the first electrical branch's pole frequency which was $w_{p,1} \cong 233 rad/s$ as seen in Table 3.3. Going on towards the imaginary axis, a big C-shaped locus can be spotted and represents the poles of the unsprung mass. As visible, such poles do also manifest an asymptotic behavior towards a given point in the complex plane. A similar behavior is also that of the sprung mass, whose corresponding root locus is zoomed in Figure 4.1 (b). The root locus is missing the poles related to the second branch of the electrical subsystem, poles that are anyway far into the stability region and whose assessment is not so relevant. It is visible how the full system root locus asymptotically reaches the imaginary axis, showing, then, marginal stability. An important remark can be made in parallel to what seen in Chapter 2, where a root locus plot showing the behavior of a one degree of freedom levitated system was shown. In that case, the root locus plot extended beyond the imaginary axis, showing unstable behavior already at very low speed, in this case, instead, the unsprung mass seems to be well within the stability region. This condition that characterizes the two degrees of freedom full system but that is not representative of the behavior of the single degree of freedom system may be at first deemed as a consequence of either the presence of dissipative forces between the two masses or of the presence of a sprung connection between the unsprung mass and the stator. Such connection would limit the vertical displacement of the pad thus forcing it into stability. This version is not realistic as this connection does not play any role in the stabilization of the system. In fact, it turns out that stability is induced by the interaction between the sprung and unsprung mass, together with the energy dissipation in the voice coil but only up to a certain point. This is visible in Figure 4.2 where a color-map root locus shows what happens when varying the sprung mass from a value of a few grams (shown in blue) to its real value of $m_s = 15.82 kg$ (in yellow). This process sees the root locus plot passing from a 1dof-like shape, very similar to what seen in Figure 2.10 to what seen in the previous plots in Figure 4.1. Thus, an increase in sprung mass causes the system's poles to shift deeper inside the stability region.

Figure 4.3 shows, instead, the evolution of the root loci when increasing voice coil damping. The value of suspension damping starts from zero, passes from the real configuration $c_{vc} = 220 Ns/m$, highlighted in red and then proceeds to a value of $c_{vc} = 4000 Ns/m$. It is interesting to evidence that the increase in damping seems to be beneficial for the poles of the unsprung mass. Looking to the sprung mass poles, instead, the opposite effect can be highlighted. It appears, in fact, that the poles shift towards the stability region for low values of damping but after a certain threshold the locus assumes a more arched "C" shape whose extensions protract more and more towards the imaginary axis. A crucial remark is that the

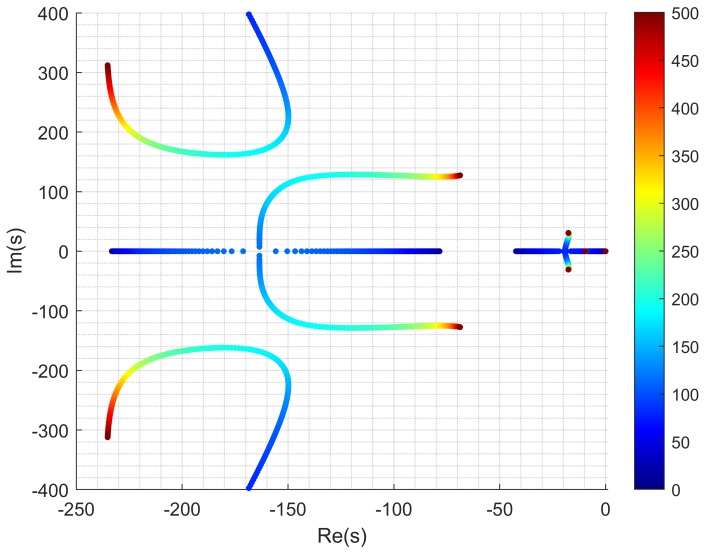

(a)

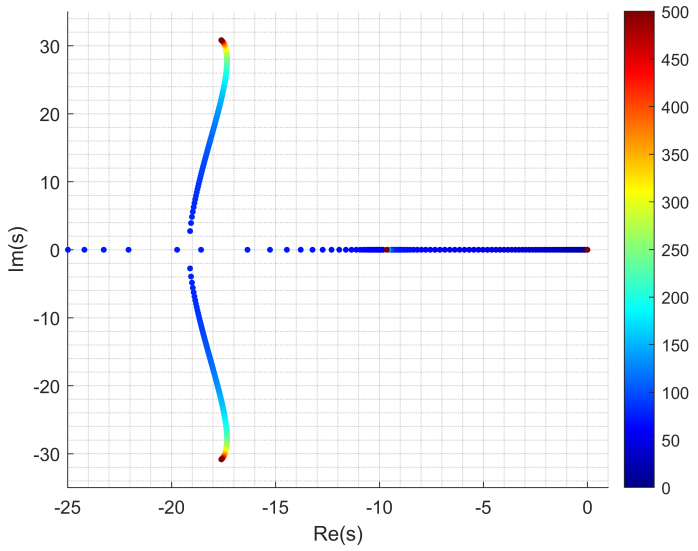

(b)

Figure 4.1: Root locus of the full system model with varying rotational speed $\omega[rpm]$ shown in the color bar (a) Poles of the unsprung mass (bigger C shape), poles of the first electrical branch on the left (b) poles of the sprung mass

locus of the sprung mass is progressively turning into the single degree of freedom root locus plot seen in Figure 2.10, so the system is converging to a single-degree of freedom like configuration due to the very high damping. The unsprung mass locus

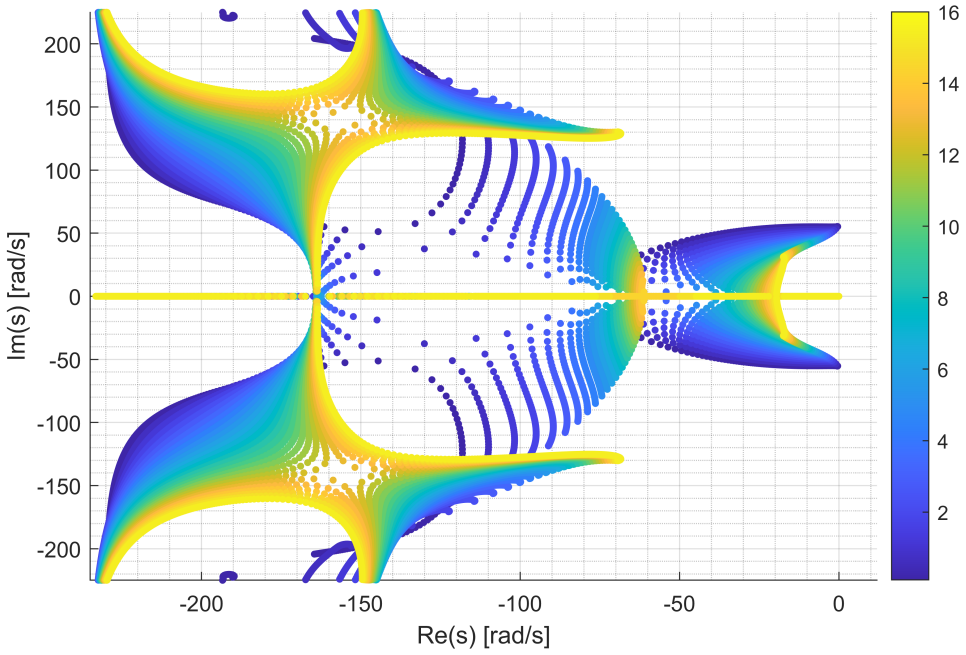

Figure 4.2: Root locus plot of the dynamic measuring device model. The color-map shows the evolution of the root locus when applying an increasing sprung mass. Unit of measure of the color-bar [kg] (velocities ranging in 0 to 1000rpm)

sees a complete change in shape, the initial C shape seen in Figure 4.1 gets further away from the imaginary axis, until it disappears, giving way for a new ellipsoidal poles region that arises only for a small range of dampings before disappearing giving way to the already seen single degree of freedom root locus. The evolution of the poles that are closer to the imaginary axis must receive particular attention, since their real part influences the system overall stability. Plotting the real part of such poles for all the analyzed values of damping should reproduce a plot similar to what seen in Figure 2.11. The result is displayed in Figure 4.4 and shows, the optimal damping value for the measuring device model. The minimum value of the pole's maximum real part is shown for a damping value of $c_{vc} \cong 205 Ns/m$. Thus, not only the dissipation in the voice coil is not directly involved in the stabilization of the system but, after a certain damping value it turns into a worsening factor. Resuming, in this paragraph, the stability of the two degree of freedom levitated system was investigated to establish what factors induce the stability that is not seen in the single degree of freedom system. Differently than expected, damping only plays a beneficial role in a narrow range of values and the stabilizing effect arises from the interaction between the two masses rather than dissipative forces.

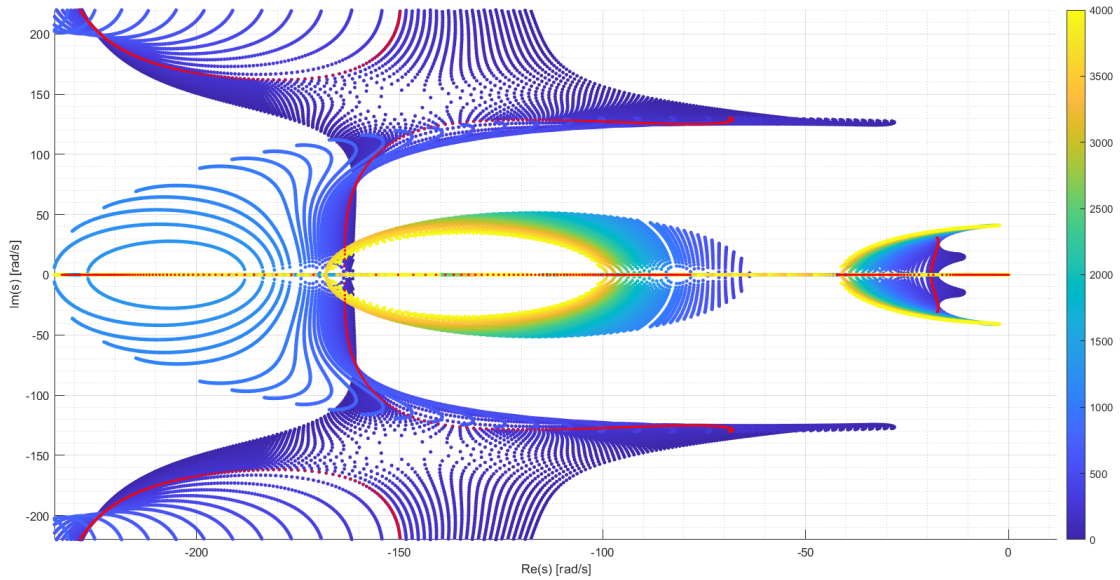

Figure 4.3: Root locus plot of the dynamic measuring device model. The color-map shows the evolution of the root locus when applying an increasing voice coil passive damping c_{vc}. Unit of measure of the color-bar [Ns/m] (velocities ranging from 0 to 1000rpm)

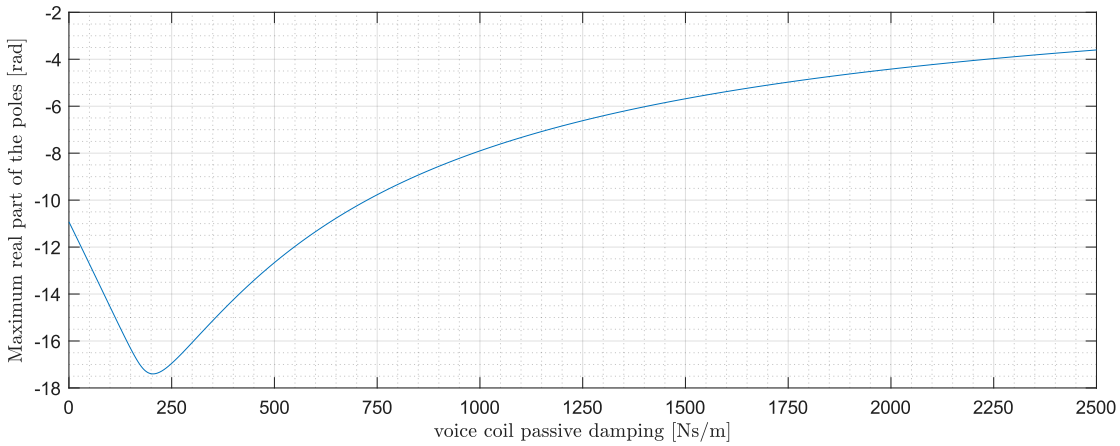

Figure 4.4: Real part of the pole closest to instability varying damping

4.2 Equivalent Damper

Numerical analysis of the measuring device model will be carried on parametrically, considering changes in the values both of track's rotational speed and suspension damping. Changes in suspension damping factor have been proven to influence the system performance and overall stability, as seen in the previous paragraph and in Figure 4.3. It was also seen how the entity of the sprung mass with respect to

the unsprung mass can affect the overall stability in Figure 4.2. While a change in sprung mass is feasible, it is less representative of a real possible case since the payload is usually a datum and not subject to heavy adjustments. A change in suspension damping is undoubtedly more interesting. Experimentally speaking, given that the addition of an adjustable damper on the dynamic device is not an easy task, it would be ideal to exploit the voice coil to actively reproduce the additional damping force on the two masses. Furthermore, given that the system has never been actively controlled, this process would be a first step to prove the feasibility of a feedback loop. The feedback line gain can be obtained by exploiting basic rules of applied mechanics. First of all one may unify the passive damping and the active damping contribution into a unique dashpot having c_{tot} damping coefficient which is the final desired suspension damping. Following the previous definition, the total damping can be expressed as follows.

$$c_{tot} = c_{vc} + c_{sim} \tag{4.1}$$

where c_{vc} is the already known voice coil damping factor, while c_{sim} is the additional damping contribution that must be actively simulated. Let v_{rel} be the relative velocity between the sprung and unsprung mass, expressed as

$$v_{rel} = \dot{z}_{us} - \dot{z}_s \tag{4.2}$$

The active force component at the ends of such dashpot would be the following.

$$F_{eq} = c_{sim} \cdot v_{rel} \tag{4.3}$$

Remembering what seen in equation 3.2 and hereby reported for clarity, the voice coil force is directly proportional to the current flowing through its windings, following the producer's indications.

$$F_{vc} = K_m \cdot i_{vc}$$

Thus, the 4.3 can be rewritten as follows.

$$K_m i_{vc} = c_{sim} \cdot (\dot{z}_{us} - \dot{z}_s) \tag{4.4}$$

At this point, by simplistically following Ohm's equation, one can write the following equations.

$$i_{vc,ss} = \frac{V}{R_{vc}}$$

$$K_m \cdot \frac{V}{R_{vc}} = c_{sim}(\dot{z}_{us} - \dot{z}_s) \tag{4.5}$$

Finally, the voltage that must be provided to the voice coil is

$$V = c_{sim} \cdot \frac{R_{vc}}{K_m} \cdot (\dot{z}_{us} - \dot{z}_s) \tag{4.6}$$

$$(c_{sim} = c_{tot} - c_{vc})$$

A big approximation has been made when considering the instantaneous voice coil current to be equal to its steady state value, since a sudden change in input voltage does not instantaneously reflect in a change of voice coil current. Thus the dynamics of the voice coil RL electrical subsystem is completely neglected. The effect is that, mostly when working at high frequency and high requested forces, the actual force exerted by the actuator will be very far from the desired value. A possible way to approach this issue would be that of applying a nested control loop that can achieve the desired current behavior using input voltage as control variable. Figure 4.5 shows the Simulink system containing such the

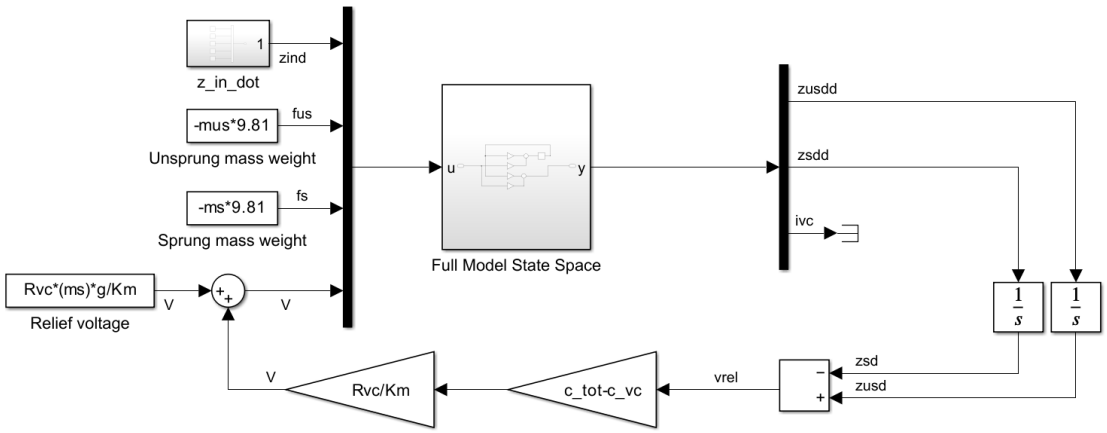

Figure 4.5: Simulink model with simulated damping feedback line

fictitious damper feedback line. The inputs fed to the system are the track vertical velocity, seen in the previous chapter, the static sprung and unsprung weight forces and voice coil relief voltage needed to decouple the two masses.

4.3 Sensitivity analysis

The dynamics of the system can be further explored through sensitivity analyses. These tools allow to show how changes in parameters characterizing the system can affect the system's response, in particular the accelerations of the two masses. This approach becomes especially helpful when circumstances prevent the straightforward application of a frequency response function. For instance when there

are uncertainties regarding the nature of the excitation's frequency content. Two main parameters can be identified at this point to have a crucial role in impacting the response of the measuring device, the first is the damping whose impact on the stability was already analyzed in the parametric root locus. The second one, also involved in the previous root locus analysis is the track's rotational speed. The following paragraphs deal with the impact of such parameters on the system's sensitivity.

4.3.1 Variations in damping

The equivalent damper effect represents a possibility to introduce varying values of damping in the real test bench system. Of course, in this merely numerical site, it is possible to check for the compliance of the simulated damper with respect to a system featuring a real passive damping c_{tot}. A first way to assess such compliance would be that of performing many time simulations and extrapolate the steady state acceleration response amplitude of the system both for the simulated damper and for the actual damper. Figure 4.6 contains the result of such preliminary

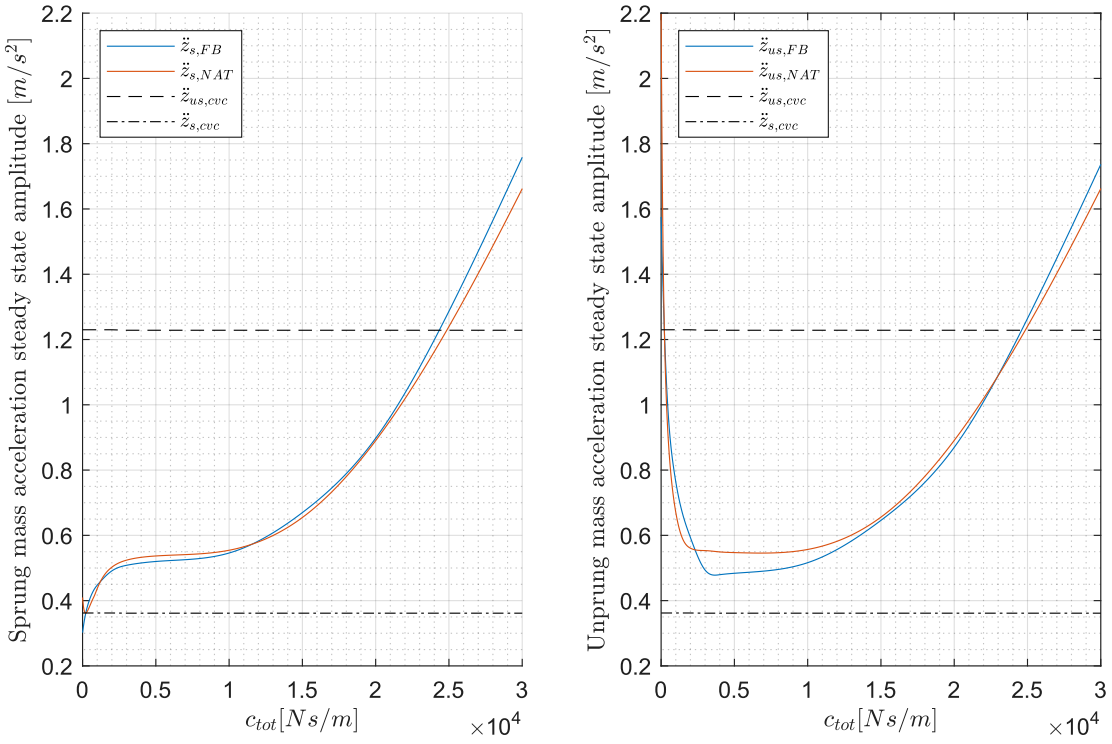

Figure 4.6: Sensitivity analysis comparison between sprung (left) and unsprung (right) steady state acceleration responses for the simulated damper (blue) and modified system with actual passive damper (orange). Nominal speed 500rpm. Excited by track irregularities.

sensitivity analysis. In particular, it shows the sprung and unsprung acceleration amplitudes at steady states in the left and right plot respectively. The excitation consists in the ground irregularities vertical velocity only. A very good compliance can be evidenced between the response of the system with simulated damper through the feedback line and the modified system with the real passive damper. In the same plot, the two black horizontal axes represent the acceleration values for both the sprung and unsprung mass working with a passive damping value $c_{vc} = 220Ns/m$. It can be noticed how the increase of damping produces worsening effects on the sprung mass acceleration amplitude for almost the entire analyzed range. A zoomed view of the left plot is displayed in figure 4.7 where a minimum

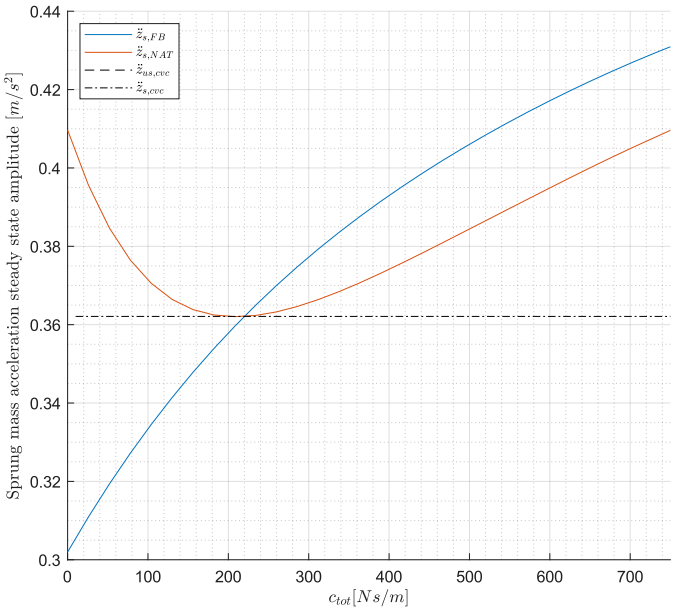

Figure 4.7: Zoomed view of the sprung mass sensitivity

point for the steady state response can be spotted around the value of voice coil passive damping $c_{vc} = 205Ns/m$. The same damping is that in correspondence of which the minimum vicinity between the root locus and the unstable region is witnessed. In this low damping area, the fed back system does not show the same behavior as the natural one, in fact, for such system, the increase in damping proves to be always disadvantageous.

4.3.2 Variations in speed

The influence of the rotational speed of the track is also an interesting effect to be evaluated. In the same way as done for the damping, various speeds are analyzed to extrapolate the sprung and unsprung response amplitudes when the system

is excited by the sole influence of the track irregularities. Figure 4.8 depicts the sensitivity of the sprung and unsprung mass in a rotational speed range going from 0 to 1000 rpm. Notice that levitation happens only above 200rpm, thus the values below such speed are not meaningful for the real system. The numerical model permits non zero values of accelerations of both the masses, even when the system is operating at speeds below the levitation threshold of the physical system. This occurrence arises from the extension of the air gap model linearization to negative air gap values. Therefore, the Simulink solver consistently produces accurate algebraic solutions to the model's equations that, even if mathematically correct, lack of physical significance. What emerges from the figure is that the sprung mass acceleration has a much lower amplitude with respect to the unsprung's. The sprung mass acceleration amplitude shows an increasing behavior up to around 500 rpm after which the trend is reversed and the amplitude is reduced. This phenomenon arises because the excitation frequency originating from track irregularities is excessively high to be felt. The sprung mass acceleration also shows this behavior but the modulus of the acceleration raises up to 4 times more than the sprung mass' since it has almost one fourth of the inertia. Anyway, after 900rpm, also the unsprung mass sensitivity shows a decrease.

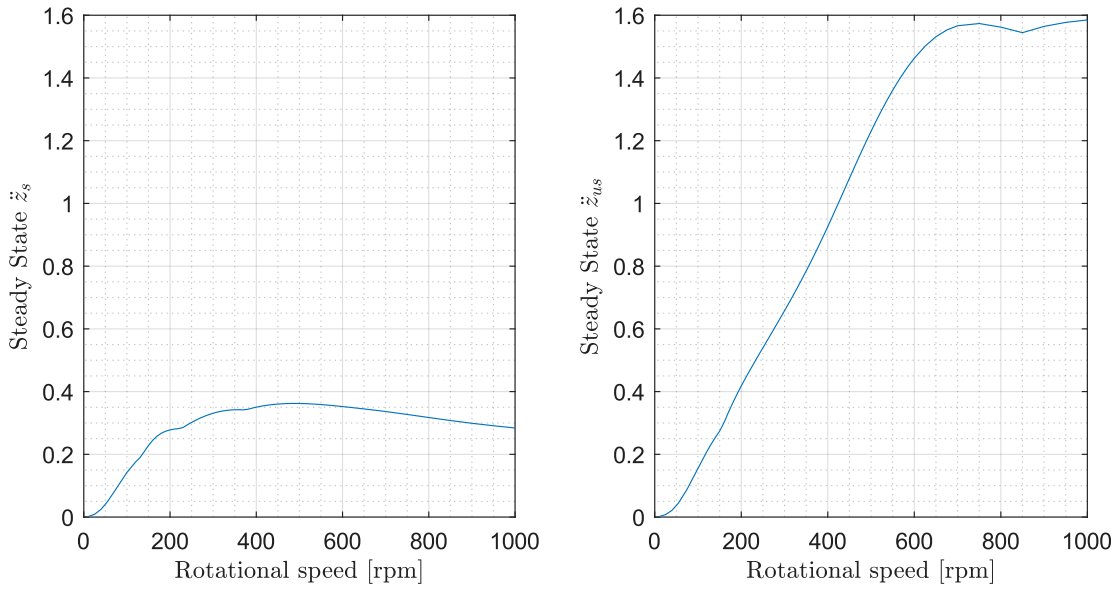

Figure 4.8: Sprung and unsprung mass sensitivity varying rotational speed

4.3.3 Variations in speed and damping

Having examined the isolated effect of variations of speed and damping it is interesting to present a comprehensive 2-D map illustrating the system sensitivity

across a wide spectrum of speeds and damping combinations. Conducting such two-dimensional sensitivity analysis necessitates a grid of points cover as densely as possible, the parameter domain of interest. For each one of these points, a time simulation is executed to capture the steady state amplitude of the acceleration response. As covered in the stability analysis, a value of suspension damping around 3000Ns/m already brings the behavior of the system back to something very similar to a 1-DOF. It's intriguing to capture the behavior of the system below this value, setting the domain within a range of voice coil passive damping between zero and 3000 Ns/m. The grid of points exploited for such stability analysis is displayed in Figure 4.9. Significantly, the primary attention was directed towards the speed

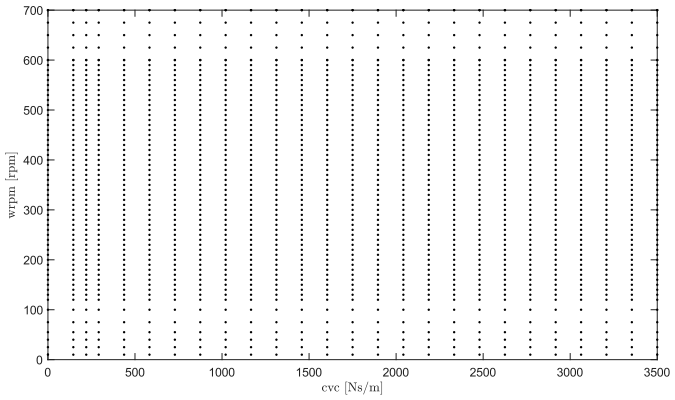

Figure 4.9: Grid Points for sensitivity analysis

range between around 200 to 600rpm since levitation does not occur below this lower threshold and the rotational speed is preferably maintained below 600 rpm with the possibility of reaching the maximum rated speed of 700 rpm. Figure 4.10 shows the unsprung mass sensitivity of a model including a real damper (damping in the state space matrices) (a) vs the sensitivity of the model with simulated damper (b) (damping through feedback line). Noticeably, the two sensitivities are very similar in shape. In general two horizontal zones of enhanced sensitivity can be highlighted in proximity of a rotational speed of 200rpm and 400rpm. The unsprung mass shows also quite large response in high speed and low damping configuration. It is in this latter region that one can spot the largest difference between the simulated and real damper. As mentioned earlier, in the high speed region the compliance between the two systems is depleted due to the kind of feedback that the numerical model is using to control the damping force, which, as mentioned, simplistically exploits the assumption of null inductance of the voice coil electrical subsystem. Such assumption, in fact, does not hold when dealing with higher frequency ranges. Figure 4.11 presents the results regarding the sensitivity of the sprung mass. In this case, the two plots exhibit a greater compliance and the

dissimilar region discussed for the unsprung mass cannot be observed here since it is either absent or at least much less noticeable. This could be attributed to the much more significant inertia of the sprung mass that renders the effects of the non-correspondence in damping force less pronounced. Evidently, the regions of enhanced sensitivity persist around the velocity ranges of 200 and 400rpm and so they do along the whole range of damping values analyzed.

Stability

As previously observed, the interaction between the two masses ensures that the system's poles are placed well within the stability region. Nevertheless, it is important to evidence that this does not imply the system's stability in all possible configurations. While root locus plots offer a detailed evaluation of the system overall stability, they do not provide a straightforward reading of the parameters combinations that might ultimately lead to instability. Thus those plots provide a comprehensive depiction of the system's behavior without offering very specific insights on the precise conditions under whom instability may take place.

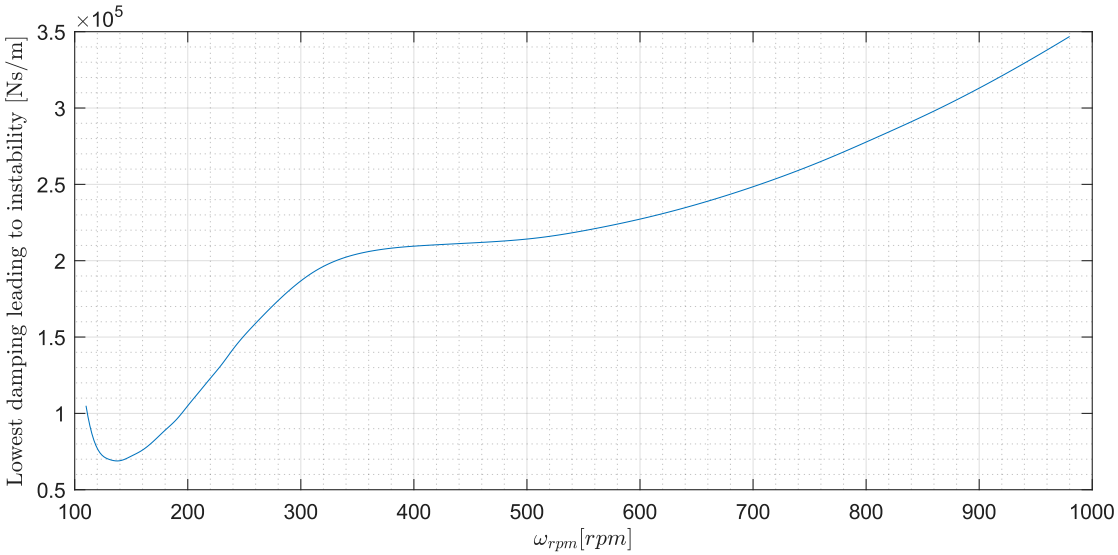

Figure 4.12: Threshold of instability, shows the lowest value of suspension damping that leads to instability for each rotational speed

By now, it is very well known that the imposition of very large values of dampings can lead the system to a behavior similar to that of a single degree of freedom one. As a consequence, such adjustment, can also drive the system's poles into the instability region. An analysis was undertaken to check whether such occurrence can be expected during operation and, if so, to determine the specific operating

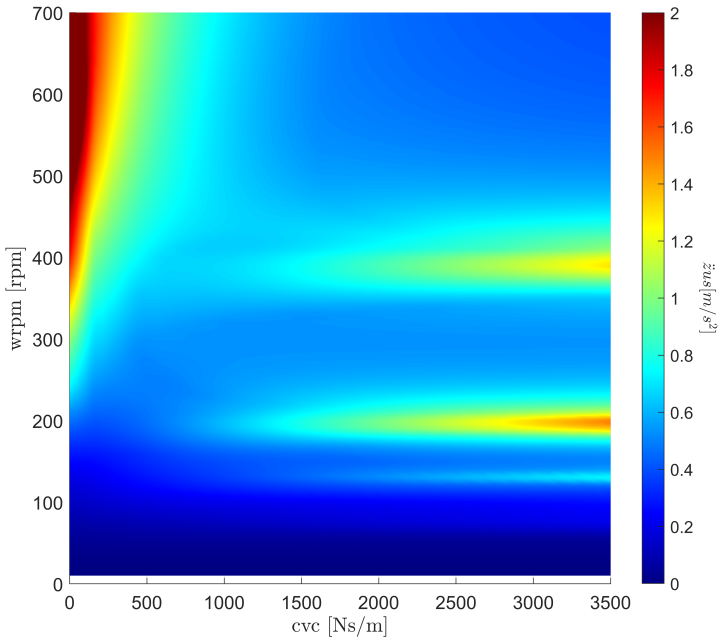

(a)

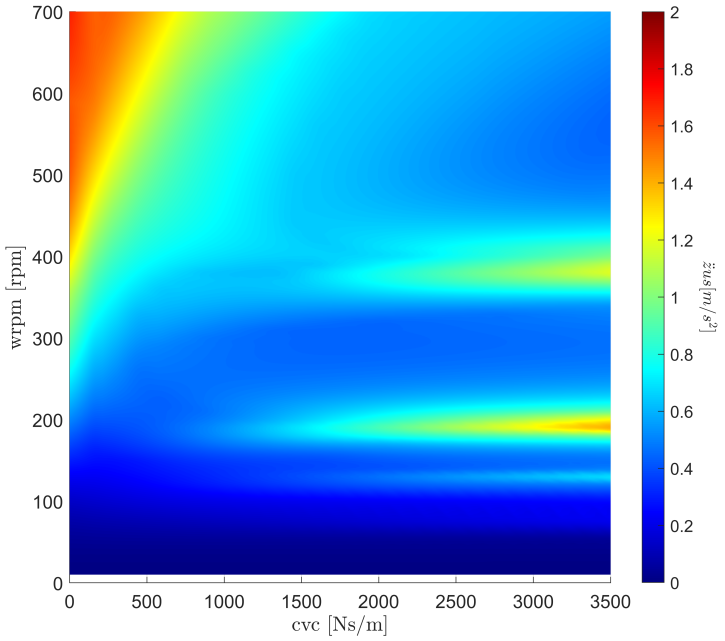

(b)

Figure 4.10: Unsprung mass sensitivity map. (a) Sensitivity of a naturally damped system, (b) Sensitivity with simulated voice coil damping

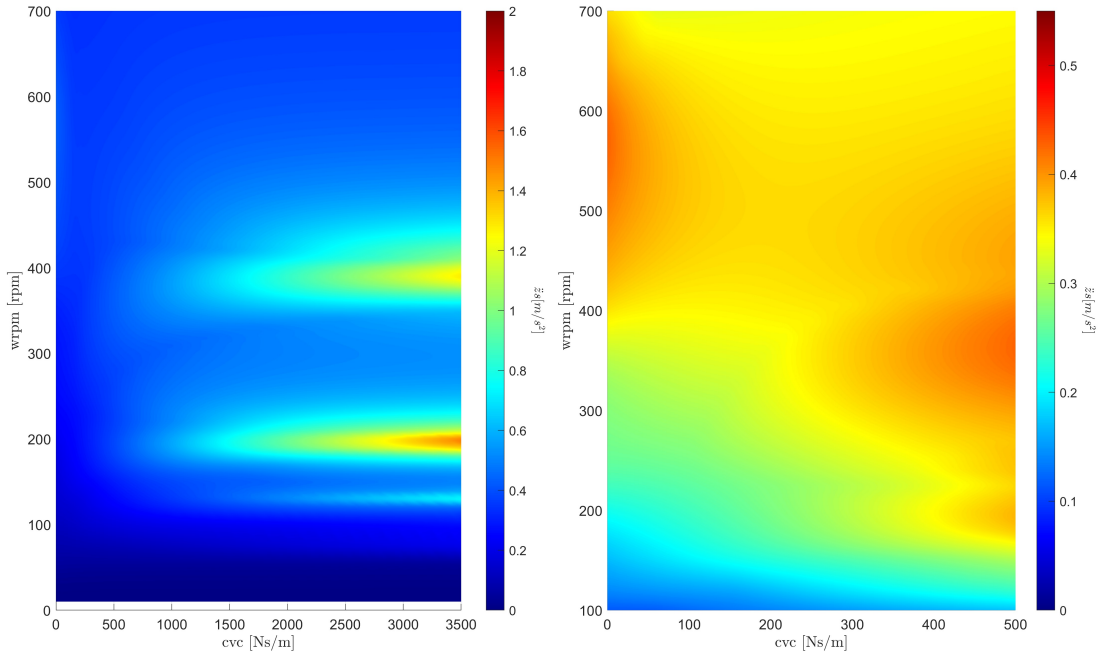

(a)

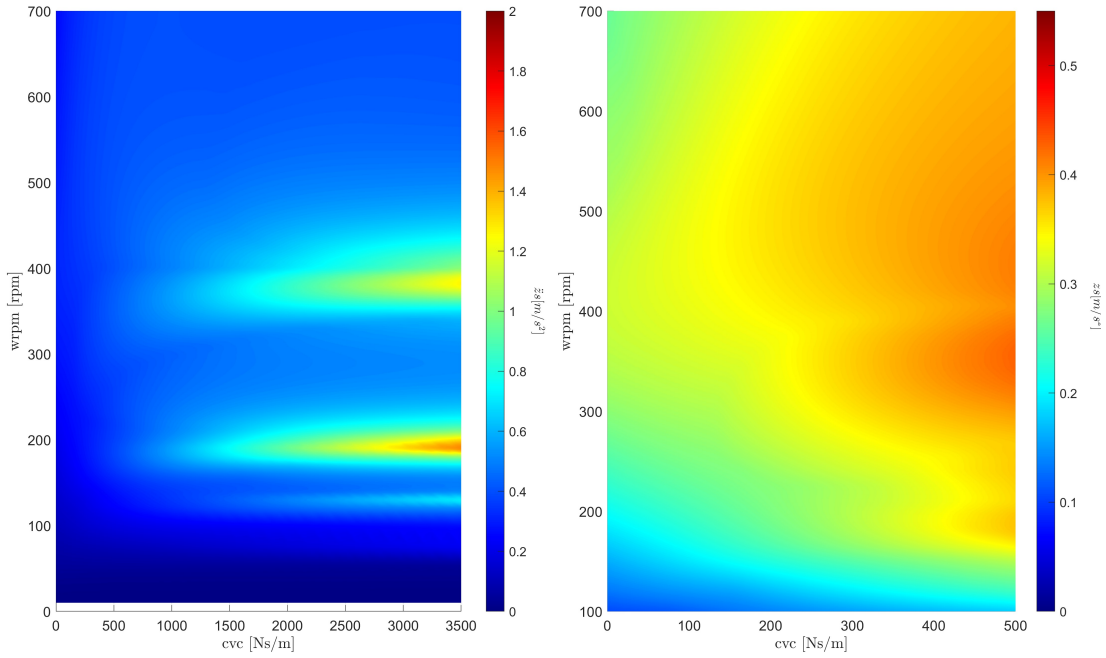

(b)

Figure 4.11: Sprung mass sensitivity maps. The maps on the left show the full range. On the right, zoomed view over the 0-500Ns/m in the 100 to 700rpm band. (a) Sensitivity of a naturally damped system, (b) Sensitivity with simulated voice coil damping

regimes where it might manifest. Figure 4.12 contains a representation of the instability threshold within the parametric instability field. Such curve shows the minimum suspension damping that makes the induces the system to instability for various speeds. One can notice that this curve is clearly placed at very high damping levels, exceeding the range explored in Figure 4.10 and Figure 4.11 by at least one order of magnitude. An extended sensitivity analysis covering a broader spectrum of damping values was conducted. The results are plotted in Figure 4.13, where they are superimposed with the previously mentioned instability threshold plot. Such results were produced by stretching over the new damping range the same grid of data point used for the restricted range sensitivity map. Notably, only one plot is presented regarding this extended sensitivity analysis, differently than the four depicted earlier. This is not a case since in this very high damping region, there is a negligible difference between the sensitivities of sprung and unsprung masses as they effectively behave as one. Furthermore, at extremely high damping values, the feedback-simulated damper closely resembles the behavior of the real one. Interestingly, the two horizontal regions showing enhanced sensitivity persist in this field always at 200 and 400 rpm. In addition, one can spot a very extensive area of heightened sensitivity below 200 rpm. Such region lacks of physical relevance since, as mentioned, levitation occurs only above 200rpm

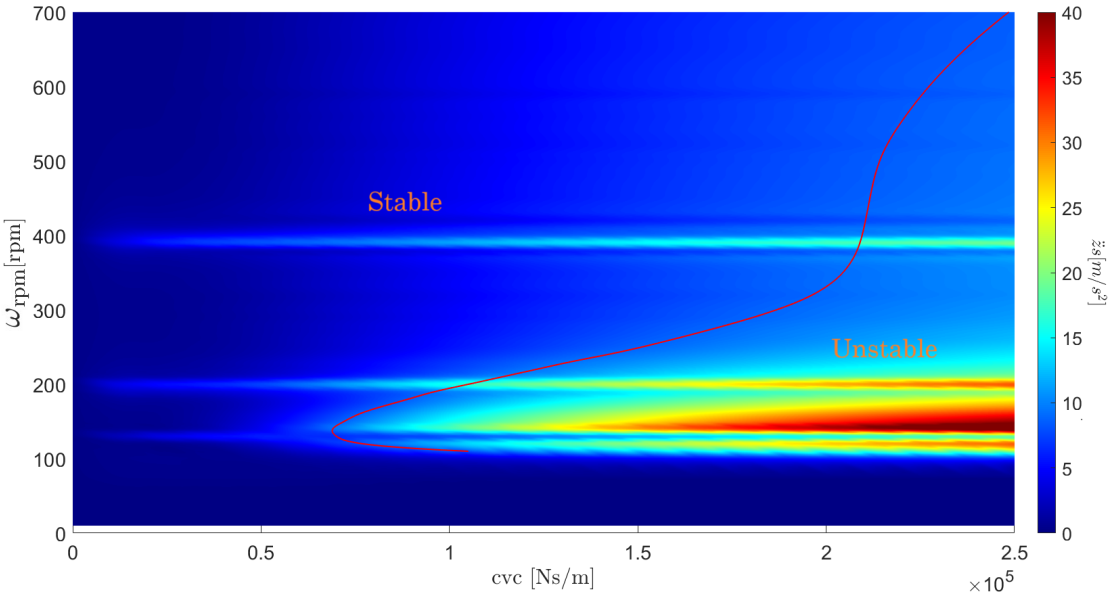

Figure 4.13: Threshold of instability on the sensitivity map, shows the lowest value of suspension damping that leads to instability for each rotational speed

4.4 Frequency Response Functions

Finally, in this overview concerning the system's stability and general behavior, Frequency Response Functions (FRFs) are employed to evaluate the impacts that various types of inputs can have of the system. Deriving frequency response functions in the practice, especially for the inputs that characterize this particular system, proves to be quite challenging due to the need for a comprehensive and precise knowledge about both the excitation and the response. Speaking about the response aspect, no issues arise as long as the primary interest revolves around acceleration, which is the case since all of the analyses are focusing on passenger comfort-related aspects. Acceleration is directly measured by two accelerometers that are positioned on the sprung and unsprung masses. These accelerometers serve as the unique source of direct measurement of kinematic parameters. The knowledge about the track's vertical velocity input is solely based on measurements that were conducted statically as mentioned in the previous chapters. Furthermore, it relies on the approximation of a Fourier series comprising five sine waves.

Thus, given that to the best knowledge the excitation has only five sinusoids, when running the test-bench at constant rotational speed, a discrete set of only five frequencies, is excited. Consequently, a comprehensive representation of the system's response across all frequency ranges cannot be achieved. It is important to avoid misunderstanding in this regard. The actual track does not simply consist of such a limited number of waves. The true track geometry can be seen like a Fourier series composed of an infinite number of sine waves, each one having distinct frequency amplitude and phase. Thus, the true geometry effectively triggers a wide spectrum of frequencies and, having a complete understanding of it would indeed allow to depict the correct frequency response function. Therefore, with the limited knowledge of the Fourier transform of the track irregularities, there's an incorrect clustering of response amplitude, which is proper of an entire range of frequencies, into a single frequency value, leading to a significant overestimation of the response. One can refer to Figure 4.14 which illustrates the Fourier transform of the ground irregularities employed in the simulations

When discussing voltage, instead, ideally, no issues should arise regarding the correct knowledge of the excitation since voltage serves as the actual control input to the system. It can be easily transformed into a chirp signal to construct the desired response. However, the constant relief voltage acting on the voice coil presents potential risks of interfering with the generation of the intended chirp signal, once again leading to a mismatch between the actual excitation and the desired one. It is important to emphasize that these issues appear during the evaluation of the test-bench responses. From a numerical standpoint, there are no issues to obtain all the response functions given that the inputs can be whatever.

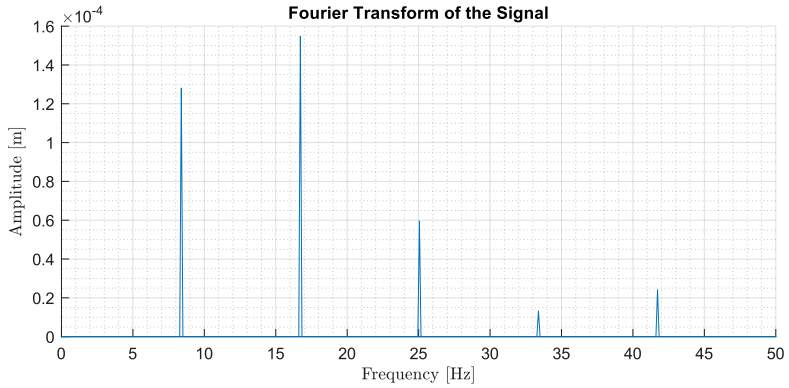

Figure 4.14: Fourier transform of the ground irregularities

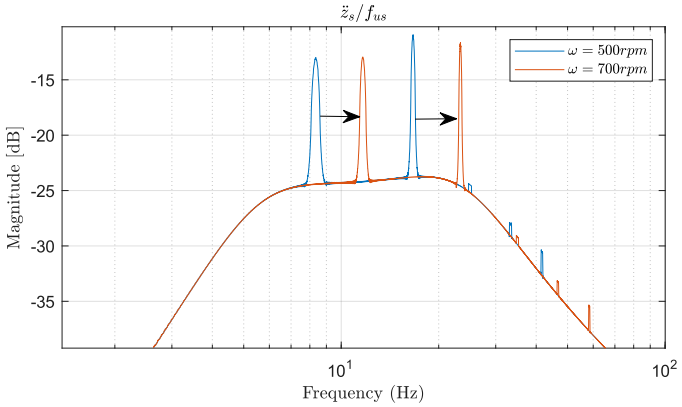

Figure 4.15: Effect of ground irregularities on FRFs varying speed

It is worth noting that the input signal is a chirp signal with characteristics specified in Table 4.1. In addition, it's important to acknowledge that within this numerical site one can analyze the response with or without considering the effect of ground irregularities. Responses to track vertical velocity do not encompass the effects of ground irregularities, while all the other responses take into account such effects superimposed to the chirp excitation. One important aspect to be emphasized concerns the appearance of ground irregularities-related peaks in the frequency response functions. When applying a chirp perturbation to an input (with the exception of ground vertical velocity), we consider its amplitude and frequency content as the sole input to the system, and the response is collected as the result of such excitation. The presence of ground irregularities is not included on the excitation we are focusing on but it is inherently present. Therefore, in vicinity of the frequencies corresponding to the Frequency content of the ground irregularities, the actual disturbance experienced by the system is the sum of

the contribution coming from the chirp signal and the contribution of ground irregularities. As a consequence, the computed response around such frequencies tends to be overestimated as shown in Figure 4.15, as it attributes the response caused by these two excitations, solely to the input signal under analysis. It is clear that an increase the rotational speed provokes a rise in excitation frequencies and a consequent shift of the peaks. Furthermore, if the amplitude of the chirp signal is increased, the effect of the ground irregularities is comparatively more significant. Neglecting them in the input vector amplifies their effects on the peaks of the frequency response functions. Figures 4.17, 4.18, 4.19 and 4.20 show the sprung and unsprung mass acceleration frequency response functions to each input. Having dealt with the effect of suspension damping on system sensitivity it is interesting to complete such discussion by displaying the effect of such parameter in frequency response functions. Figure 4.16 shows the effect of increasing suspension damping from the FRF standpoint and, also in this ambit, the evolution of a two degree of freedom response to a single degree of freedom like one with one resonance peak can be seen. Notice also the presence of three invariant points in the frequency response function.

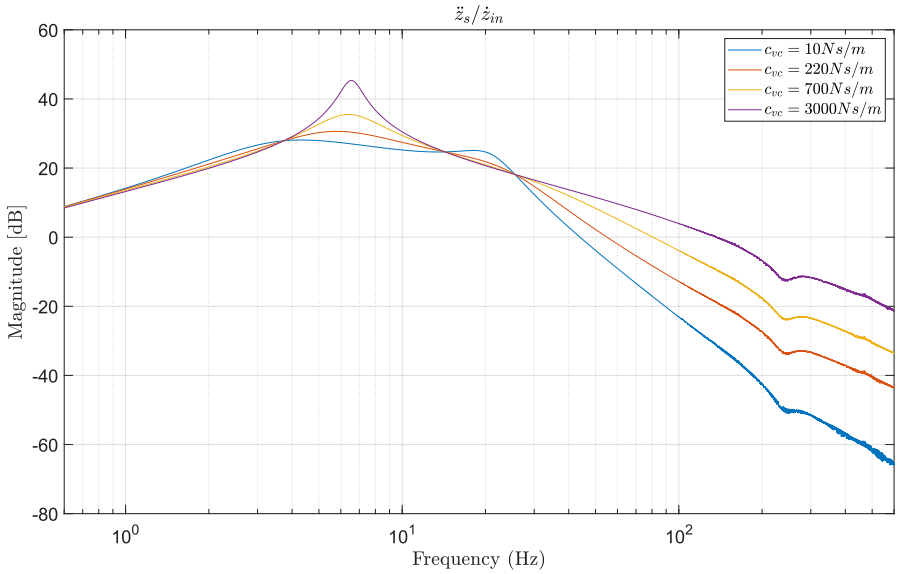

Figure 4.16: Track vertical velocity vs sprung mass acceleration FRF varying suspension damping

Parameter	Value	Unit
Track vertical velocity chirp amplitude	0.002	m
Unsprung mass chirp force amplitude	10	N
Sprung mass chirp force amplitude	10	N
Voltage chirp amplitude	5	V
Rotational speed	500	rpm
Initial frequency	0.001	Hz
Target frequency	1000	Hz
Target time	60	s
Sweep time	60	s
Initial phase	$\pi/2$	rad
Sampling time	$5 \cdot 10^{-5}$	s
Simulation time	100	s

Table 4.1: Parameters of the chirp signals for FRFs obtainment

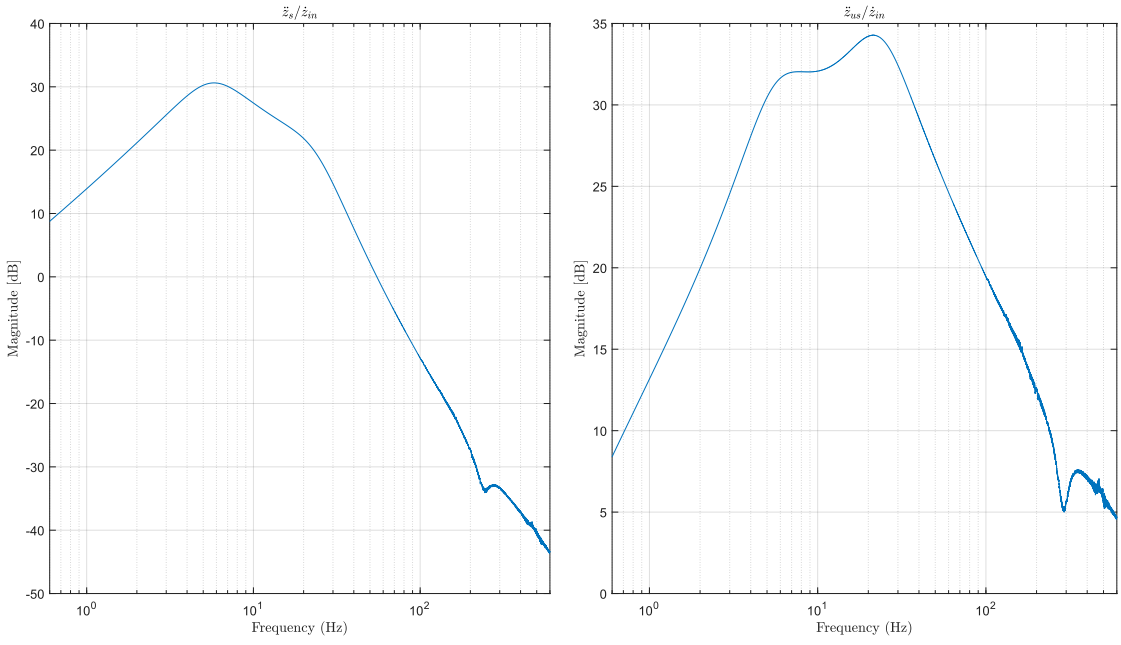

(a) (b)

Figure 4.17: Sprung (a) and Unsprung (b) mass acceleration frequency response to track vertical velocity

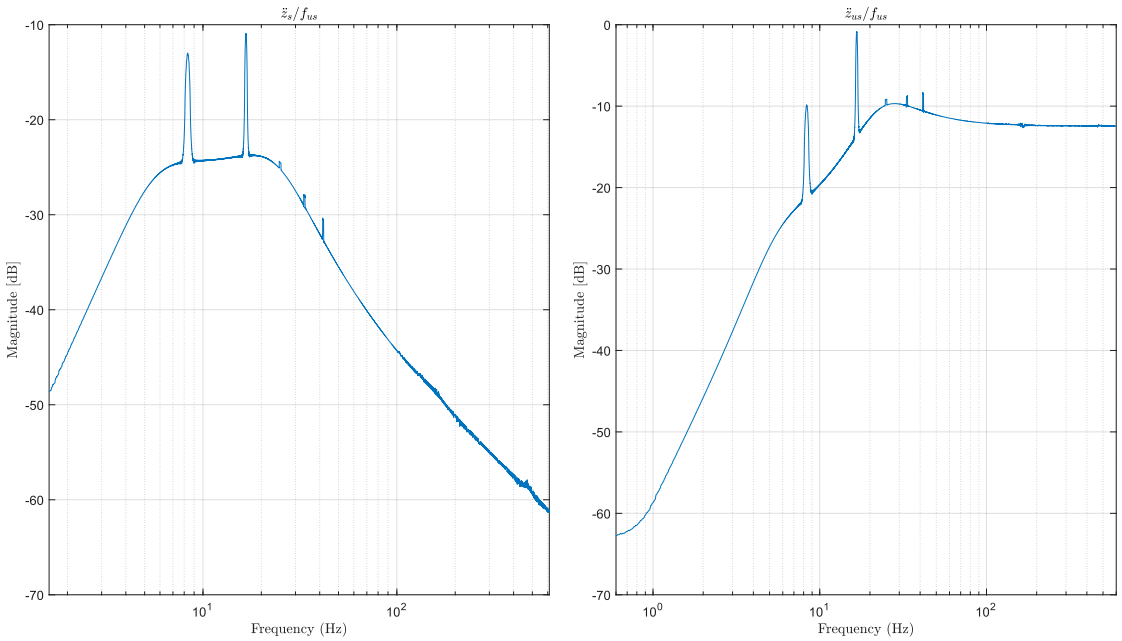

(a) (b)

Figure 4.18: Sprung (a) and Unsprung (b) mass acceleration frequency response to external force on the unsprung mass

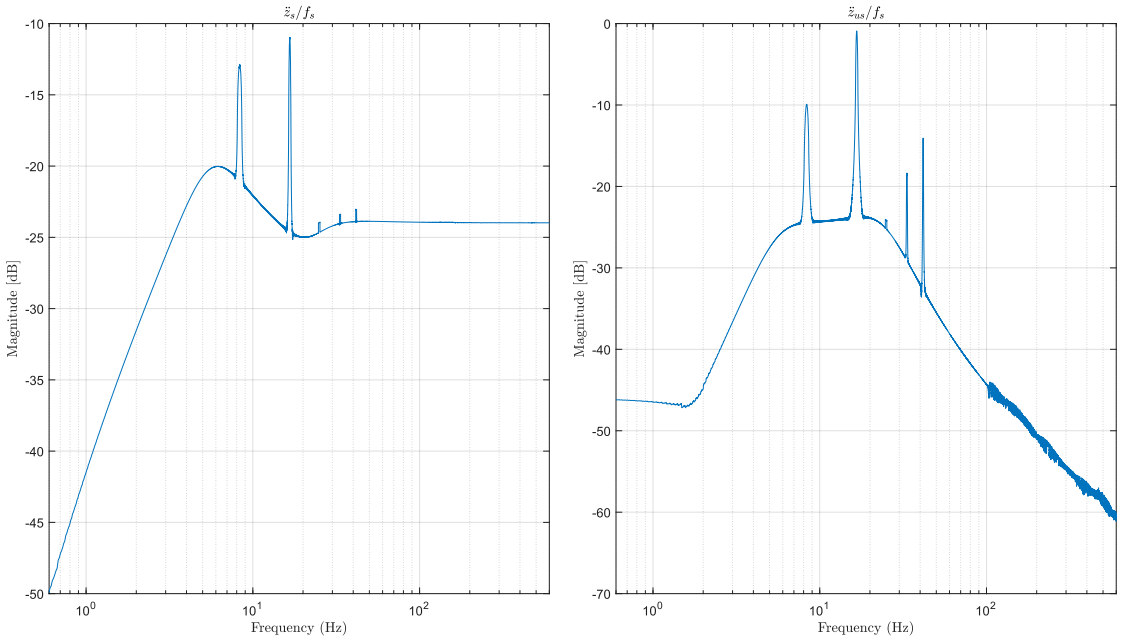

(a) (b)

Figure 4.19: Sprung (a) and Unsprung (b) mass acceleration frequency response to external force on the sprung mass

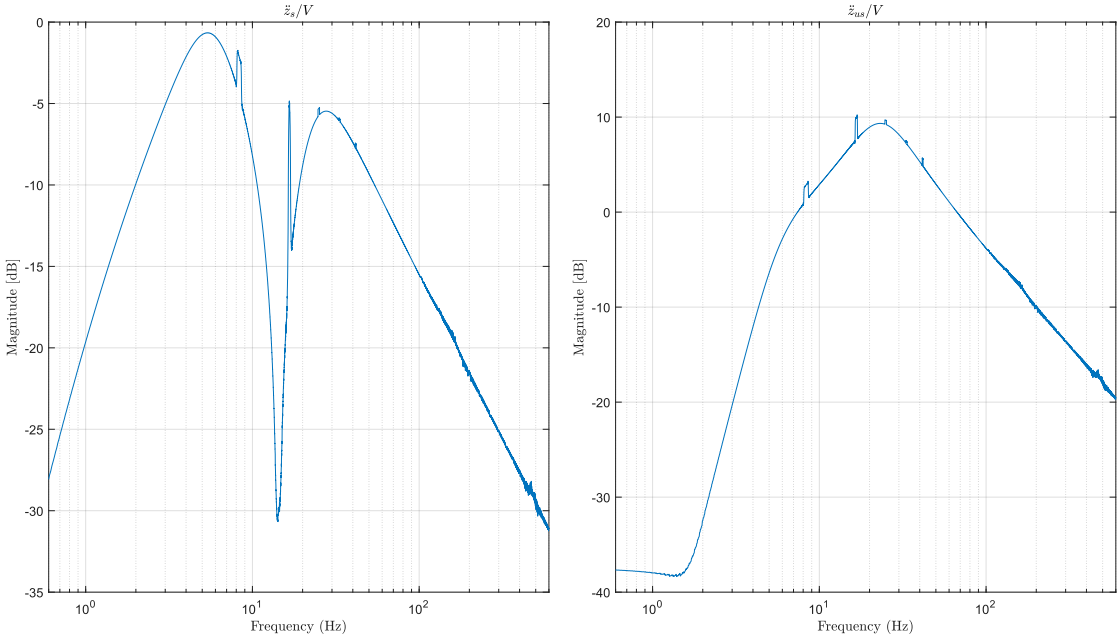

(a) (b)

Figure 4.20: Sprung (a) and Unsprung (b) mass acceleration frequency response to input voltage

Chapter 5

State estimation

In a numerical environment, obtaining feedback signals is a very trivial matter, as demonstrated when adopting the feedback line to simulate additional damping. However, when dealing with the actual physical system such process is very far from being trivial. The apparent simplicity of the feedback loop for the simulated damper hides the actual challenge that one would face when applying it to the real system. In fact, it relies on a relative speed dependent feedback signal even though the only measured parameters from the device are the accelerations of the two masses. One may argue that velocity could be obtained by integration of these acceleration signals, but in reality this approach does not provide accurate velocity estimate due to the inherent non-idealities in the measured variables and drifts. This does not mean that the measured signals are so wrong that cannot be relied on but means that they cannot come as the sole source of information in deriving other parameters. To address this issue, one potential solution is not to rely solely on sensor-derived signals but to somehow integrate them with the knowledge coming from the mathematical model. In this pursuit, this chapter aims to give an overview on how such fusion of information is achieved through the use of a Kalman filter. Furthermore, it will also highlight the characteristics of the reduced mathematical model and its employment for state estimation purposes.

5.1 Kalman filtering

Kalman filter is the most popular algorithm used to fuse together mathematical expectations coming from a model and real measurements coming from sensors. It is not in the scope of this work to give a comprehensive mathematical demonstration of how the filter works, for such information one can refer to [13]. A very brief overview on the logic laying behind is provided following *Faragher* [14]. First of all, to introduce the process, we need to de-contextualize the Kalman filter forgetting

for a moment about the dynamic measuring device. We have to refer to a simple translating mass over a plane of which we want to know the position at various time steps knowing the possible range of force that such mass may experience (thus the acceleration) and a measured position that is subject to a certain error. Kalman filter theory is based on the assumption that all uncertainties about measurements and estimations can be taken in to account with Gaussian probability density functions. Such curves are of particular interest since a product of two Gaussian curves having each one their own variance and expected value produces a third Gaussian curve having a third couple of variance and expected value. This lays the foundations for an iterative procedure to be set up as the algebraic complexity of the problem remains unvaried going on from a time step to another.

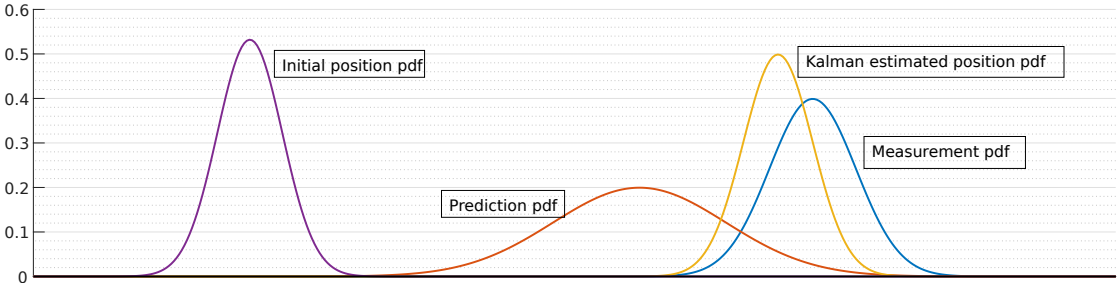

Figure 5.1: Kalman filter working principle

The position of the mass at the initial time is known with a reasonable accuracy and, thus, it is only described by a very narrow Gaussian PDF and the mean value is considered as the actual position at that time instant. When the mass starts to move with non zero initial velocity it can be subjected to an unknown amount of force ranging between a known minimum and maximum. Associated to such force there is again a probability distribution which is once more assumed to be a normal distribution and can be referred to as process noise, as it contains the uncertainties related to the amount of non-measured actions the system is being affected by.

Generally, the introduction of process noise allows also to represent mismatches between the real behavior and the model's behavior that would otherwise require much more complex models to be captured. Following these statements one may obtain, based on the mathematical model, on the uncertainty about the process (in the case of the translating mass, the forces) and on the uncertainty about the initial position, a further Gaussian curve with a certain variance whose mean value represents the best guess from the mathematical side for the new position of the mass at the following time step. The equation of such Gaussian curve is written in Equation 5.1.

$$g_{prediction}(x, \mu_1, \sigma_1) = \frac{1}{2\pi\sigma_1^2} e^{-\frac{(r-\mu_1)^2}{2\sigma_1^2}} \tag{5.1}$$

The term x is the position, μ_1 is the mean value associated with the probability density function and σ_1 represents the standard deviation. For example, thinking to the moving mass case, if the process noise is expected to have a positive mean value it means that it is very likely that a positive force that accelerates the mass will appear during the time step. As a result, the Prediction Gaussian will have a mean value positioned further away from the initial position with respect to where it would be paced if the process noise mean value was zero. Other than the prediction Gaussian, a measurement Gaussian curve contains information coming from the utilized sensor. The measurement's expected value and variance will depend on the sensor's precision and accuracy and, such uncertainty contribution, is the enclosed in the measurement noise. The measurement Gaussian curve equation is the following

$$g_{measure}(x, \mu_2, \sigma_2) = \frac{1}{2\pi\sigma_2^2} e^{-\frac{(r-\mu_2)^2}{2\sigma_2^2}} \tag{5.2}$$

Thus, two Normal probability density functions describe the best guess (mean value) and the accuracy of such guess (related to the variance) obtained from both the mathematical model prediction and from the measurement data collection. At this point, exploiting the mentioned properties of Gaussian curves, one can simply multiply the two to obtain a third Gaussian curve having a fused mean value and variance and it is the most reliable guess for the actual position of the mass as it comprehends all available information.

$$g_{fused} = g_{prediction} \cdot g_{measure} = [...] = \frac{1}{2\pi\sigma_{fused}^2} e^{-\frac{(r-\mu_{fused})^2}{2\sigma_{fused}^2}} \tag{5.3}$$

With

$$\sigma_{fused}^2 = \frac{\sigma_1^2\sigma_2^2}{\sigma_1^2 + \sigma_2^2} \tag{5.4}$$

$$\mu_{fused} = \frac{\mu_1\sigma_2^2 + \mu_2\sigma_1^2}{\sigma_1^2 + \sigma_2^2} \tag{5.5}$$

This process can thus be resumed in two main steps:

- Prediction stage: in which the mathematical and measurement Gaussian curves are obtained;

- Measurement update stage: in which the two PDF are merged together are merged to create the starting distribution for the next time step estimation.

This very simple example is detailed enough to get the working principle of this kind of filter. It is not in the scope of this thesis to provide a complete explanation

of the algorithm as it will be just used as a tool. For more insights on the Kalman filter's theory refer to [13].

5.2 Reduced Model

The introductory paragraph about Kalman filtering provided a de-contextualized sight of the logic behind data fusion for parameters estimation. Actual Kalman filter prediction and measurement update stage are of course way more complex when dealing with big systems and they resort to matricial formulation. Running a Kalman filter live means that the processor must deal at each time step with a requested computational effort that depends on the size of the model. In this case the model under analysis comprises a number of 10 states and 4 inputs and three outputs, thus the processor has to deal with a 100 element dynamic matrix A_{full}, a 40 elements input gain matrix B_{full} and a 30 elements output gain matrix C_{full}. Considering that the prediction stage has to occur thousands of times per second, even removing one state could result in an important upgrade towards optimization. Recalling what discussed in the Numerical modelling chapter, the electrodynamic levitation suspension may be substituted by a spring of stiffness k_p as expressed in equation 2.22. Figure 5.2 contain a schematic representation of the modified model.

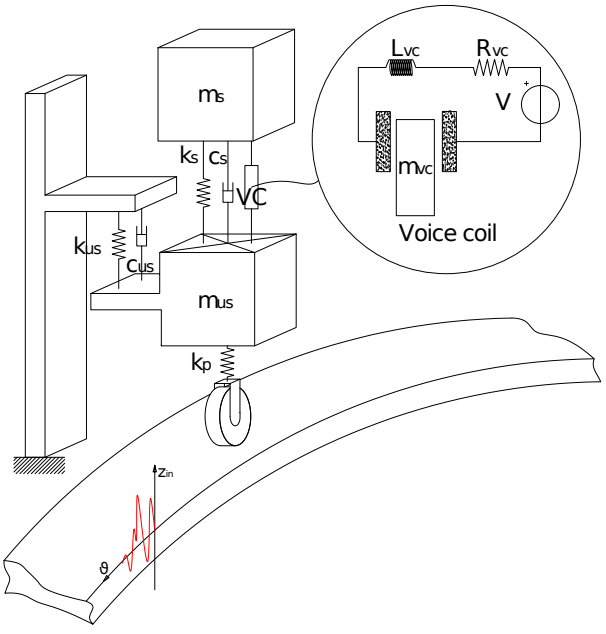

Figure 5.2: Reduced model schematic representation

This simplification introduces a relevant reduction of the state space matrices sizes as the four states connected with the in quadrature and direct component of currents on the two electrical subsystem's branches are completely eliminated. The dynamic matrix, thus, passes from a 10x10 of the full model to a 6x6 in the reduced one. Appendix A.6 contains all the state space matrices representing the reduced model.

5.2.1 Frequency Response

The frequency response of the reduced model, as compared to the full model discussed in the previous chapter, generally shows a high similarity. In most cases there is no significant difference between their frequency response functions. As a result, displaying the same response functions seen in the previous chapter is not be meaningful in distinguishing the behavior between the two systems. It is important to emphasize that even though the frequency responses are nearly identical, this does not necessarily imply that the reduced model faithfully represents the full model, if it did there would have been no reason to numerically treat the full model instead of this reduced one in the first place.

The difference between the two models is indeed present and, in many situations, quite noticeable. The reason it does not manifest in the frequency response functions seen in the previous chapter is that they explore the wrong excitations as they are not too much affected by the presence of a spring instead of an electrodynamic levitation cushion. The effect of the spring can be seen when changes in elongation happen, thus, a suitable excitation that can be investigated is the track irregularities' vertical displacement rather than their vertical velocity. To perform such analysis and obtain the corresponding frequency response functions $\ddot{z}_s/z_{in}$ and $\ddot{z}_{us}/z_{in}$ the state space equation must be slightly modified to encompass a displacement in the input vector effectively removing it from the states vector. The frequency response functions for the sprung and unsprung mass acceleration response to input track vertical displacement are displayed in fig 5.3 and 5.4 respectively. One may notice that there is no significant difference between the full and reduced model response at least up to 50Hz. At higher frequencies the difference is quite noticeable and a resonance frequency associated with the electrical subsystem is completely missed. Apart from that, the slope of the two FRF going towards very high frequencies is very dissimilar. This discrepancy between the two models has a very well understandable physical meaning. When the frequency of the track irregularities is quite low, the spring is able to continuously follow the track shape and the force on the sprung and unsprung mass changes in a continuous way similarly to what happens when the magnetic cushion is in the place of the spring. Moving towards higher frequency content excitations implies very high rate of changes of the spring elongation, resulting in rapid changes of force applied to the

unsprung mass. This concept can be taken to extremes thinking to a sudden step on the track surface, such perturbation is associated with a very high frequency content and so, by looking at the FRFs, the two systems should be working in a very different way. What physically happens to the reduced model with such perturbation, is a sudden change in elongation of the spring, resulting in a sudden step in lift force perceived by the unsprung mass.

In the full system, instead, there is not such direct link between the ground shape and the lift force, the generation of such force is in fact delayed and more progressive with respect to the reduced model. In the full model, the source of this delay is the inductance of the electrical subsystem related to the track that is completely neglected in the reduced model.

In fact, a sudden change in track height results in a sudden reduction in the air gap and, consequently, in a sudden increase of concatenated magnetic flux with the track electrical subsystem. Such increase in concatenated magnetic flux drives a sudden change in induced electromotive force in the track's electrical subsystem. This step in electromotive force does not instantly translate in a flowing current, as the current behavior is driven by the dynamic equation of the electrical system. The induced current is the responsible of producing a magnetic field in contrast to the one that produced it (by Lenz's law) and, thus produces a lift force. So the production of lift force in the full model is not subject to impulse behaviors but to more or less rapid continuous increases.

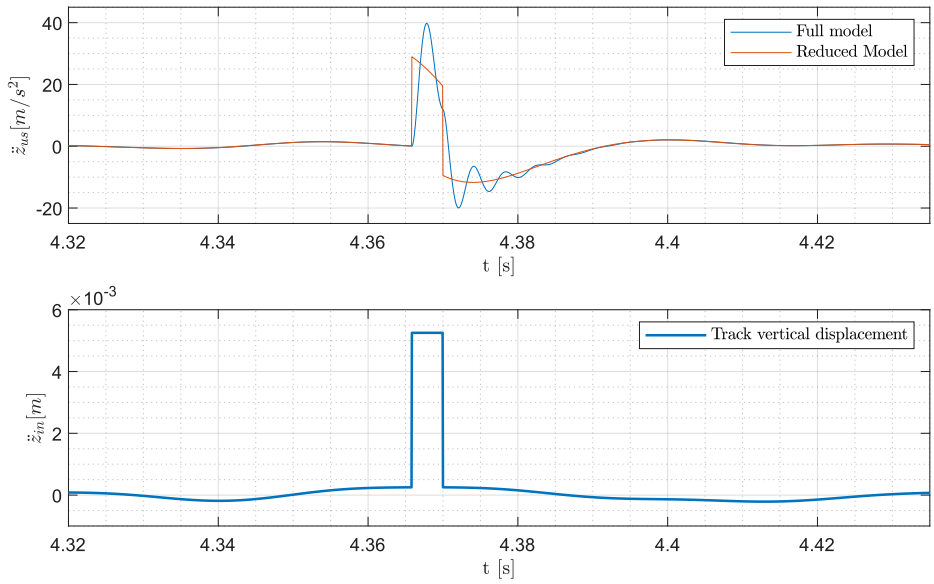

Figure 5.5: Unsprung mass acceleration reaction to a conductive 5mm step on the track

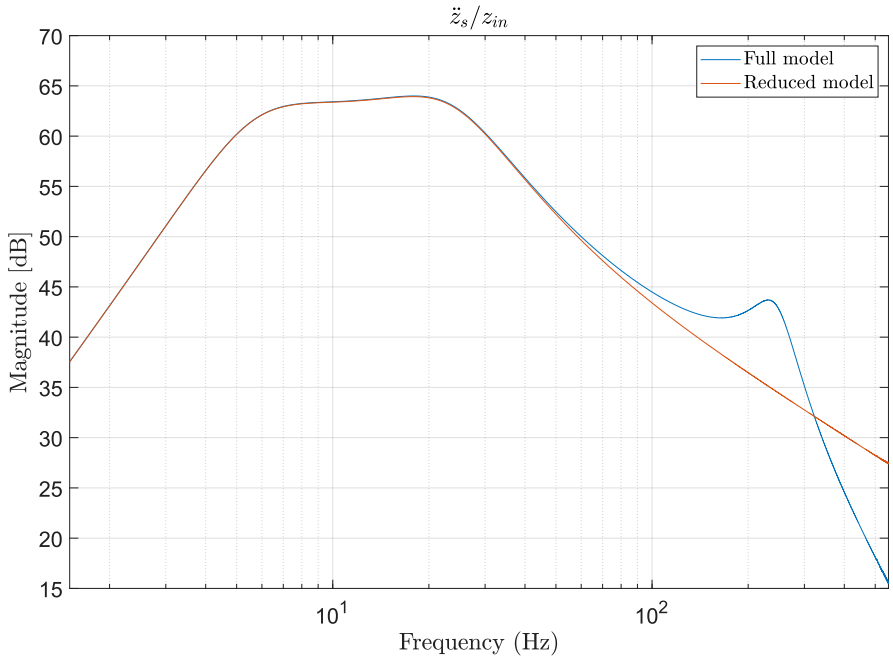

Figure 5.3: Full vs Reduced model unsprung mass acceleration FRF with input vertical track displacement

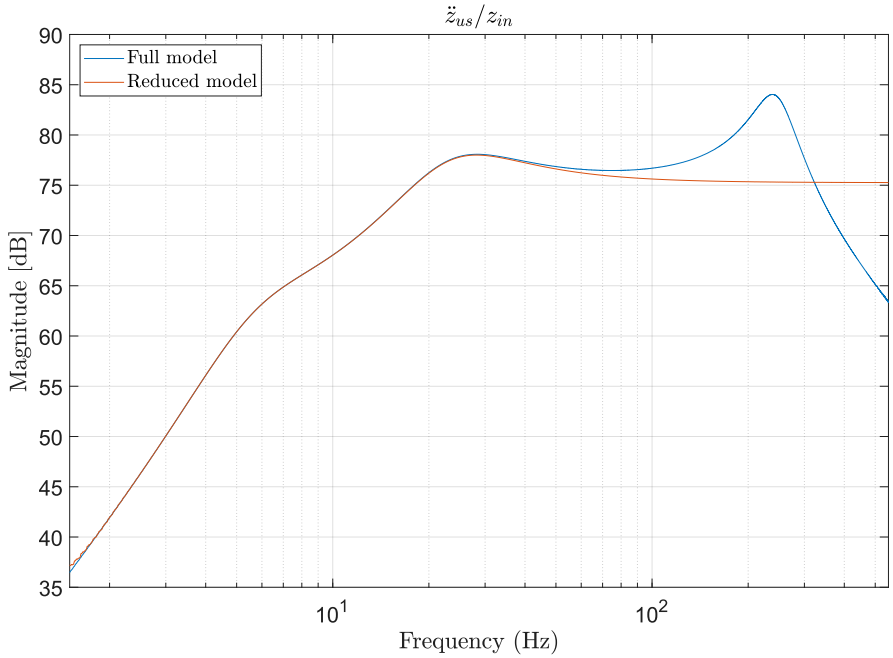

Figure 5.4: Full vs Reduced model sprung mass acceleration FRF with input vertical track displacement

Everything mentioned is confirmed by Figure 5.5 in which a sudden 5mm step is added to the shape of the track irregularities. It is noticeable how the orange curve, showing the reduced model behavior, perfectly overlaps the full model before and after the effect of the step, since the excitation comes from the sole low frequency effect of ground irregularities. The difference, as announced, is noticeable nearby the impulsive change of height of the track and it is visible that such impulse is directly reflected in in an impulsive change in unsprung mass acceleration for the reduced model and in a continuous increase of such acceleration for the full model.

5.3 Estimation

The main objective of this section is to obtain a working Kalman filter to accurately estimate the relative velocity between the sprung and unsprung masses at each time step. Before proceeding with mathematical simulation, an appropriate measurement and process noise must be introduced in order to mimic potential uncertainties that might emerge during testing. While the dynamic model has been proved representative of the real system, it remains an approximation. Discrepancies between the model and the actual system stem from oversimplified assumptions. Indeed, every mathematical model includes its own assumptions and a flawless representation is unrealistic to be obtained. Nevertheless, there are more or less significant sources of error. Among the most impacting factors are the linearization of the lift force equation and the modeling of the track through a two-branched electrical subsystem. In addition, representing the voice coil as a simple RL circuit, introduces notable sources of error. Such errors must be taken into account when simulating the system in Simulink and they are considered by adding a white noise to each of the states in the state space subsystem. Figure 5.6 depicts the Simulink block diagram used for the estimation of states. The modified full model taking into account the input displacement and velocity was utilized. As visible, the inputs to the system is the ground irregularities' profile, its derivative, the forces on the unsprung and sprung masses and the voice coil voltage.

The Kalman filter block requires two inputs, the first one is the input vector to be fed to its model and the second one is the vector of measurements that must coincide with the mathematical model output vector y. Notably, the Kalman filter cannot be aware of any sudden changes in input forces neither in track profile. Even though the track irregularities' form is known, feeding their shape into the Kalman filter would be wrong since the "zero" of the track's rotation and the "zero" of the track irregularities are not guaranteed to correspond, thus the real track irregularities by which the system is being affected, and the track irregularities fed to the Kalman filter, would present a more or less pronounced shift in phase. The best course is to provide as input to the Kalman filter only those well known

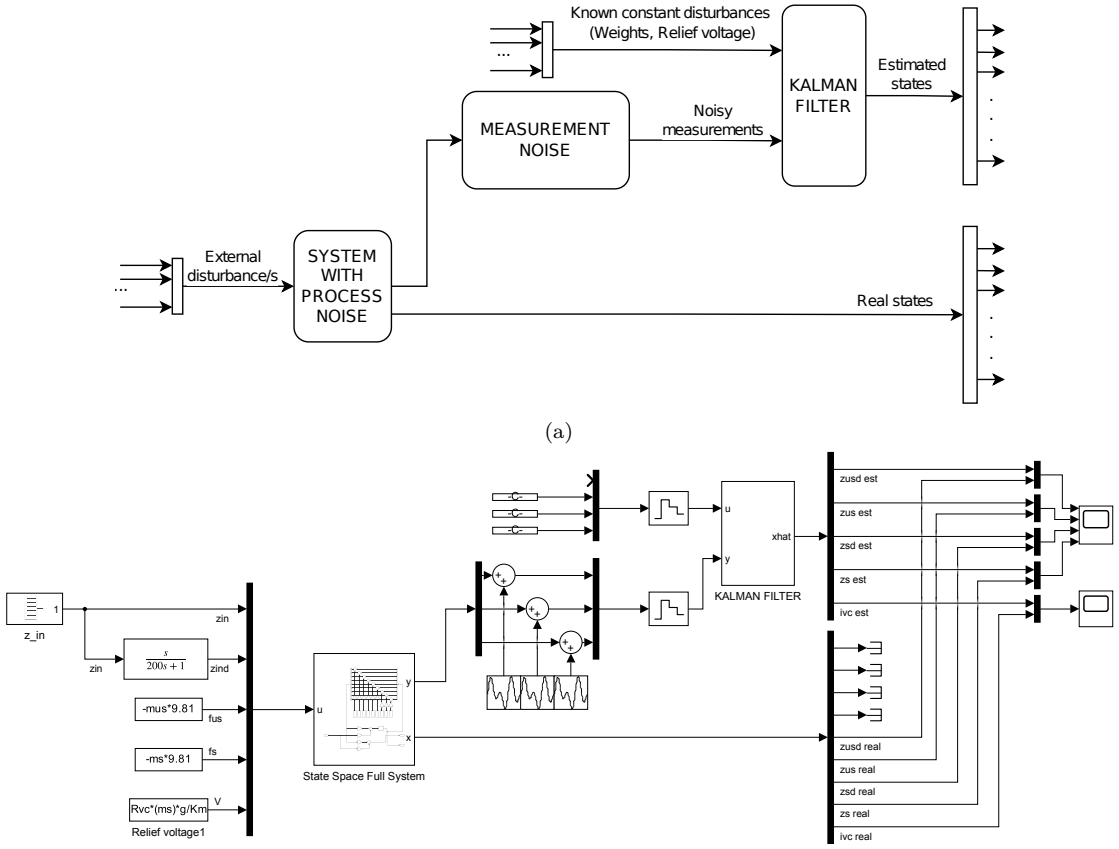

Figure 5.6: (a) Schematic representation (b) Simulink implementation

constant inputs, thus the unsprung and sprung mass weight force and the voice coil relief voltage. The system in the state space block is actually simulating the behavior of the real system as it encompasses also the process noise. Its output vector y contains all the variables to be measured and then input into the Kalman filter. Before doing so, a Gaussian measurement noise is added to each component of the y vector. The two zero-hold blocks before the Kalman filter block convert the continuous signal into a discrete signal having the sample frequency of the data acquisition (DAQ) board in use in the experimental setup.

In Figure 5.7, the impact of introducing a process noise is illustrated both for the sprung and unsprung mass.

This discrepancy between noisy and regular acceleration captures the mismatches between the mathematical model in use and the actual system. It's important to evidence that the process noise that was added to this analysis is fictitious. Its purpose is to deliberately create a divergence between the model's behavior and the real system. Thus, the noisy signal does not represent the behavior of the

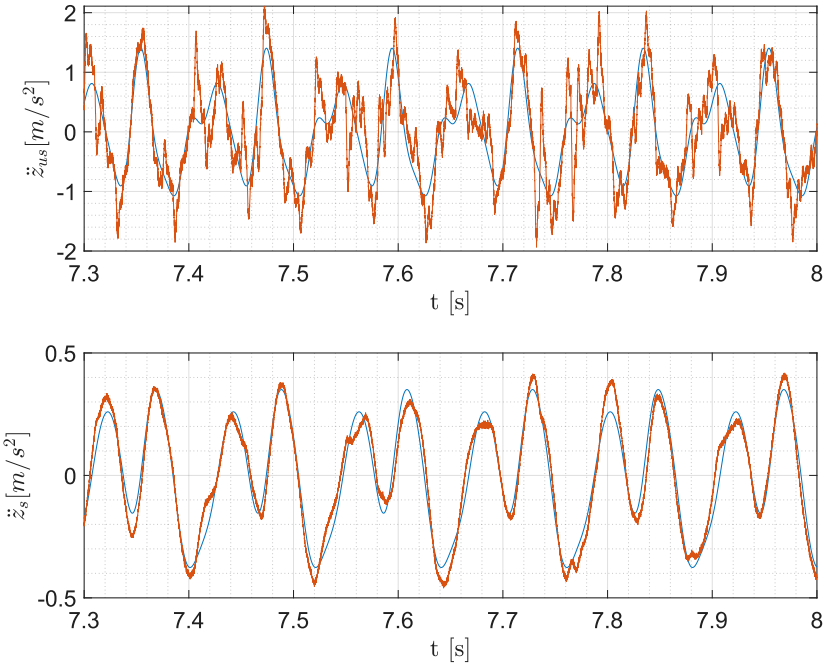

Figure 5.7: Unsprung (top) and sprung (bottom) mass acceleration,(Full) mathematical model's response (blue) and (Full) mathematical model with process noise (orange) at 500 rpm, with input track irregularities

actual system, it serves, rather, as a tool used to assess the Kalman filter's ability to predict the behavior of the system even when it deviates from the model. Figure 5.8 displays the sprung-unsprung mass relative speed, which is the signal to be estimated. A working Kalman filter should reproduce a signal similar to the orange one. If it does, it means that the filter is effectively averaging information coming from sensors with those of the mathematical model. The tuning of the Kalman filter is based on adjusting the parameters Q and R, related to the process noise and measurement noise covariance respectively. Increasing the first parameter allows the Kalman filter to admit greater deviations of the states from the model, but it makes it more sensitive to noisy measurements. Using a low Q instead, limits the deviation that the actual system can have with respect to the model, thus low Q could be suitable if the model is considered highly reliable. Regarding R instead, an high value implies noisier measurement that cannot be deeply relied on, so the Kalman filter estimation will more closely resemble the model's behavior over the measured one. Using a low R parameter implies low noisiness of the measured parameters so the filter's estimation will be more influenced by measurements and less by the model. Talking about measurement noise, Figure 5.8 depicts the three

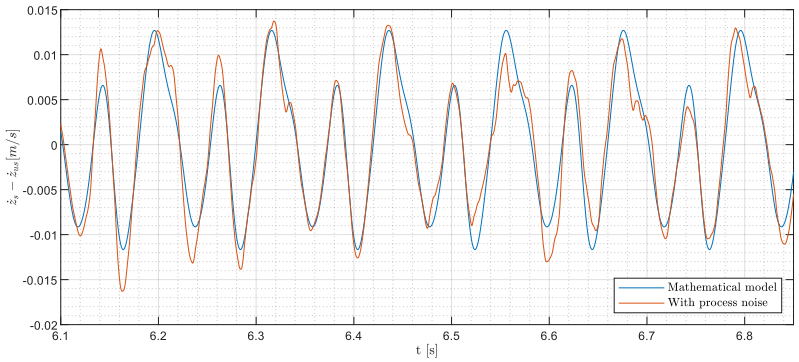

Figure 5.8: Relative velocity of the (Full) mathematical model (blue) and of the (Full) Mathematical model with process noise (orange)

measured variables with their measurement noise. The noise follows a Gaussian distribution with non zero mean value to allow from some constant deviation from the actual behavior. Finally, Figure 5.10 depicts the estimated relative speed

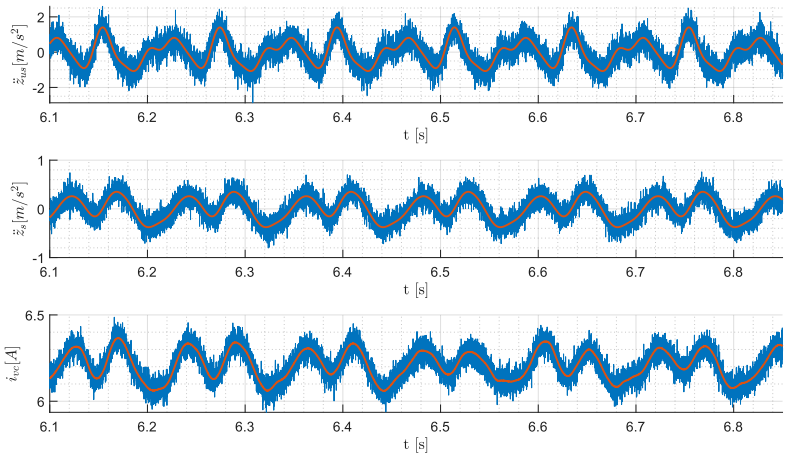

Figure 5.9: Model with process noise (orange) and Measurements (blue). From top to bottom: measured unsprung mass acceleration, measured sprung mass acceleration, measured voice coil current

together with the speed coming from the mathematical model plus process noise and the relative speed predicted by the sole mathematical model.

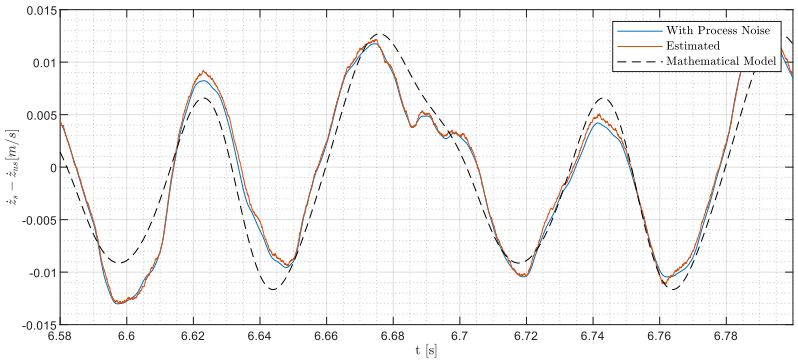

Figure 5.10: Relative speed of: (Full) Mathematical model with process noise (blue), (Full) Mathematical model (black dashed) and estimated by a Kalman filter working with reduced model (orange) with R=25 and Q = 10^{-5}

5.3.1 Input Step

The previous state estimations were obtained by considering the sole effect of ground irregularities as disturbances. Despite not being aware about the shape of such irregularities, the Kalman filter successfully captured their influence on the system's response. However, it's worth to note that track irregularities bring in a relatively small disturbance and also a continuous one. Therefore it would be interesting to evaluate the effects of introducing a sudden step in the track profile, in particular the same step used when comparing the full and reduced model in figure 5.5. As mentioned earlier this kind of disturbance is the most critical one regarding the accuracy of the reduced model (which is the one implemented into the Kalman filter). Forgetting for a moment the introduction of fictitious process noise, the difference between the reduced and the full model can itself be regarded as process noise. The results of the estimation are displayed in figure 5.11. Remarkably, even though the filter bases its prediction on the reduced model, the contribution of the measurement allows the final estimation to capture dynamics that do not belong to the reduced model. These results were obtained using the same parameters, R and Q, as in the estimation involving track irregularities ($Q = 10^{-5}$ and $R = 25$). Now, reintroducing the fictitious process noise, Figure 5.12 displays the quality of the estimation of relative velocity.

Remark that employing a very low process noise covariance factor (Q) does not result in the estimation aligning with the behavior of the reduced model. In fact, as Q tends to zero, the estimation of $\ddot{z}_{us}$ tends toward a null signal. This occurs because the system in the Kalman filter is not receiving any inputs and a null Q is equivalent to considering the mathematical model (together with its inputs) in the filter entirely accurate. Consequently, the measurements are not considered.

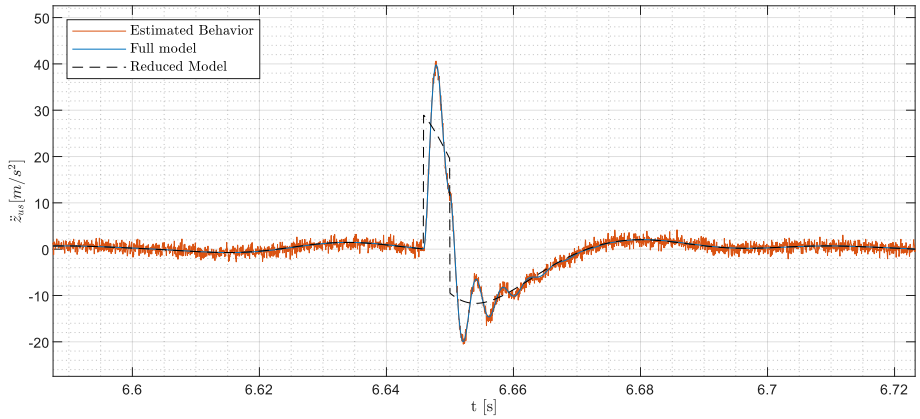

Figure 5.11: Input slab response of the reduced and full models together with the Kalman filter estimated response.

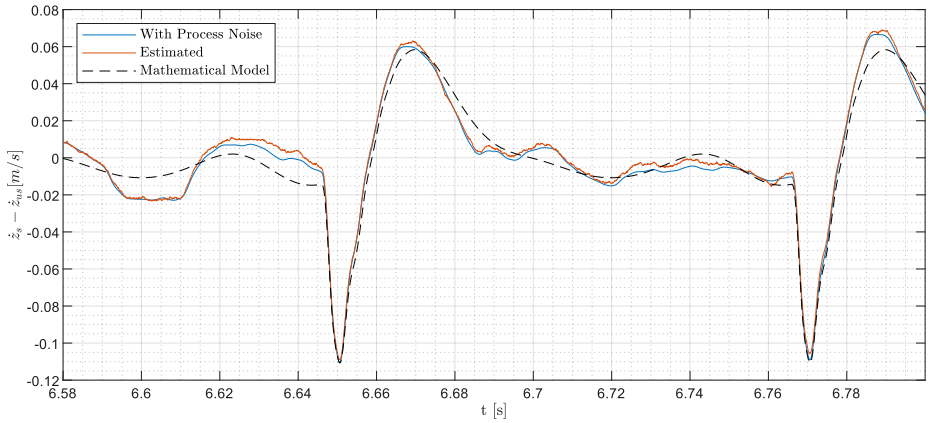

Figure 5.12: (Full) Mathematical model with process noise (blue), (Full) Mathematical model (black dashed) and estimated by a Kalman filter working with reduced model (orange) with R=25 and Q = 10^{-5}

Chapter 6

Control

Up to this point, this thesis work has primarily dealt with understanding the system's properties. A thorough exploration of the dynamic characteristics of the model was presented in Chapter 4. Within such chapter, a form of proportional control for the electro-dynamic levitation measuring device was introduced and it incorporated a static gain that mimicked the effects that an additional damper could bring into the system. Such approach was not directed towards enhancing passenger comfort; its primary objective was, in fact, to establish some sort of simple enough control loop that could be readily implemented into the real test bench to evaluate the feasibility of retro-acting the system. Furthermore, such implementation on test bench could pave the way to experimentally confirm the effects of damping on the system's dynamics and to further prove the correctness of the mathematical model. In this chapter, the main focus is enhancing passenger comfort within the train carriage. To this purpose, the system's loop will be closed once again, but this time in a significantly different fashion than previously. The estimation of states, investigated in Chapter 5 will pay a central role in the control process, providing more live information about the system behavior and makes it possible for a better identification of the correct control action to be exerted. It must be underlined that this part of the work not only aims to provide a working control strategy for this specific system but also wants to present a novel approach to control strategies based on fuzzy logic, also setting the base for possible future research. The content of this chapter will first bring an overview to standard fuzzy inference system working principles and then present the novel proposed approach showing the steps and trials that have led to the final results.

6.1 Introduction to fuzzy logic

Fuzzy logic exploits a totally different approach of classifying information compared to classical logic. In classical logic, commonly known as "crisp" logic, a proposition can only satisfy or not a certain condition. If for example one was to state that a number is greater than zero, crisp logic would assign a value of truth of "1" to every number that satisfies the condition. A value of "0" is instead attributed to every number that does not satisfy it. The truth diagram of such logic could be represented as a step signal centered at zero. In this way, first of all, it is trivial that no distinction is being made between a very large number and a very small number, the information is very hermetic and does not allow seeing how close the number is to not satisfy the condition. Perhaps most importantly, the transition of the degree truth from 0 to 1 occurs abruptly, without a transition. Fuzzy logic overcomes these issues with data interpretation and allows for an improved classification of inputs. An input signal can partially satisfy a condition in a way specified by the definition of a fuzzy set composed by the so-called "membership functions". A membership function describes the level of truth of a certain class within the range of variation of an input. To better understand this concept it is useful to provide an easy example. Figure 6.1 contains a depiction of how the degree of truth functions (membership functions) appear for a crisp logic and a fuzzy logic.

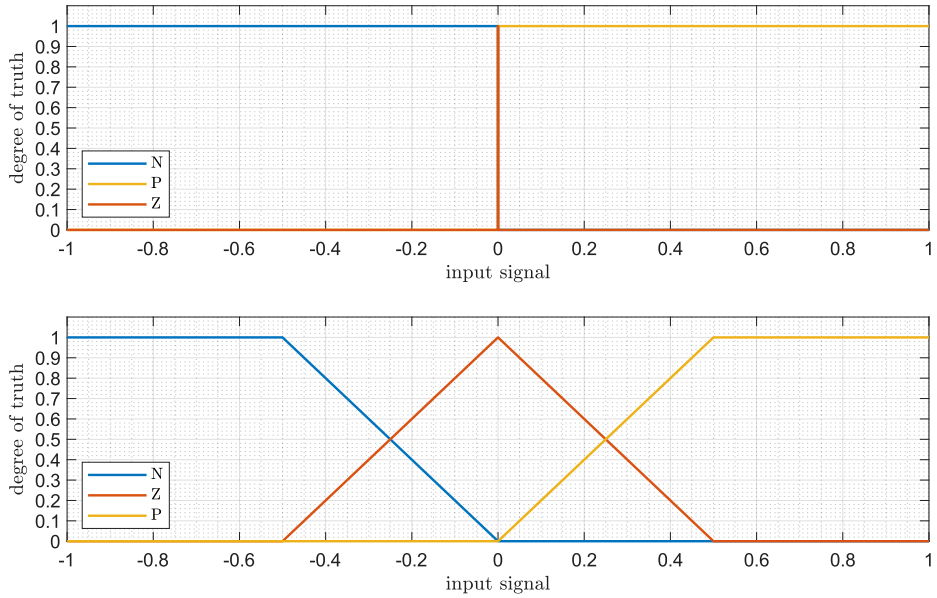

Figure 6.1: Crisp logic classes (top) and Fuzzy logic Membership Functions (bottom)

The signal range in this example is between -1 and 1. Three classes have been identified, N for negative numbers, Z for zero and P for positive numbers. In crisp logic, each function assumes only 1 or 0 value, in particular, the Z membership function assumes unitary value only when the input signal is exactly zero. In fuzzy logic, the degree of truth of each one of the classes transitions continuously from zero to one, not allowing for steps. As visible, going from -0.5 to 0, the N degree of truth decreases while the Z degree of truth increases accordingly. For example, in logical terms, the input -0.25 is seen by crisp logic as 100% negative number, while, in fuzzy logic it is seen as a 50% negative and 50% zero. The number 0.15 is seen as 100% positive in crisp logic while it is identified 70% zero and only 30% positive with the defined membership functions in fuzzy logic, as it is small enough to be accurately represented by the zero class. A fuzzy controller, like any type of controller, receives information about the states of the system and schedules an appropriate action on the control variables that depends on the logic laying behind. Such logic will turn out to be heavily depending on the designer's choices. To turn input into appropriate output, information should follow an appropriate path within the fuzzy controller. One can distinguish three main steps:

- Fuzzification
- Inference
- Defuzzification

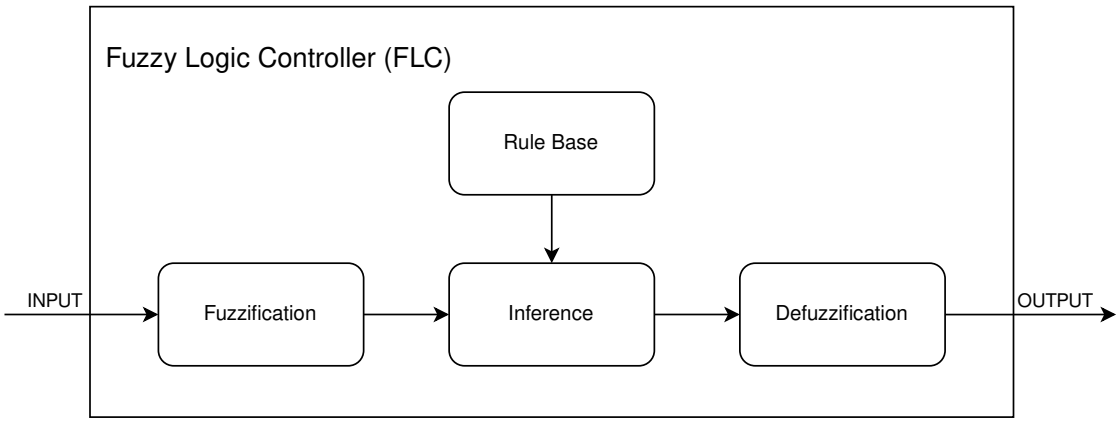

Figure 6.2: Fuzzy Logic Controller (FLC) scheme

Figure 6.3 contains a visual representation of how input signals are interpreted in fuzzy logic and in crisp logic. The main interest for fuzzification is that of categorizing data in classes and to build a table of rules containing an entry corresponding to all possible combinations of inputs. This table of rules is represented by the

grid displayed in the figure and the activated rules are highlighted in black/gray. As noticeable, crisp logic classification finds one and only one activated class for each input, thus, the activated cell is uniquely determined. The passage of the activation from one cell to another happens drastically in an on/off fashion. When fuzzy logic is applied instead, each input activates a certain number of classes; thus the activation of rules can be seen to form a cloud centered on the crisp logic activated rule. The result of such distribution of the degree of truth is that the transition from one rule to another is progressive and does not produce impulsive variations of the control signal which would be mischievous for the final objective of stabilizing the system.

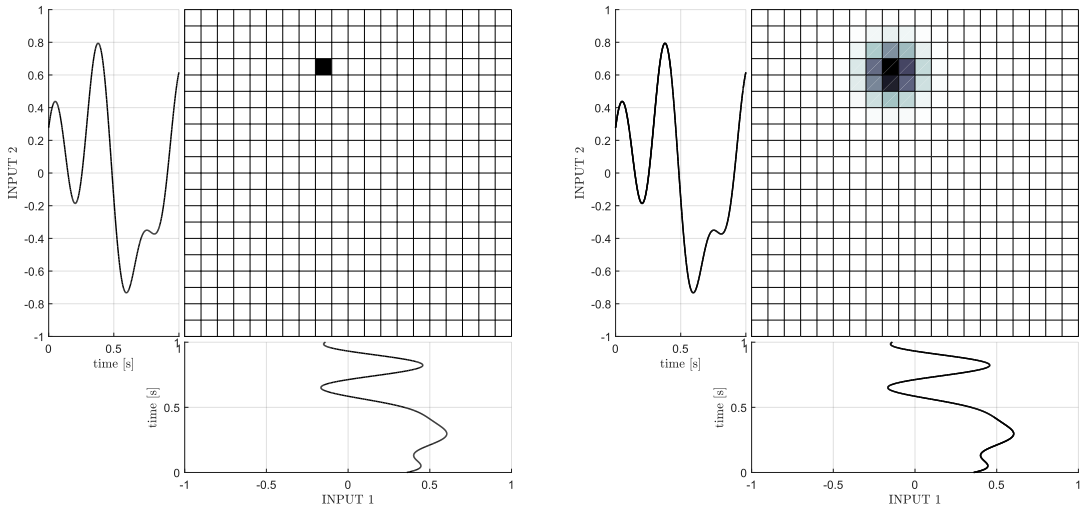

(a) (b)

Figure 6.3: (a) Crisp logic activated rule (b) Fuzzy logic cloud

Note that the fuzzy appearance of the activation cloud gives the name to this kind of logic. Defining the parameters characterizing a fuzzy inference system consists in giving a description on the characteristics of such cloud, thus, determining the extent of the influence of neighboring rules on the final control action. In the following paragraphs a step-by-step introduction is provided on a very simple 3x3 table of rules.

6.1.1 Fuzzification

The process previously described for the dummy fuzzy set with N, Z and P membership functions reflects the fuzzification passage. This step consists in converting the input signal into as many degrees of truth as membership functions

in the fuzzy set. If one denotes with μ_i the degree of truth of the membership function i, and if one refers to the fuzzy set in Figure 6.1, the result of the fuzzification of a dummy input of 0.15 should result in the following information.

$$\mu_N = 0 \quad \mu_Z = 0.7 \quad \mu_P = 0.3 \tag{6.1}$$

The activation of the membership functions informs the fuzzy controller that the input signal is positive but quite small, the controller will respond accordingly in the next phase

6.1.2 Inference

The inference section is the central part of a fuzzy controller, where the actual control action is decided and the performance of the controller is determined. In this paragraph, the inference following the Mamdani method is discussed, as it is the only one that will be adopted. More insights on other inference methods are reported in [15]. At the early stage of controller implementation the designer should first define a suitable fuzzy set for the output of the controller. After designing input and output fuzzy sets, a set of rules must be defined based on the knowledge of what input is being fed to the controller and what output the controller is providing to the system. The fuzzy rules to be defined in this part are as many as the combinations of membership functions for each input. Based on the combination and on the degree of truth μ of the activated membership functions the designer must decide what rule to apply. Again making an example is the best path to understand this phase. Let's imagine that the fuzzy set in Figure 6.1 can interpret the two inputs of a new fuzzy controller. There are three membership functions for each input and thus 9 possible combinations of activated membership functions. There are then 9 rules to be defined. One can design a possible output fuzzy set with a larger number of membership functions to increase the freedom to choose the correct rule to fire for each of the 9 cases. Figure 6.4 shows a possible output fuzzy set made of 5 membership functions NB (Negative Big), N (Negative), Z (Zero), P (Positive) and PB (Positive Big).

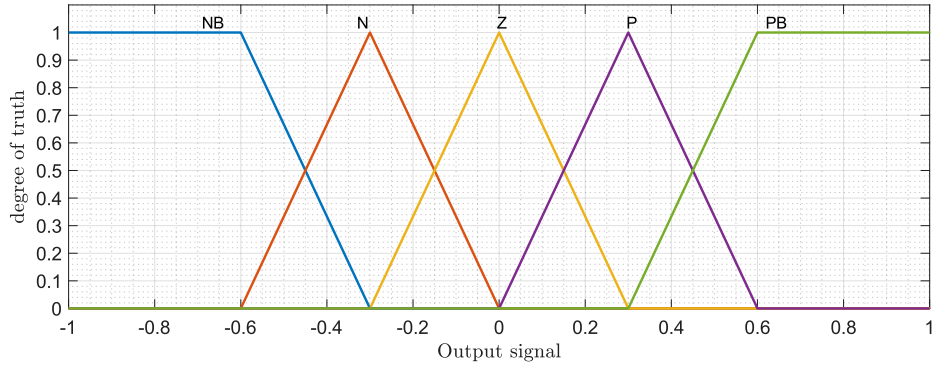

Figure 6.4: Example of output fuzzy set

Consequently, one can write an appropriate set of rules based on the physical knowledge of the system and the expected reaction to a given control signal. Table 6.1 contains a possible set of rules for the given system. At this introductory stage, these are just random rules, in the study of the implementation for the dynamic measuring device, the rules will be focused on reducing the sprung mass acceleration by acting on the voice coil voltage. If for example one let input 1 be 0.15 and input 2 be -0.25 the degrees of truth for each input are the following

$$\mu_{N,1} = 0 \quad \mu_{Z,1} = 0.7 \quad \mu_{P,1} = 0.3$$

$$\mu_{N,2} = 0.5 \quad \mu_{Z,2} = 0.5 \quad \mu_{P,2} = 0$$

Input 2 → Input 1 ↓	N	Z	P
N	PB	P	Z
Z	P	Z	N
P	Z	N	NB

Table 6.1: Table of Rules

This means that 4 classes in the bottom left of Table 6.1 are activated in the inference phase for the specified input. Referring to Table 6.2, notice how the degree of truth assigned to each rule is the minimum between the degrees of truth of the input membership functions related to such rules. This is because the assigned degree of truth to a rule is the result of the intersection between the input activated membership functions which can be demonstrated to be the minimum between the involved degrees of truth [15]. When the same class of the output fuzzy set is activated two times such as the Z membership function in Table 6.2, the highest

activation value should be considered since it is the result of the union of the two membership functions [15], in this case output membership function Z is activated with 0.5 degree of truth.

Input 2 → Input 1 ↓	N (0.5)	Z (0.5)	P
N	PB	P	Z
Z (0.7)	**P (0.5)**	**Z (0.5)**	N
P (0.3)	**Z (0.3)**	**N (0.3)**	NB

Table 6.2: Inference

The resulting degrees of truth of the output fuzzy set are the following.

$$\mu_{NB,output} = 0 \quad \mu_{N,output} = 0.3 \quad \mu_{Z,output} = 0.5 \quad \mu_{P,output} = 0.5 \quad \mu_{PB,output} = 0$$

6.1.3 Defuzzification

The inference stage has produced a certain array of activation values for the output fuzzy set membership functions. Therefore, it has converted a fuzzy input (originated by fuzzifying the crisp real input) into a fuzzy output that has to be brought back to crisp logic. There are several ways to perform the conversion into crisp logic but, in this work, the centroid method will be used in order to follow the Mamdani approach. This defuzzification approach, also called α-cut method consists into cutting each membership function at the height of the degree of truth assigned in the inference stage. Figure 6.6 shows such procedure applied to the previous example.

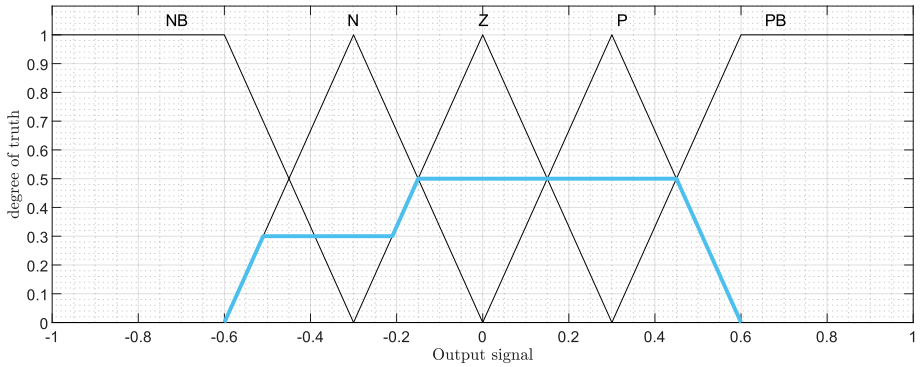

Figure 6.5: α-cut of the output set for defuzzification

Having obtained the α-cut trapezoid-like shape, the centroid approach consists in determining the center of gravity of such region and in using the corresponding x

coordinate as output value. It is fairly easy to compute such value u as the average of all the x coordinates weighted with the corresponding value of the α-cut shape following equation 6.2

$$u = \frac{\int u \cdot \mu(u) du}{\int \mu(u) du} \tag{6.2}$$

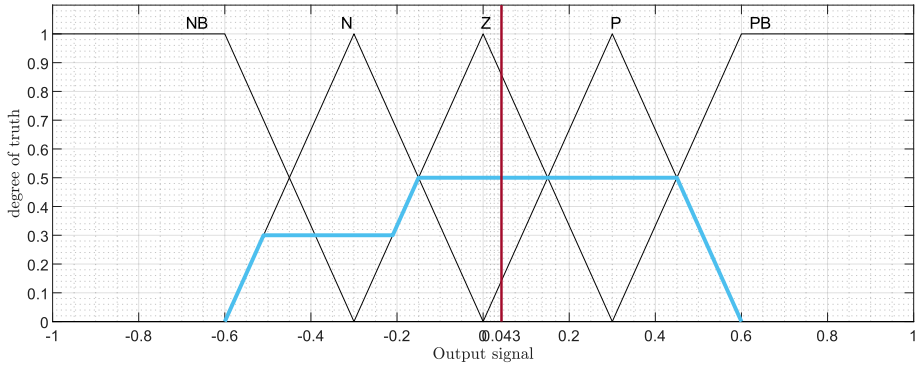

Figure 6.6: Defuzzificatoin through centroid method

In this example, the defuzzified output will be 0.043 and, as expected, it is quite close to zero since it had activated both negative and positive output membership functions. A simpler but worse approach is that of the method of maxima which can come in three variants: FOM (First of Maximum) chooses the first maximum value going from left to right as the output, in this case it would output -0.15; LOM (Last of Maximum) chooses the last of all maximum points, in this case outputs 0.45; The MOM (Middle Of Maximum) that instead outputs the average between the two, thus 0.15. There are other approaches such as Sugeno method that allow to pass directly to crisp signals after the inference phase, without the need for the defuzzification stage but producing somehow rougher outputs. The centroid method is mostly used since it provides as output an averaged value that is less sensitive to variations in the input value and produces an overall smoother response.

6.2 Fuzzy logic control proposed approach

The previous section contains a very brief explanation of how fuzzy logic approach is applied using the Mamdani method. Some comments must be made before introducing a possibility of improving the conventional approach. In the example, two very simple fuzzy sets were considered for the inputs, consisting of 6 total membership functions, while an increased number of classes had to be used for

the output fuzzy set given that 9 possible combinations of the input membership functions may occur. This definition of fuzzy set was useful to render the idea but may be too simplistic to work with in a real fuzzy controller. Anyway, keeping a low enough number of membership functions is almost mandatory given that the growth of the number of rules is exponential with the number of classes, when more than one input is used. Moreover, choosing the distribution of membership functions is very dependent on the designer's choices and, effects of changes in fuzzy sets, are not easy to identify and manage. Therefore, maintaining a low number of membership functions plays also the role of keeping a low number of arbitrary parameters that depend on the designer. The same may be said for the shape of these functions. As mentioned earlier, from literature, one can see a variety of functions that range from simple triangular ones to more complex sigmoid or pi shapes requiring a larger number of arbitrary values. In the pursuit of producing the least user dependent fuzzy sets it is undeniably useful to use triangular and trapezoidal membership functions.

Interpretation of the response of a fuzzy controller is not easy and requires many trial and error iterations. However, the main course that one can take towards optimization always tends to privilege trying different combination of rules rather than going to modify the fuzzy sets. Small changes in position of membership functions are already very difficult to manage and it is anyway never easy to determine what modifications to make since they usually produce marginal effects and they have to be made almost randomly. Furthermore, finding the optimal fuzzy set involves an optimization that spans over tens of parameters. If fuzzy sets configurations are hard to optimize, optimizing the shape of each function is basically unthinkable. For all of these reasons the procedure will stick with an "accepted" fuzzy set to be used for all inputs and considers it as the optimized one. No optimization is performed on its definition. In the following sections, the choice of adopting triangular membership functions for fuzzy sets will be further justified, since post processing on the control surfaces will produce smoothing effects that can bring similar advantages to using different shapes.

Conventional fuzzy controllers found in literature [16] [17] do usually refer to many arbitrary parameters but, maybe most importantly, the common approach is to identify a possible range of variation expected for the inputs and define the fuzzy set membership functions for that range or, at most, statically normalize the inputs to a normalized -1 to 1 range using a static gain based on the estimated range. Though this may produce positive effects on the system's response, such approach shows various critical points. A so designed system is very dependent on the choice of the range of variation of the inputs. If for some reason the system is shaken by random unexpected excitation that makes the inputs very large, the controller wouldn't be able to react accordingly. Thus, imposing a range and expecting it to be always respected for the whole life cycle of the machine could be a dangerous

choice. One could think of overcoming this problem by overestimating the range of variation of the inputs in order to design the controller to be responsive also to very high amplitudes. Also this approach is not recommended. Defining a large range can mean either one of the following two alternatives

1. Defining more membership functions to maintain the same resolution in the whole input range, thus increasing exponentially the size of the inference system;

2. Stretching the same number of membership functions over a broader range, introducing a lower-resolution fuzzy controller with a likely worse performance.

Therefore, anyone of the two options, leads to big compromises. In the first case one must define a much more complex controller with many membership functions that are almost never activated if not for failures or, in general, unexpected inputs. In the second case, one is worsening the performance over the most useful range in order to stretch the fuzzy sets to a broader domain that, again, is needed only in extreme situations. Of course one could define a less precise set of membership functions in those regions that tend to be almost never covered or, could support the fuzzy controller with another one of different type that takes the lead when unexpected regimes are detected. The proposed solution to this issue allows for the use of a stand alone adaptive fuzzy controller that does not need auxiliary controllers.

The idea is that of working with a "normalizer" that is able to re-scale in real time the control space to adapt to the magnitude of the phenomenon it is receiving as input. An example is illustrated in Figure 6.7. The original signal has various regimes in time, the objective is to extract a real time gain that divides the original wave to obtain a normalized signal. In this way the control will only take into account the shape of the signal and the control signal will also be output in a normalized way. The entity of the output will be again scaled respecting the same scaling signal used for the inputs. The full approach logic is shown in Figure 6.8. In the Figure, the system is excited by external disturbances and produces a certain response signal. The normalizer captures the response splitting its information in the normalized signals that contains information about the shape of the response and a Dynamic gain that carries information related to the magnitude. The normalized wave enters the normalized space fuzzy controller that consequently outputs a control signal in a -1 to 1 range. The control signal must be rescaled to take into account of the previous scaling performed in the normalizer block, thus, it has to be multiplied by the dynamic gain to produce an adequate magnitude of the control signal. Notice that if the normalized space controller works with

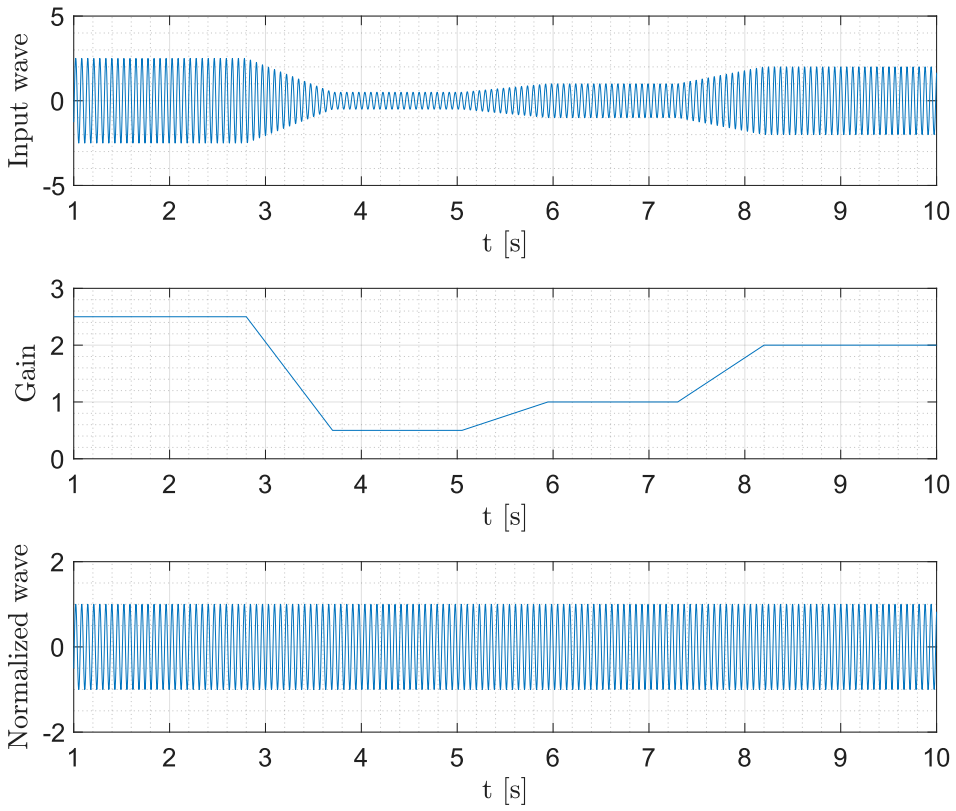

Figure 6.7: Normalizer working principle. From top to bottom: 1. Input signal with varying amplitude 2. Dynamic gain 3. Normalized signal

n inputs, the normalized response and the dynamic gain are multi-dimensional signals of size n. In this case, thus, only one gain must privileged out of the n and it usually is the one related to the most relevant state to be controlled.

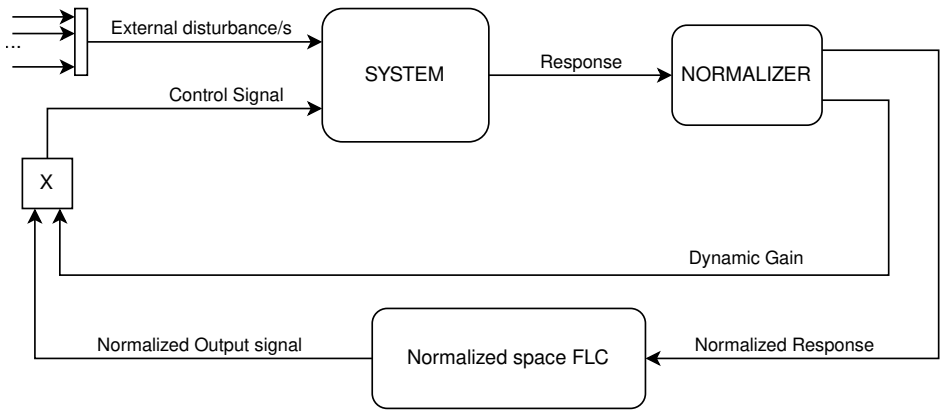

Figure 6.8: Normalized space FLC implementation concept

6.3 Normalizer

In the schematic shown in Figure 6.8, the two pivotal elements for the approach are the normalized space Fuzzy Logic Controller (FLC) and the Normalizer block. In this section, an explanation is provided on how the normalizer was implemented, exploring the opportunities for optimization and thoroughly examining the impact exerted by its primary parameters. The discussion about the normalizer working principle will be articulated in two parts. At first an alpha version of the normalizer logic is presented, then an optimized beta configuration is shown. A very big improvement in control performance was witnessed when passing from the initial to the optimized normalizing logic.

6.3.1 Logic

Regardless, before delving with the actual implementation in SIMULINK®, it is useful to explain through a flow chart, displayed in Figure 6.9, the logic that was followed. It is also useful to refer to Figure 6.13 that provides a visual representation of the dynamic gain in time. First of all, the approach relies on the use of two Memory blocks, referred to as MB1 and MB2 that are able to store the value of the gain in the previous time steps. The initialization value for both memory blocks is set to 0. The normalizer is able to identify a growth on wave amplitude by simply computing the maximum value between the absolute value of the wave at a certain time step and the gain stored in MB1 in the previous time step. The maximum value will be stored itself in MB1 and act as a starting point for the next time step. The initialization value can be either zero or any negative number as it will be substituted already at the first time step. The MB1 block is updated every time a growth in input signal maximum absolute value is detected. However, this approach fails in detecting reductions in the input wave amplitude, that's why an update phase is needed in order to allow a novel computation of the gain to start from the initialization value. Therefore, one can determine a certain time-span after which the gain must be recomputed from zero and updated to allow for detection of reductions in wave amplitude. To do so the same algorithm used to determine the gain in MB1 is used, and, starting from an initialization value (0 or any dummy negative number) the normalizer must again compute the maximum of the wave for a certain period of time. This stage is undertaken in the flow chart when the "start update phase" condition is set to true. In such case, the system stores the last gain that was stored in MB1 into MB2. This reassignment is crucial for the working of the normalizer, in fact, in the meanwhile that MB1 starts again from an initialization value, and during all the estimation period, the normalizer can anyway provide the last used gain now stored in MB2 as a meaningful substitute output. This stage can be evidenced in the flow chart as the branch corresponding

to a false state of the "Update time ended" conditional block. The output block "Output gain MB2" suggests that during all the duration of the MB1 update, the output gain is the one contained in MB2 instead of that in MB1. The substitute gain MB2 is the last recorded MB1 value before the beginning of the update stage. Only when the update time has elapsed the loop is closed and the newly estimated gain MB1 becomes again the output. The cycle can recommence at the next time step starting from the new value stored in MB1 instead than the initialization value.

6.3.2 Simulink implementation

The approach presented in a flow chart form is implemented in SIMULINK®and is reported in Figure 6.11. The various stages of the normalizer functioning are controlled by two command signals y and z. These two signals have just the task of activating switches to redirect the main computation to different parts of the block diagrams. In particular, y signal is the *Begin update signal* an impulse like rectangular wave that is tasked of resetting an initialization value into MB1 (zero or any negative dummy value, in this case -1000). The z signal can be called *Update period signal* and it is another rectangular wave that starts with y but lasts for the whole length of the update stage. The two signals are displayed in Figure 6.10. The duration of the update stage as well as the update period is entirely designer dependent and must be decided according to the desired responsiveness of the normalization.

Moving back to the Simulink block diagram in Figure 6.11, one can see that the input wave is sent into a "max" block together with its negative and with the value stored in MB1, in this way the "max" block can determine the maximum value between the absolute value of the input wave and the value stored in the memory block in the preceding time step. If the wave amplitude increases with respect to previous values, it passes into the memory block and is stored into MB1 for comparison in the next time step. If the input wave was to decrease in magnitude, the gain in MB1 would stay the same up to the action of the y signal on Switch A. As mentioned, the "begin update" y signal latches a negative dummy value into MB1 in order to start a novel estimation of the amplitude.

Applying the dummy MB1 gain to the wave would produce unsatisfactory results, thus, together with the reset of MB1, its last meaningful stored value is inherited by MB2 thanks to the activation of Switch B commanded by the "Update period" signal z. Switch C remains in the update configuration until the update phase has ended and MB2 effectively replaces MB1 for the time it takes to this latter have a truthful estimation of the actual gain. MB2 remains static for the whole duration of the update stage.

Switch B is activated together with switch C by the "Update period" signal z and

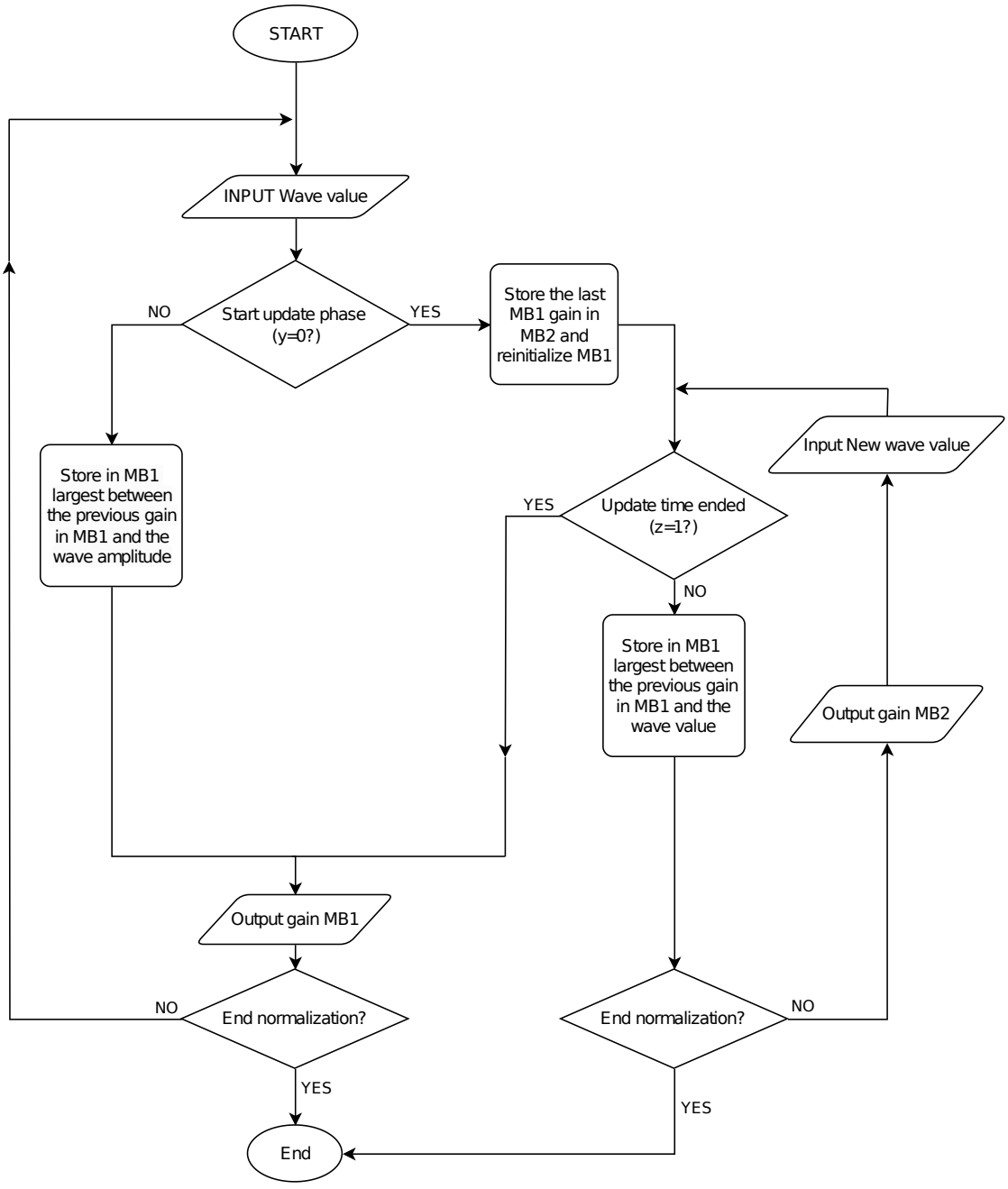

Figure 6.9: Normalizer logic flow chart

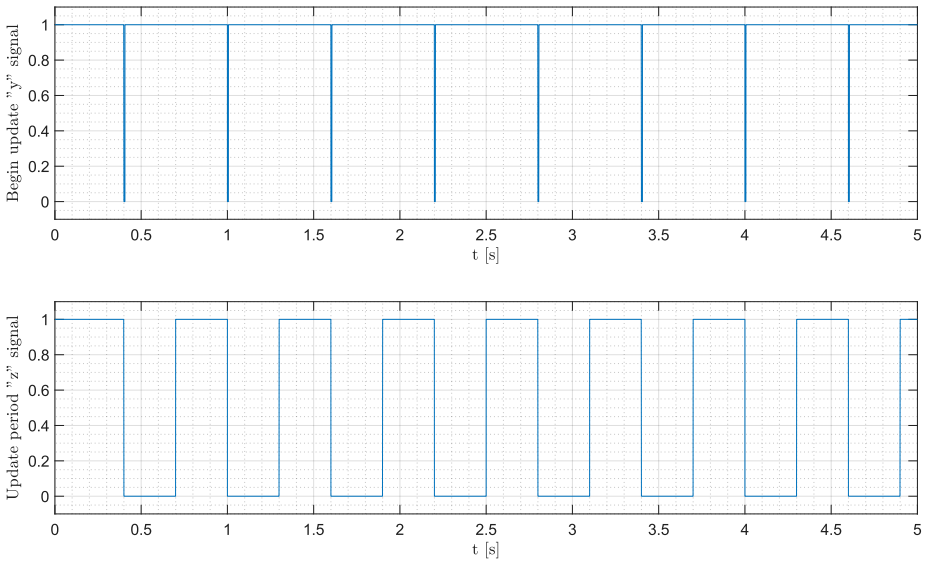

Figure 6.10: Begin update "y" (top) and Update period "z" (bottom) signals

it basically commutes the gain that must be sent to divide the wave. Therefore, in non-update configuration, Switch B is positioned to make the gain coming from MB1 to pass to the wave division. Instead, in update configuration, Switch B allows for the substitute gain coming from MB2 to pass to the division operation.

Results

The proposed design provides satisfactory results, as shown in Figure 6.12. The same wave proposed in the introduction of the logic, in Figure 6.7 is fed to the normalizer block and the estimated gain is coherent with the actual one. Notice that the increase in amplitude is followed almost perfectly while the reduction shows more steps since, in this case, the update of the gain can happen only at the end of the update time.

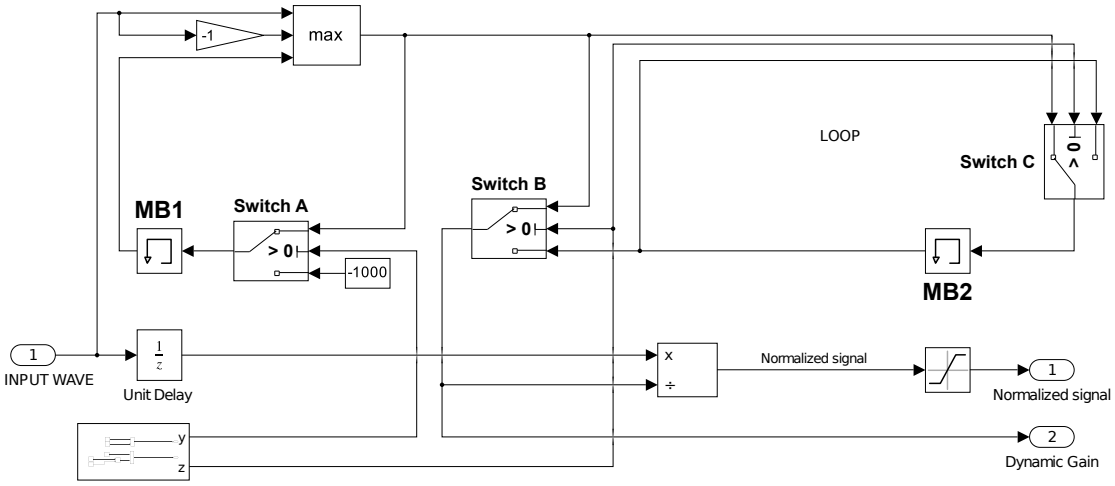

Figure 6.11: Normalizer implemented in SIMULINK®

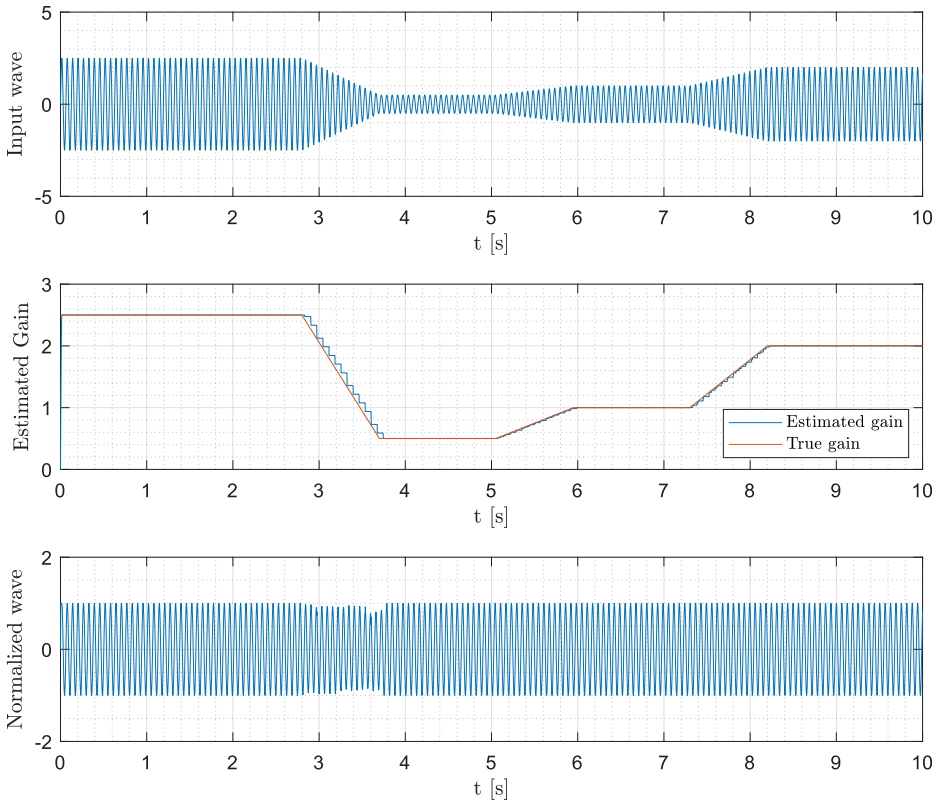

Figure 6.12: Normalizer test data. From top to bottom: 1. Input signal with varying amplitude 2. Estimated gain 3. Normalized signal

6.4 Optimized Normalizer

While the first normalizer concept performed quite good in estimating a dynamic gain to re-scale the input wave forms, some optimization was performed which has shown to produce heavy improvements in final results. Both the approaches were reported in this work to follow the logic flow that brought to the final controller design.

6.4.1 Logic, Implementation and Results

The optimization of the normalizer consists in a very slight modification to the original approach explained in Section 6.3.1. The updated flow chart is visible in figure 6.14. The only difference is on how the substitute gain MB2 is used during the update stage. In the previous configuration, while the gain stored in MB1 was being updated during the update stage, MB2 statically provided the last known MB1 gain before the beginning of the update phase. This new configuration allows for a live refinement of the MB2 gain following the same "find the maximum logic" to encompass any eventual further increase in input amplitude that may unfortunately happen during the update stage. An example of how the gains MB1 and MB2 are used by the normalizer is displayed in figure 6.13. The red line represents the output of the normalizer, during the update stage, the red signal corresponds to the output of the MB2 loop while the green one is the parallel update of memory block MB1.

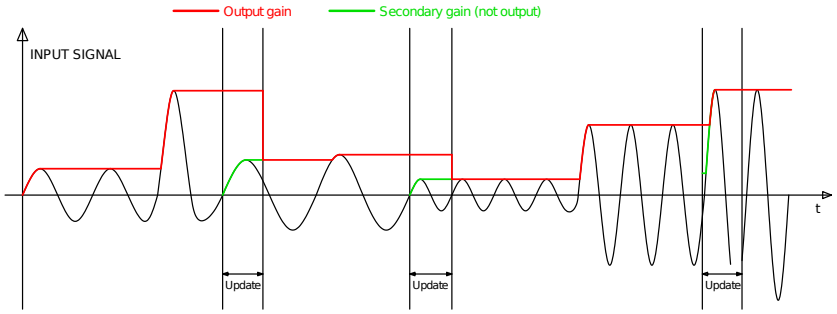

Figure 6.13: Normalizer gain example

The explanation given for the working principle of the initial Simulink system in Section 6.3.2 holds also for the updated version. The only change is the addition of a "max" block right after the MB2 memory block which is fed with the memorized MB2 gain and with the signal value. Thus two very similar loops can be distinguished in Figure 6.16. The left one, containing MB1 works as previously, determining for increases in signal value, while the second, containing MB2, provides the substitute

gain while still keeping to update it my means of the same logic used in the first loop. Switch B is always tasked to switch between the first and the second loop during non update and update phase respectively.

Concluding, the difference in the two systems revolves around how the occurrence of an unexpected input during the update stage is treated. It is for this reason that, to highlight the differences, this exact condition will be simulated and the two normalization outputs will be collected. Figure 6.17 shows the difference in performance between the two normalizers. As visible in the first subplot, a sudden step input happens during the update stage (when the update period signal is zero). The optimized approach is able to update in real-time the MB2 gain that is being fed during the update stage, thus, the system is at any instant reactive to increases in amplitude. The old configuration, instead, while also receiving the information about the sudden increase in input wave, does not output the associated gain before the end of the update time. This renders the newer configuration heavily preferable to the first one as it is in the objectives of the controller to properly react to sudden changes inputs. Figure 6.17 shows, instead, the reaction of a FLC working on the measuring device model with the old and the optimized normalizer block when a 5mm slab on the track is encountered during an update phase. As visible, the effect of the controller is still beneficial on the peak response but the reduction in amplitude is much less significant for the older normalizer version, since the gain wasn't able to adapt to the new scale of the oscillatory phenomenon and it remained the same of previous steady state condition.

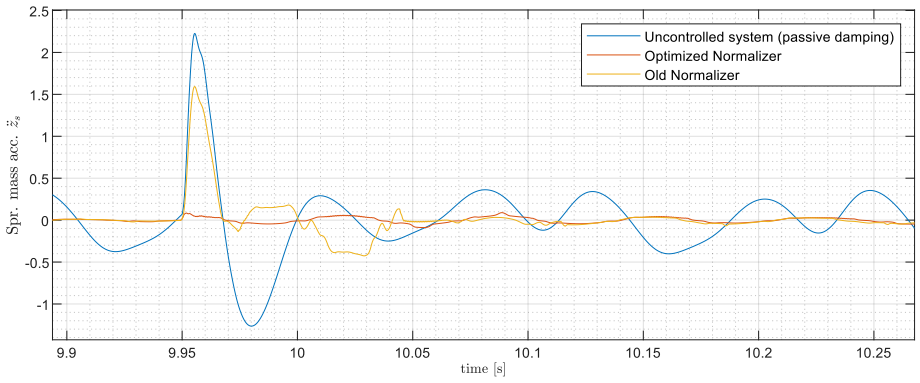

Figure 6.15: Measuring device change in performance with old vs optimized normalizer, with input 5mm slab during an update period

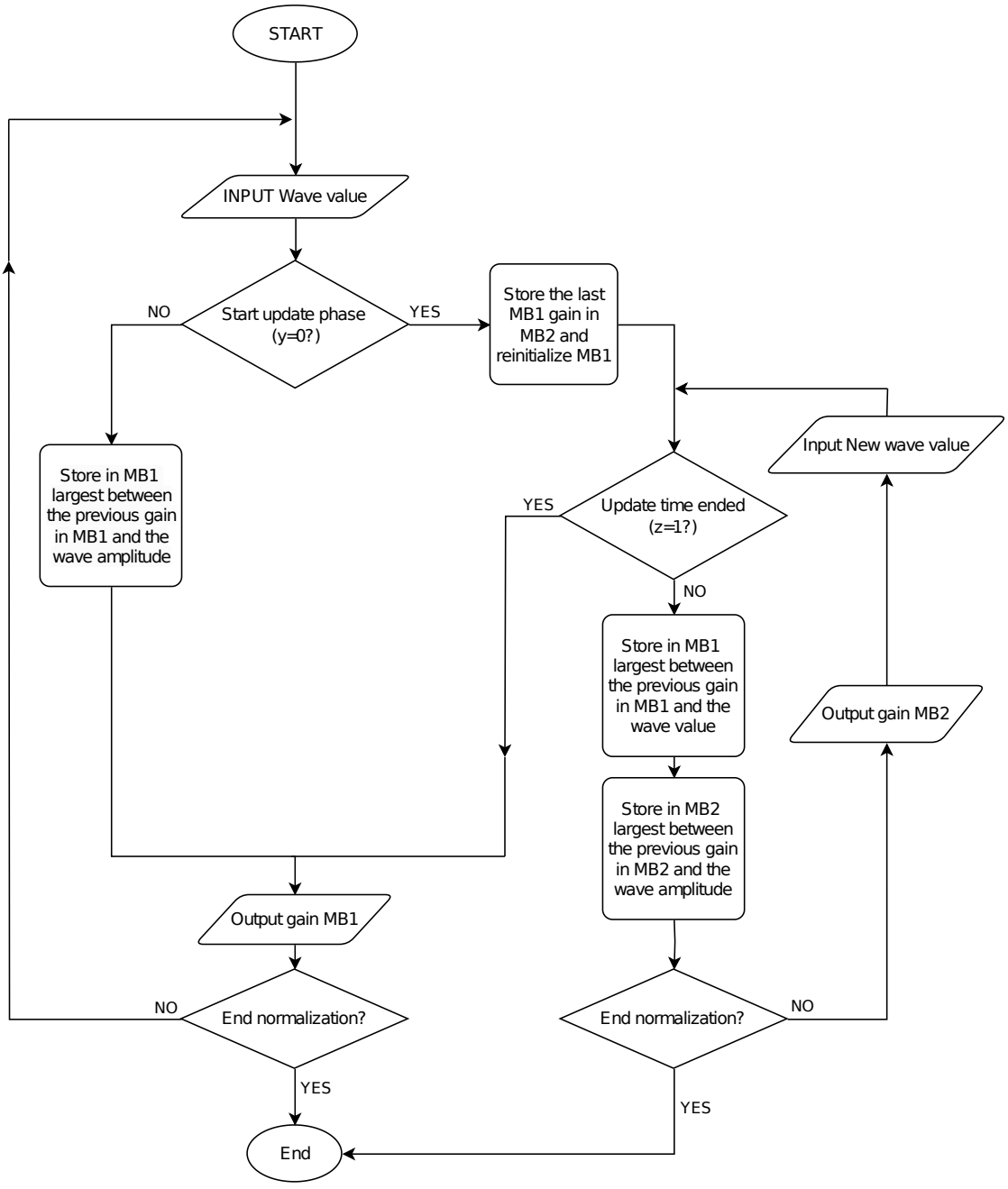

Figure 6.14: Optimized Normalizer logic flow chart

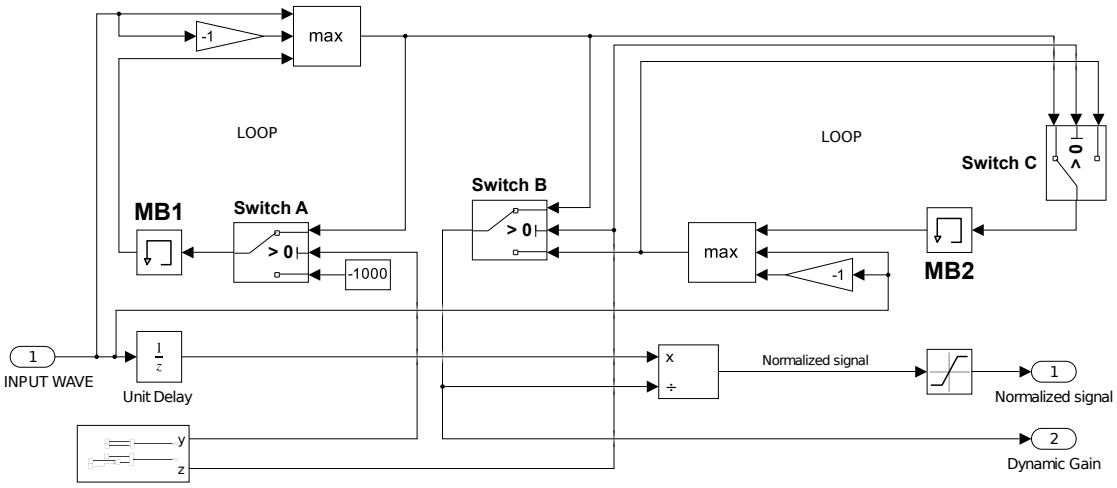

Figure 6.16: Optimized Normalizer Simulink

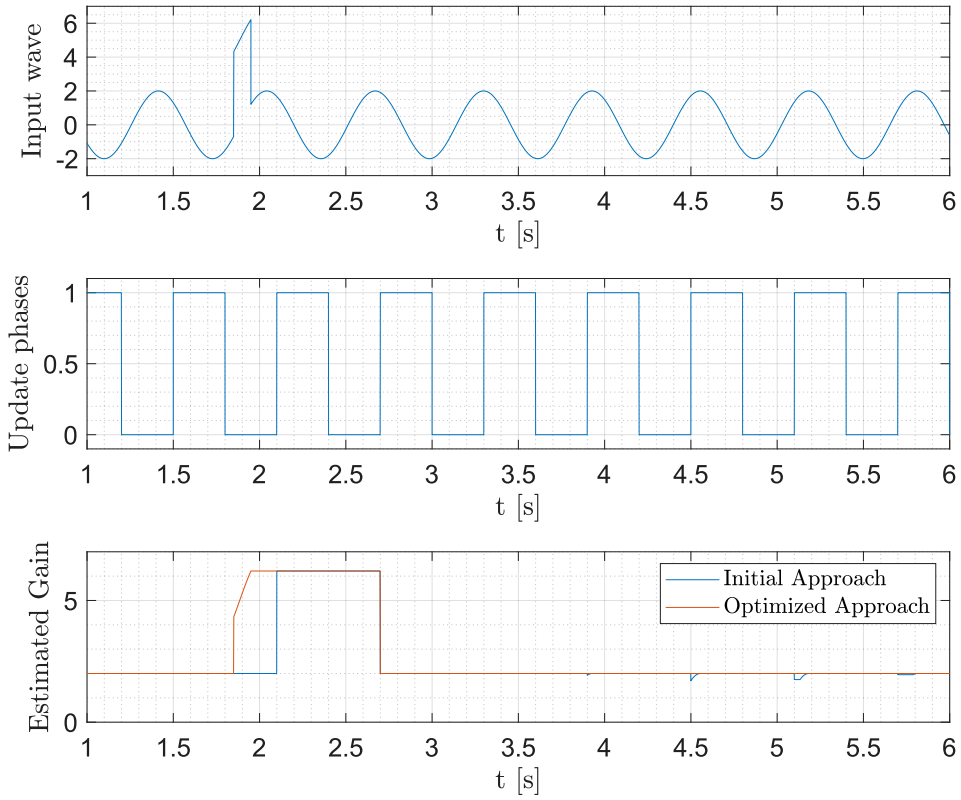

Figure 6.17: Initial vs Optimized normalizer performance, from top to bottom: (1) Input wave fed to the normalizer; (2) Update Period signal "z" (when 0 the system is updating) (3) Estimated Gains

6.5 FLC for electrodynamic levitation test-bench

The capabilities of a fuzzy logic controller strongly rely on the adequacy of the interpretation of the inputs. At the base of an FLC, there is the definition of an high enough number of membership functions, that must consent to correctly distinguish between a wide range of input combinations, in order to always have the right law to be fired. However, the definition of a fuzzy set involves a big quantity of arbitrary parameters since, as explained earlier, a single triangular membership function carries three user dependent values. Keeping the lowest complexity of input and output fuzzy sets is highly advised. In this direction, an accepted fuzzy set has been determined to be representative of all inputs sent to the FLC and it will be accepted as the optimal set for the inputs. Optimization will rather be directed towards modifying the table of rules. Anyone of the inputs considered in this study will be fuzzified following a subdivision of the input interval [-1;1] into five membership functions NB,NS,ZE,PS,PB. The goodness of such low number of membership functions is aided by the adaptive re-scaling approach explained in the previous sections. As seen in the example at the beginning of this chapter, the

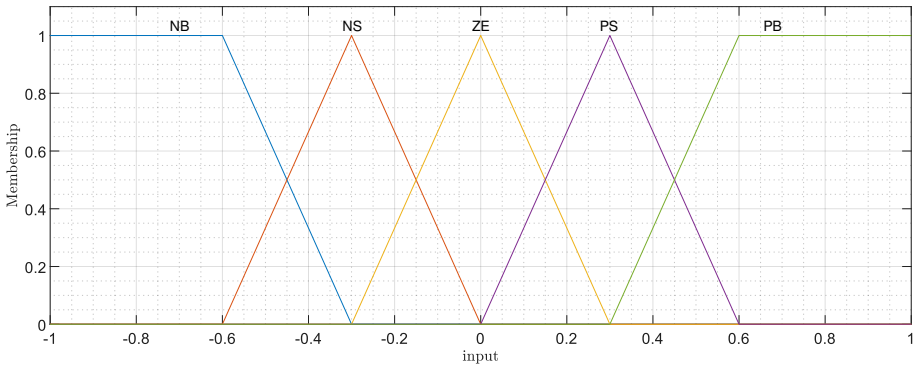

Figure 6.18: Input Fuzzy Set

dummy two-inputs - three membership functions fuzzy system required a larger number of five membership functions to be defined for the output, in order to have a certain freedom of choice when differentiating the control output to be scheduled in each one of the nine combinations of inputs. In this case, given that the input membership functions are already five, it was chosen to adopt a nine membership functions output fuzzy set that is shown in Figure 6.19. As visible, the output fuzzy set has been shaped to more accurately work between a -0.5 to 0.5 range since it was determined to be the most utilized operating range. What has previously been said can be seen in the Figure as a clustering of the membership functions towards zero.

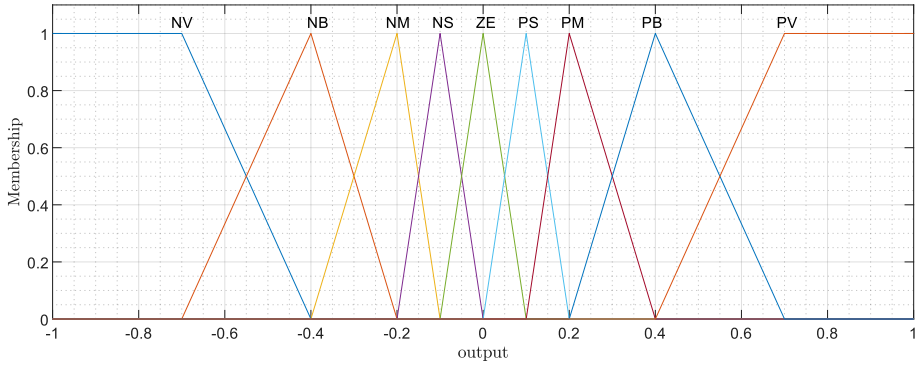

Figure 6.19: Output Fuzzy Set

6.5.1 Table of rules

Having defined input and output fuzzy sets, a preliminary table of rules can be set up, but first, a brief discussion over this topic is necessary. Defining adequate rules is the main difficulty when dealing with fuzzy controllers. Of course, also a correct definition of fuzzy sets is important but, choosing a wrong fuzzy set can still produce some good results, while choosing the wrong table of rules can produce totally meaningless results.

The tables of rules that will be proposed in this part of the work, were derived by application of human logic and they are not at all a first iteration result. Refining a table of rules to achieve the expected behavior is a very tedious task and heavily relies on the acquired expertise about the system's performance. Defining a set of rules means filling the n-way, k-entries table with n being the number of inputs and k being the number of combinations of all the membership functions. At first, it was chosen to start with an easy enough two inputs system as it is easier to manage. The chosen inputs are the sprung mass acceleration $\ddot{z}_s$, which is the state to be controlled, and the sprung-unsprung mass relative velocity, which can provide hints on what force is or will be exchanged between the two masses. With the proposed fuzzy sets, a 5x5 two-way table is generated for rules.

The designer must go through every single combination and make an appropriate choice for the output voltage. It means that he should think to the physical meaning of each combination of inputs and "tell" the inference system what to do in case such combination occurs. The controller, thus, does not output any result of mathematical operations like LQR or PID controllers would do, it limits to follow its training table which basically means that its performance goodness is directly related to the knowledge the designer has about the system's dynamics. The logical process of determining the rules is hereby explicitly explained for some

of them.

"If $\ddot{z}_s$ is NB and v_{rel} is NB, then the output V is PM"

Remember that a positive voltage on the voice coil produces an upward force on the sprung mass and an equal but downwards force on the unsprung mass. Thus, if $\ddot{z}_s$ is Negative Big (NB) and v_{rel} is also Negative Big (NB), in order to reduce $\ddot{z}_s$, a positive voltage must be applied on the sprung mass and, being the acceleration already big, a big value of positive output voltage is suggested by the first input. The information about the relative velocity suggests, instead, that the two masses are getting rapidly one towards the other. This means that the spring and damper linkage between the masses is itself going to provide two upwards forces. The first is produced by the passive damper and proportional to the relative speed, and the second one will be produced by the spring once that it has achieved a compressed configuration or anyway, if the spring remains in an elongated configuration, a reduction of its upwards force will be perceived. On an overall, thus, the acceleration suggests to apply a big positive voltage, while the relative velocity suggests to be precautionary since, already, a positive force is going to appear from the linkage elements. The final choice is to adopt a Positive Medium (PM) output voltage.

The reverse case is the following one

"If $\ddot{z}_s$ is NB and v_{rel} is PB, then the output V is PV"

In this case, again, both the inputs are the highest they can be but their sign has changed. If in the previous case the relative velocity effect favored the control action, in this case, where the sprung mass acceleration is still negative big and it would require a positive big control voltage, a further force towards the bottom is exerted by the linkage elements. In fact, since the relative velocity is positive big, the two masses are rapidly detaching and an increase of total downward force will be experienced by means of the spring-damper connection. For these reasons, the control voltage will be more aggressive and it is set to Positive Very big (PV) instead of Positive Big (PB).

Proceeding in this way, one can determine the table of rules shown in Table 6.3.

6.5.2 Control surface

The best way to visualize the imposed rules is to plot the control surface. This surface contains a discretization of the defuzzified outputs corresponding to each point in the range of variation of the inputs. Visualizing the rules through a control surface helps to determine whether the inference follows a trend and highlights the presence any eventual outlying rule.

As visible in Figure 6.20 (a), the shape of the defuzzified output shows a distinct trend and the inference system can thus be applied in the control loop. Before

$\ddot{z}_s \downarrow v_{rel} \rightarrow$	**NB**	**NS**	**ZE**	**PS**	**PB**
NB	PM	PM	PB	PB	PV
NS	ZE	PS	PM	PM	PB
ZE	NS	NS	ZE	NS	PS
PS	NM	NM	NM	NM	NS
PB	NV	NB	NB	NB	NM

Table 6.3: 2-D table of rules

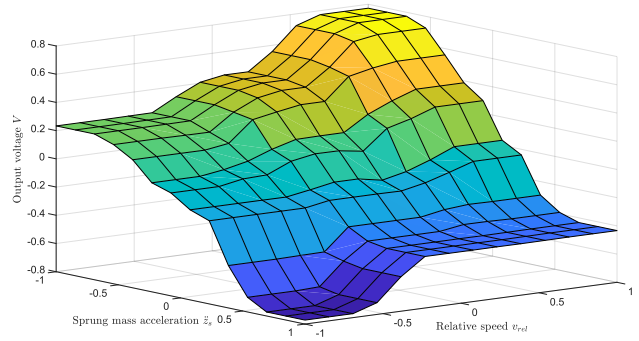

(a)

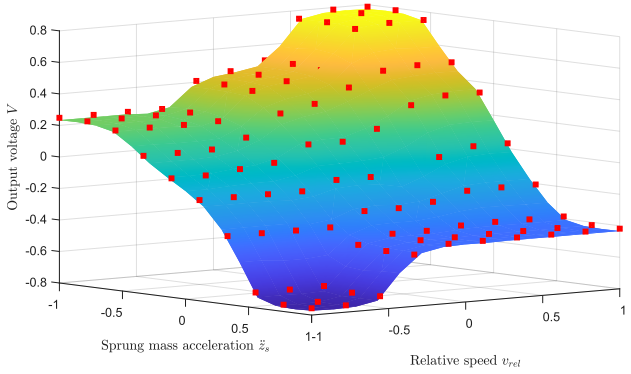

(b)

Figure 6.20: (a) Original Surface (b) Sub-Sampling

implementing it, it is useful to slightly modify the control surface. It has been seen that fuzzy controllers are very prone to produce numerical noise. Such noise can be a consequence of not so smooth shape of the control surface. As mentioned in the first section of this chapter, there are many different types of membership functions such as pi shaped, sigma shaped and Gaussian that, differently than triangular ones, can produce a smoother transition between one rule to another. Anyway, also

by using triangular functions, the output can be smoothed out by post processing the control surface. The adopted approach was that of sub-sampling the control surface in a broad enough grid of point and then build a cubic interpolation of the sub-sampled points. In this way, the sharp angles are smoothed out. The same sub-sampling procedure will be followed also when three input inference systems will be proposed. In that case, though, the visualization is not so easy as a 4D surface will be dealt with.

6.6 Simulink implementation

The Control logic seen in figure 6.8 is introduced in Simulink and the full control system with 2D control surface is shown in figure 6.21. Notice that, on the control signal line, a transfer function is necessary to avoid algebraic loops but it does not affect the control signal as its cut off frequency is set to a very high value (5kHz). On top of the transfer function block, a saturation is needed to avoid excessive voltages to be applied to the voice coil.

A "tunable" static gain is visible on the control signal line. This element has a pivotal role in the goodness of the performance of the controlled system.

The output signal coming out of the control surface lookup table is multiplied by the dynamic gain. This serves the purpose of generating the right profile of the control signal and the right relative magnitude. The word "relative" is crucial for some aspects. The control signal must have magnitudes that range according to the magnitude of the input, thus, at each time step, the magnitude of the output must be compliant with the magnitude of the input. However, this compliance is not enough to guarantee that the control signal is large (or small) enough to introduce sensible improvement in performance. All the output signals must then be multiplied with this "tunable" static gain to bring them to a dimension where the shape of the control signal actually impacts the comfort performance. For example, for the same input acceleration values, the tunable gain must be higher if the mass is larger and vice versa.

6.6.1 Tunable static gain

The choice of an adequately high static gain heavily impacts performance up to a certain value. After such value (for the system under consideration around 60), the response settles around a certain RMS value. Then the RMS degenerates to infinity or to a certain value due to the presence of a voltage saturation. A possible explanation to this behavior is the following.

When the gain is too low, the control force cannot reach high enough values, since the output signal from the control surface ranges in [-1;1]. When raising the

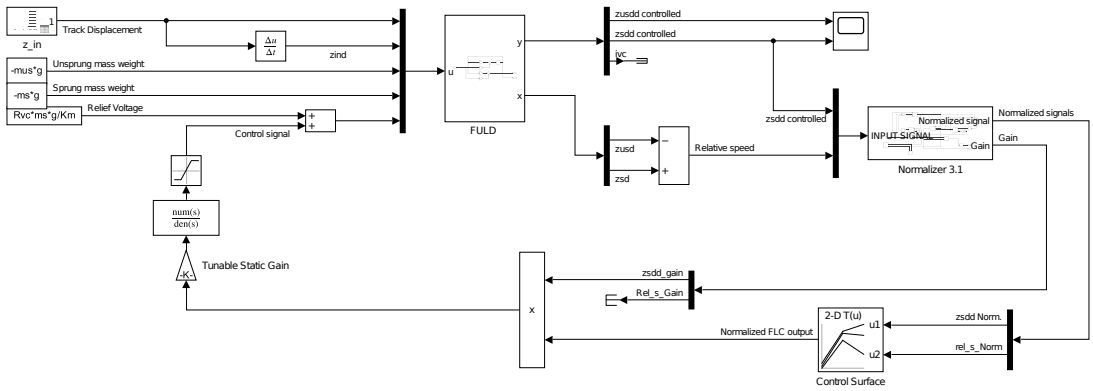

Figure 6.21: FLC implemented on Simulink

static gain the force becomes adequate to accelerate the masses of the system and the behavior improves with increasing gain.

After a certain limit gain, the improvement is marginal and the behavior settles around a certain optimum, this happens because, if it is true that the force should be greater, it is also true that the normalizer, "seeing" that the fierce reaction of the controller suddenly lowers the sprung mass acceleration, produces very low dynamic gains, that somehow kill the high imposed static gain. There is a sort of balancing between the dynamic gain and the static gain that makes the overall gain be similar for any imposed static gain over a certain threshold. What has just been said is confirmed in figure 6.22 where a curve shows the behavior of the RMS of the sprung mass acceleration when the track with a slab is used. As clearly visible,

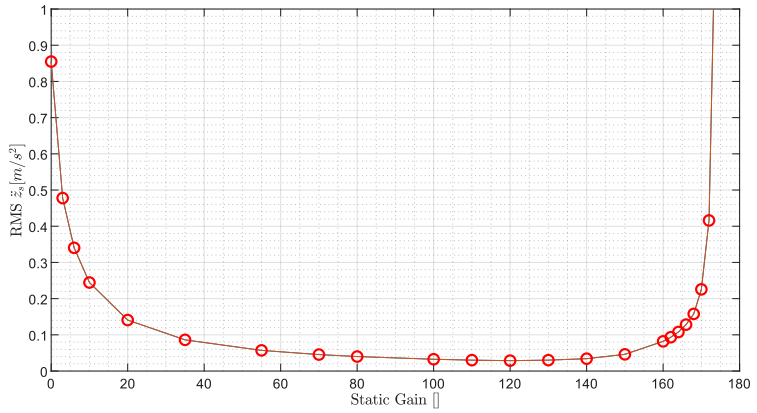

Figure 6.22: Effects of the tunable static gain

the response amplitude falls drastically from the uncontrolled behavior (when the static gain is zero) into a plateau where it remains quite stably up to a value of

150. After such value, the response seems to inexplicably tend to infinity.

This instability happens because the control action is so fierce that the system responds too abruptly for the normalizer to be able to keep-up with the update stage. It means that the update phase is too slow for the utilized gain, and the normalizer is not able to catch up and produce the small gain that has to compensate for the high static gain because, until the update time has elapsed, the fierce action has already put the system at high acceleration amplitudes. Thus the controller auto induces instability.

Resuming, the reason for instability with very high gain is connected with the duration of the update stage and update period.

The proof of this explanation is provided in Figure 6.23, where the curve shown in Figure 6.22 is superimposed with a similar one obtained adopting a shorter normalizer period (one half). Notably, the initial fall in RMS is quite similar but it's clearly visible how the "plateau" extends to higher values of gains proving that the instability occurs due to the slowness of amplitude estimation. Regardless, this matter about instability serves just as an additional remark about the dynamics of this system. Therefore, the most important outcome of this study is that, above a certain value, (usually around 60), the response isn't sensitive to the value of the static gain, thus it is not necessary to perform a precise optimization for every case study, in fact, it is enough to rely on an "high enough" gain that can be found in a couple of trial and error iterations on Simulink.

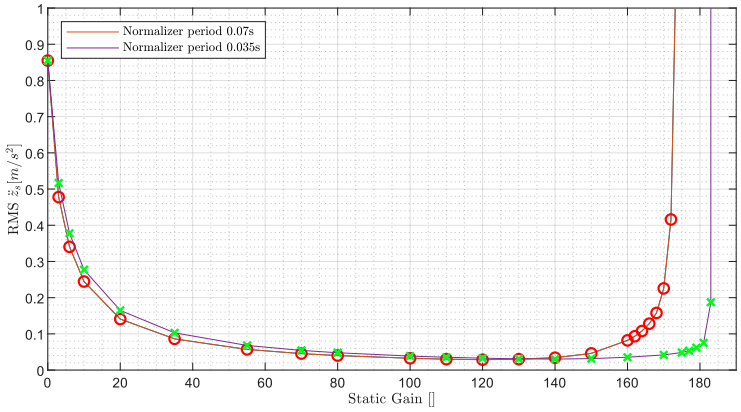

Figure 6.23: Effects of the tunable static gain and Normalizer period

6.7 Results

The results produced by this control logic will be shown as matter of time domain responses of the controlled system vs the uncontrolled one, and the goodness of

the improvement in comfort will be classified with a coefficient, allowing to rapidly grasp the performance difference between various case-studies. The coefficient will simply be the ratio between the RMS of the uncontrolled response and the RMS of the controlled one, so it tells how many times better (or worse) the controlled system performs with respect to the uncontrolled one. (Note: When not specified, the track rotational speed is considered to be 500 rpm).

The control system performance will be checked in three testing scenarios:

- Track irregularities, shown in Figure 3.4;
- Track irregularities with copper slab shown in Figure 3.6;
- Random road profile according to ISO norm.

While the first two cases were already presented in the previous chapter, random road irregularities [18],[9] deserve some words. ISO norm presents an approach to produce a road profile with different quality, from very good (A road class) to very poor (E road class). Relentless, such definition is associated with the scale of road vehicle and cannot be used on the much smaller electrodynamic levitation system taken into account. The irregularities are re-scaled in a way that the amplitude of the measured irregularities falls in the "average" road class (C). The resulting input track profile is displayed in Figure 6.24.

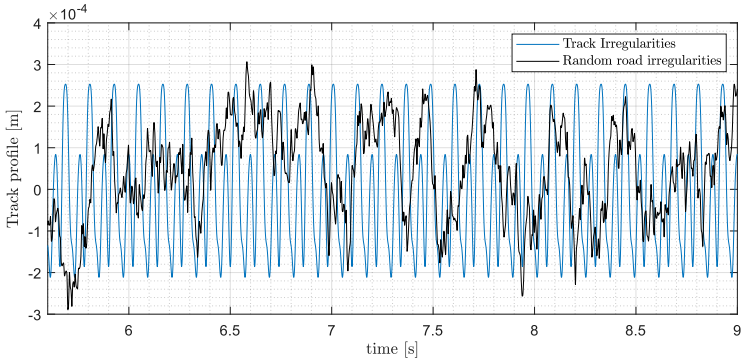

Figure 6.24: Random Road Irregularities C "average" road class

6.7.1 Track Irregularities

The time domain behavior of the controlled system subjected to track irregularities is shown in Figure 6.28. The RMS ratio and the percentage reduction in RMS is written below

$$RMS_{ratio} = 20.1$$

Which corresponds to a 95% reduction in RMS value of acceleration. Figure 6.28 shows also the shape of the control voltage signal. Figure 6.29 displays the normalized wave that is fed to the control surface and the dynamic gain behavior. A further check on the goodness of the result may be performed by checking for the force balance on the sprung mass. In this pursuit, Figure 6.25 displays the forces acting on the sprung mass. The blue curve shows the force that is applied by the actuator on the sprung mass, while the orange one shows the transmitted force through spring and damper couple. As expected, the two curves show a very noticeable symmetry. The symmetry is not perfect and the discrepancy is shown in green in the same plot. This residual force is what produces the non zero acceleration all over the time domain.

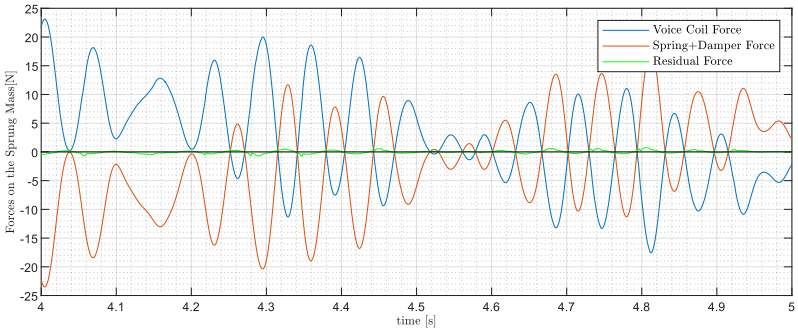

Figure 6.25: Forces acting on the sprung mass, Input track irregularities. In blue the VCA force, in orange the spring+damper connection force. In green, the residual force

6.7.2 Slab

In this case a sudden step is set on the track profile, as shown in section 3.1.1 in Figure 3.6 to check for the reaction of the system to sudden input excitation. In this case the RMS ratio is

$$RMS_{ratio} = 24.0$$

Which corresponds to a 95.8% reduction of the acceleration RMS. Then, the improvement in performance in this second case is even more pronounced than in the previous case. Figure 6.30 displays the sprung and unsprung accelerations in controlled and uncontrolled configuration together with the control voltage. Figure 6.31 shows the Normalizer output signals and gains. Once again, a verification can be made on the control forces to check for symmetry. Remark that, in this case, the best performance of this control strategy is witnessed. This could be due to the fact that this case contains the excitation of different regimes of motion. The first regime, in which just small sinusoidal irregularities act, and the second regime, in which the magnitude of the oscillation is much wider due to the step. So this

test scenario is the closest, among the three, to the case for which this controller was designed for, so a dynamic system that faces varying oscillatory regimes.

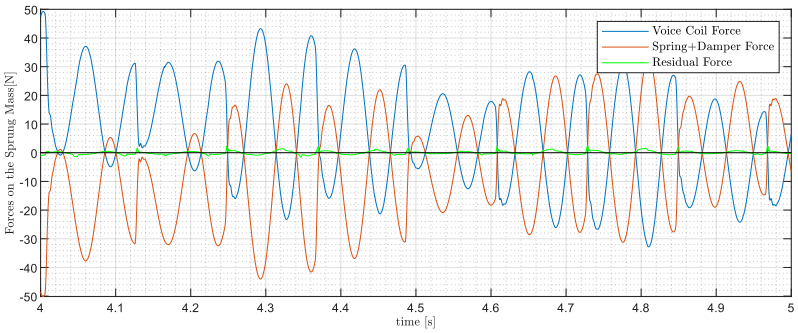

Figure 6.26: Forces acting on the sprung mass, Input track with Slab. In blue the VCA force, in orange the spring+damper connection force. In green, the residual force

6.7.3 Random road irregularities

With the assumptions made at the beginning of this section, and with the random irregularities being like shown in Figure 6.24, the response shows an improved behavior of

$$RMS_{ratio} = 6.87$$

Corresponding to a reduction of the 85.4% of the sprung mass acceleration RMS. Figure 6.32 shows the sprung and unsprung mass accelerations for the uncontrolled and controlled configuration, together with the control Voltage. Figure 6.33 displays the normalizer output. As done for the previous cases, a cross check on the force balance on the sprung mass, shown in Figure 6.27 is useful to prove the goodness of the results. Notably, this is the case in which the improvement is less evident.

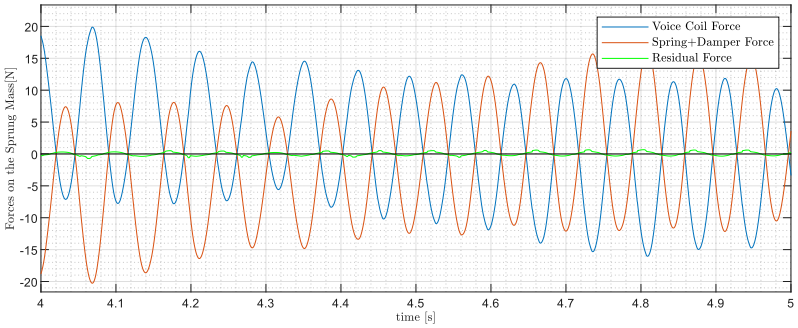

Figure 6.27: Forces acting on the sprung mass, Input ISO C road class. In blue the VCA force, in orange the spring+damper connection force. In green, the residual force

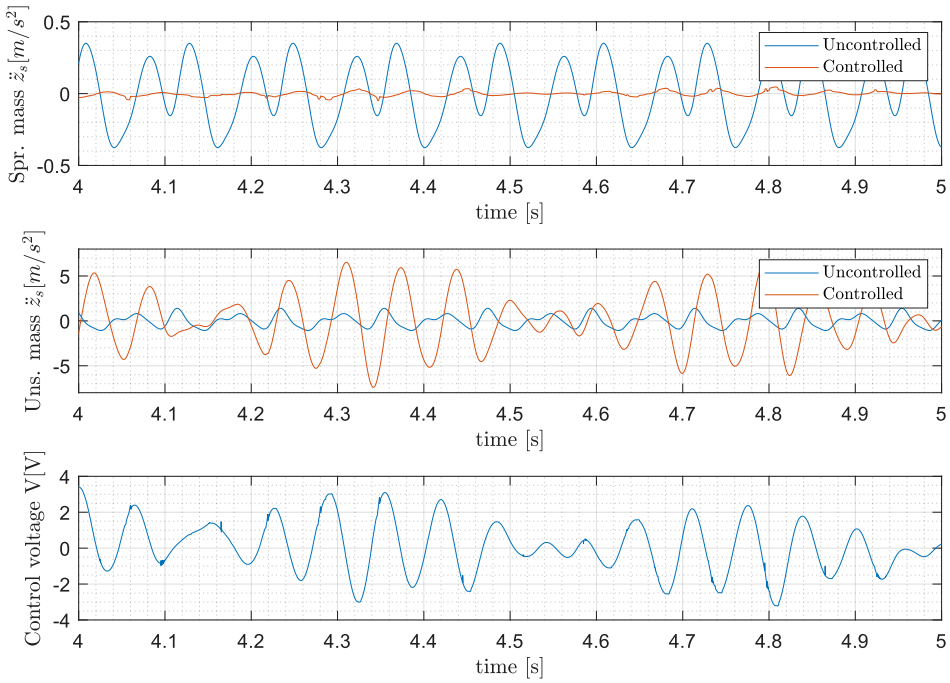

Figure 6.28: Time domain response Controlled vs uncontrolled system input track irregularities, from top to bottom: (1) Sprung mass acceleration controlled vs uncontrolled; (2) Unsprung mass acceleration; (3) Control Voltage. Results with static gain set to 90, normalizer period 0.07s

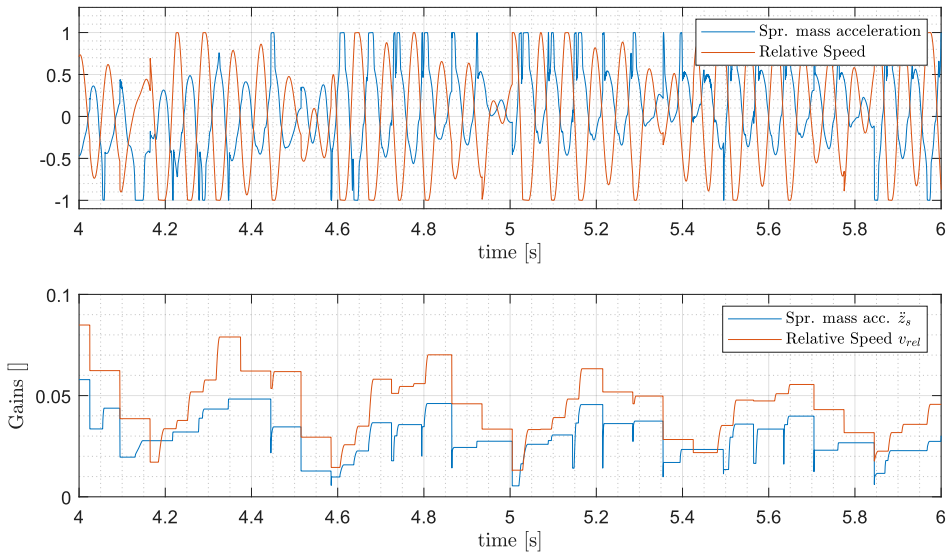

Figure 6.29: Normalizer behavior Input track irregularities. Normalized signals (top); Gains (bottom).

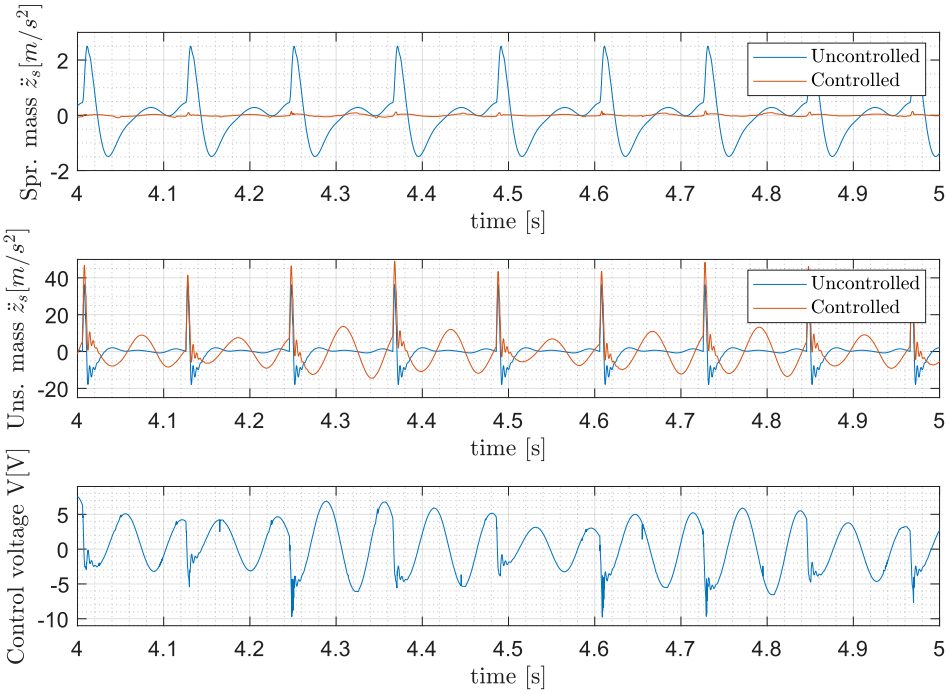

Figure 6.30: Time domain response Controlled vs uncontrolled system input Track with slab, from top to bottom: (1) Sprung mass acceleration controlled vs uncontrolled; (2) Unsprung mass acceleration; (3) Control Voltage. Results with static gain set to 90, normalizer period 0.07s

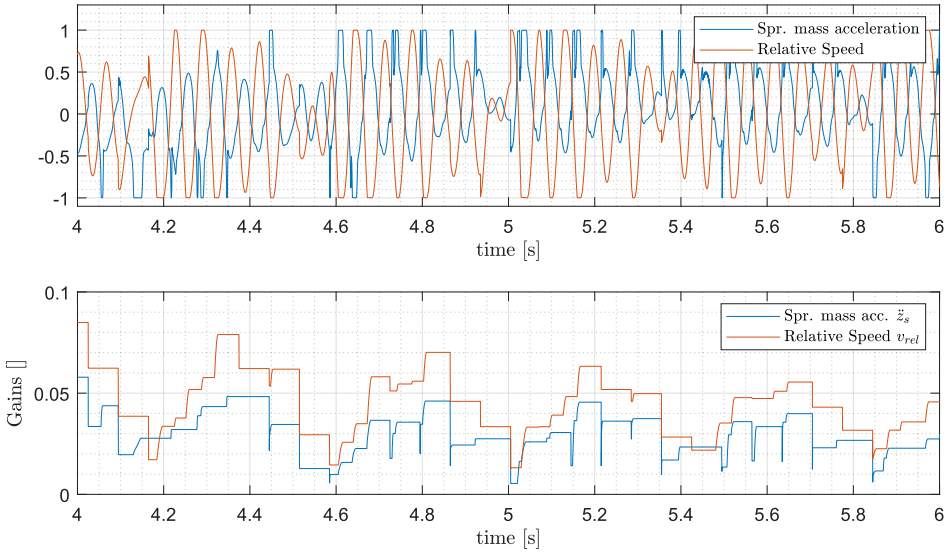

Figure 6.31: Normalizer behavior with input slab. Normalized signals (top); Gains (bottom).

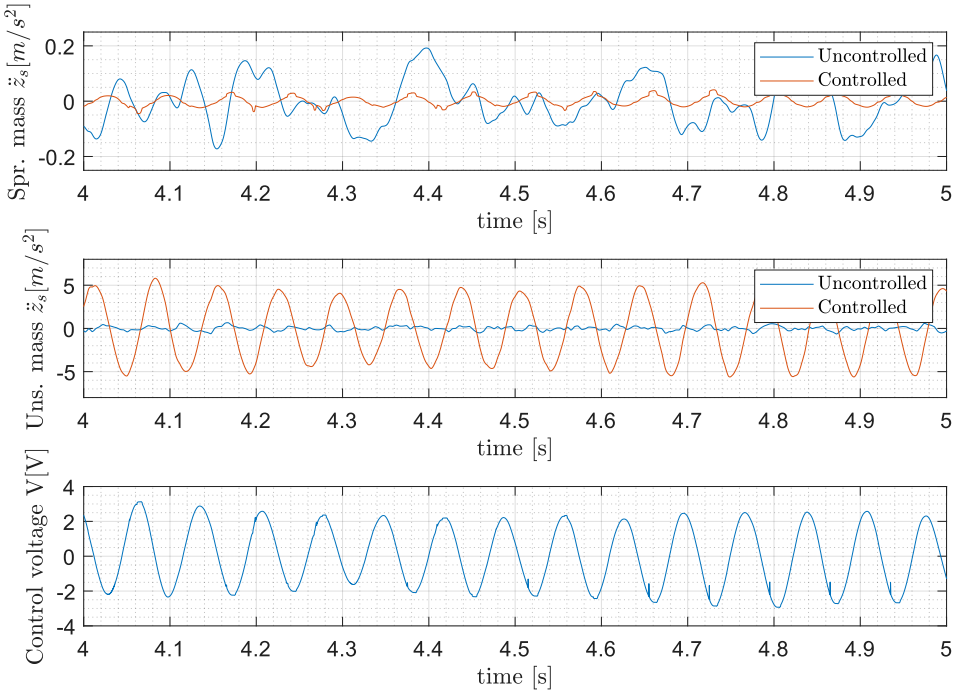

Figure 6.32: Time domain response Controlled vs uncontrolled system input ISO C road class, from top to bottom: (1) Sprung mass acceleration controlled vs uncontrolled; (2) Unsprung mass acceleration; (3) Control Voltage. Results with static gain set to 90, normalizer period 0.07s

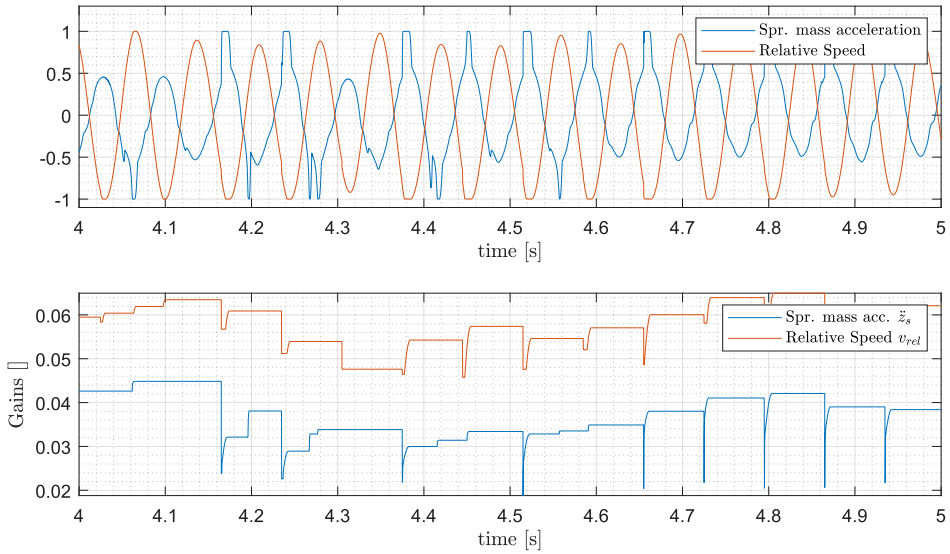

Figure 6.33: Normalizer behavior with input ISO C road class. Normalized signals (top); Gains (bottom).

6.8 4D Control Surface

The integration of the normalizer approach with the fuzzy control surface makes, on an overall, the system's behavior less sensitive to wrong applied rules. This is because, as soon as the system applies a wrong rule, the normalizer detects a destabilizing effect and, just like if it was an external disturbance, it works on the dynamic gain to reduce its impact. However, this does not mean that the system can work with random rules, they have to be consistently defined even though the methodology allows to compensate for a certain extent of erroneous rules. Thinking to a set of rules that was suitable for a two-inputs, 25 combinations inference system was a manageable task and the results have been proved to be quite good. The same cannot be said if one wanted to exploit more than two inputs to produce a control surface that is defined in a 4 dimensional space that can be displayed by means of a scatter plot. Sticking with the 5 membership functions input fuzzy set and extending it to all three inputs, one has a 125 three ways table entries to define. Each one of the entries of such table, must be considered by the designer and he should decide what is the best course for the controller. It is trivial to say that it is very easy to make mistakes, and some of the 125 rules will not be the best ones to apply. Furthermore, considering that the difference between one case and another can be very slight to allow the designer to schedule any difference in control action, the process is particularly tedious.

Anyway, some attempts have been made in order to exploit all three inputs related to the electrodynamic levitation test bench (sprung mass acceleration, unsprung mass acceleration and relative speed). Following a similar logic to what seen in the definition of rules for the 3-D control surface one may write all 125 rules. For example

"If $\ddot{z}_{us}$ is PS and v_{rel} is NS and $\ddot{z}_s$ is NB, then the output V is PM"

Being the acceleration of the sprung mass Negative Big, a Positive Big voltage is suggested. The relative velocity is Negative Small, meaning that the two masses are slowly coming one towards the other. The unsprung mass is instead accelerating upwards (Positive Small acceleration). The upward acceleration of the unsprung mass and the downward acceleration of the sprung mass implies that the relative velocity, that is already negative, will assume larger negative values so, soon, an up-bound force is expected to act on the sprung mass from the spring-damper linkage. For this reason, the control signal will be set to Positive Medium instead than Positive Big.

For brevity, the full table of rules is not reported here, instead, the control scatter plot is directly presented in Figure 6.34. Once again, this kind of representation of the table of rules allows to identify for a general trend of the logic and to look for any evident outlaying rule. The result of a controller working with such control

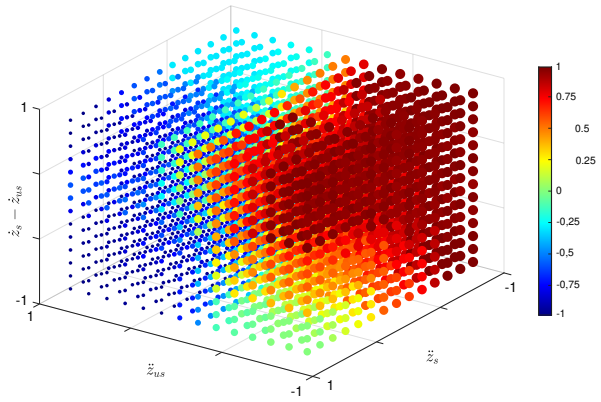

Figure 6.34: Designer defined scatter plot 3 inputs inference system: Sprung and Unsprung mass acceleration and relative velocity

surface is shown in Figure 6.35 where ISO C road class has been taken as a test scenario since it was the most critical one in the previous paragraph. In this case the result is quite unsatisfactory, even though it still shows some improvement on the RMS as the best obtained RMS ratio is

$$RMS_{ratio} = 5.2$$

And it comes with too much numerical noise. To keep an adequately low control noise and voltage amplitude, the RMS ratio must be kept below around 3.5 (it is the case shown in figure). The main issue is the very oscillatory behavior of the sprung mass acceleration. This is a result of a quite noisy control voltage as visible on the third subplot. What generates this noise is the firing of many non-optimal rules that continuously excite the system and, to whose excitation, the normalizer approach tries to react. Furthermore, a series of unexplained peaks are visible on the controlled sprung mass acceleration response. These peaks do not correspond to any particular impulse coming from the track, they just show up due to one or more than one completely wrong rules.

It is apparent that the anticipated issue about rule based control is supported in this instance. In fact, increasing the number of inputs from two to three has brought the table of rules from 25 to 125 entries. If the 25-rules table was quite manageable, in this case it is very difficult to make changes and to check for their effectiveness. Therefore, the initial notion of exploiting all available input data to achieve an enhancement beyond the two-input control appears to be vain.

Notice that the 4-D surface that was just presented is already child of many iterations trying to improve it's performance. Given the unsatisfactory results, another approach has been followed and is presented in the following paragraph to make it possible to take advantage of all available data to possibly get even better outcomes.

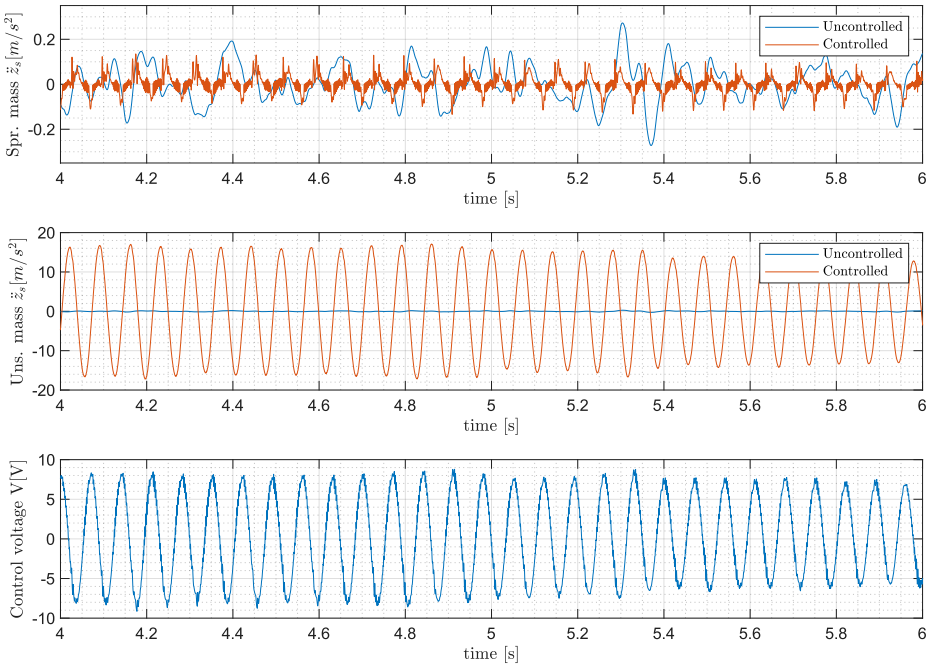

Figure 6.35: Designer defined 4D Control Surface Performance with input ISO C road class, from top to bottom: (1) Sprung mass controlled vs uncontrolled acceleration (2) Unsprung mass controlled vs uncontrolled acceleration (3) Control voltage

6.9 Training Fuzzy inference systems

Given the difficulties encountered when defining a large number of rules to build a 4-D control surface based on human logic applied to mechanical system dynamics, a different approach was attempted in order to take advantage of the full available data.

Undoubtedly, when trying to develop a control surface by applying human logic, there are input combinations that are way easier to manage than others. In the approach presented in the previous paragraph, designer's logic was applied to the only three available inputs, with them being sprung and unsprung mass acceleration and relative velocity. There wasn't much arbitrariness on the set of inputs as any other input cannot actually be obtained with the current experimental setup.

The idea proposed in this section is to take advantage of "easier" to manage inputs, such as jerk and acceleration, to build a control surface based on those signals, even if they are not available as inputs in reality, and try to translate the content of such surface into a table of rules working with available input signals. A very simple inference system training algorithm will be presented and the systems involved will be referred to as "training or trainer" and "trained".

First of all an "empty" (without rules) inference system must be defined to receive

the training rules. This means that the input membership functions and the empty table of rules must be defined.

The approach consists in making the trained system work in a training simulation under some random conditions, in order to activate all the possible combinations of inputs of the trained inference system. The normalized control signal output by the training system (working with the unavailable inputs) in this condition is acquired together with the values assumed by the trained system inputs. Then, the acquired signals are post processed.

The input fuzzy sets of the trained system are divided in crisp classes for simplicity, in order to have defined bounds to classify the signals at the various time steps. Figure 6.36 displays the meaning of the last statement. For example, every input that belongs to the [-0.15 +0.15] range will be considered as Zero (ZE), every input in [0.15 0.45] range will be classified as Positive Small (PS) and so on.
.

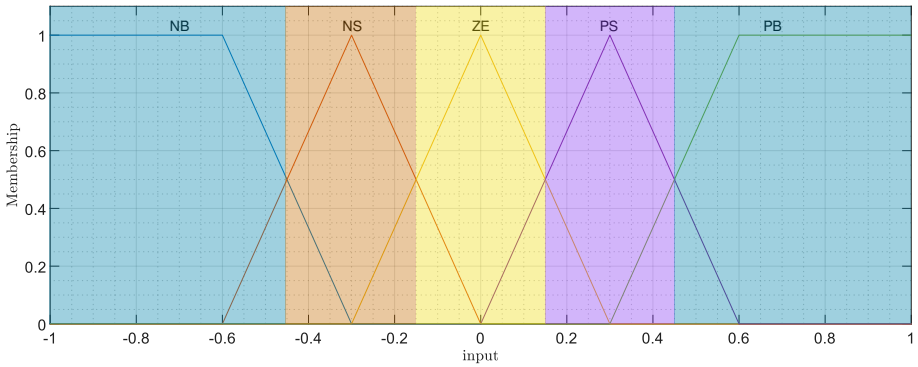

Figure 6.36: Classification of training inputs in crisp classes

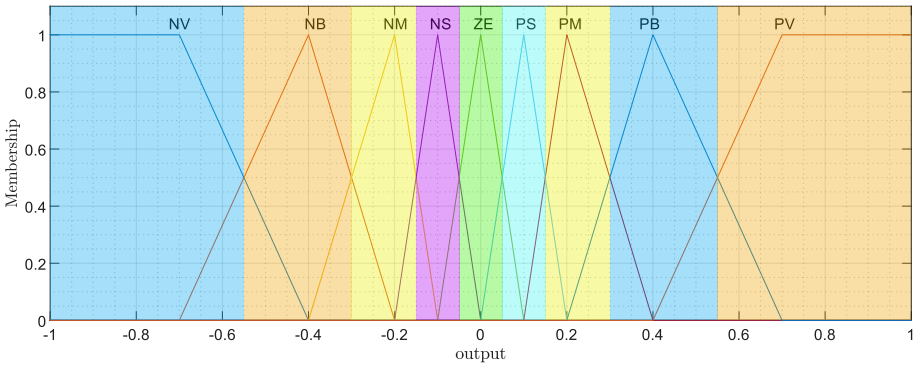

Figure 6.37: Classification of training outputs in crisp classes

The time steps containing the desired combination of the input classes will be looked after in the acquired time domain signals and, once that the time instants have been identified, the average action taken by the controller will be determined and the rule corresponding to the considered combination of inputs will be collected.

Making an example is the best way to understand this logic: If we are looking for a rule to fire when all three inputs ($\ddot{z}_s, \ddot{z}_{us}, v_{rel}$) are all Positive Small (PS), firstly, the bounds to consider the input as PS must be defined, and, as said, they are 0.15 and 0.45 (since in this range the Positive Small (PS) class is the "most activated class" in the original fuzzy set). Once that these bounds are set, we look for all the time steps in the training simulation time domain data that satisfy the condition that all three inputs fall in the range [0.15 0.45]. Then, the corresponding control signal is looked after for each one of the determined time steps. All the control signal values are then averaged and the average value is input in to a crisp logic set of the output shown in Figure 6.37. The mean value will correspond to only one class of the crisp set and that class will correspond to the rule imposed on the trained system.

This is a simple approach that passes through two accepted crisp sets to determine the rules. Notice that a choice was made to classify an input and an output as belonging to a certain class when the corresponding fuzzy logic class is activated with more than 50% degree of truth. Also, other criteria may be adopted, such as increasing this activation threshold to higher values. For example, to activate an input class when the corresponding fuzzy logic class is activated with more than 75% degree of truth. Another possibility to perform this classification task would be to reverse the inference system to avoid referring to crisp sets but to consider the original fuzzy sets. The feasibility of this approach will not be explored in this thesis.

6.9.1 Acceleration and Jerk control surface

Among the various pairs of input states, the acceleration-jerk combination proves to be quite convenient in establishing reliable rules with a low probability of errors.

In fact, in all attempts for determining control rules, the approach has always tended to predict what is the future of the sprung mass acceleration in order to provide a rule that takes into account both the current condition and the one that will soon come. Having available both acceleration and jerk data means having directly clear and unquestionable information about the current and the near-future behavior of the sprung mass acceleration. In a numerical context it is very easy to obtain a clean jerk signal by using a derivative block with appropriate filtering, if needed. The same cannot be said for the experimental stand point, where, obtaining clean derivatives of measured states is not an easy task. This is where the proposed approach comes into play, as explained in the introduction, the

easy pair of acceleration and jerk will be utilized only on the numerical context and will be used to teach an inference system working with the available inputs.

The same 5 membership functions fuzzy sets in [-1 1] will be used also in this case. The 25 rules are quite self explanatory, anyway an example is provided for clarity:

"If $\dddot{z}_s$ is PB and $\ddot{z}_s$ is PB, then the output V is NV"

In this condition not only is the acceleration high, but also is its rate of growth, thus, the control action should provide the fiercest possible downward force, for this reason, the control voltage is set to Negative Very big (NV). The full table of rules for such control is provided in Table 6.4 and the control surface is visible in Figure 6.38. Figure 6.39 shows the improved behavior

$\dddot{z}_s \downarrow \ddot{z}_s \rightarrow$	**NB**	**NS**	**ZE**	**PS**	**PB**
NB	PV	PV	PS	NS	NS
NS	PB	PM	PS	NS	NM
ZE	PB	PM	ZE	NS	NB
PS	PS	PS	NS	NM	NB
PB	PS	ZE	NS	NB	NV

Table 6.4: 2-D table of rules

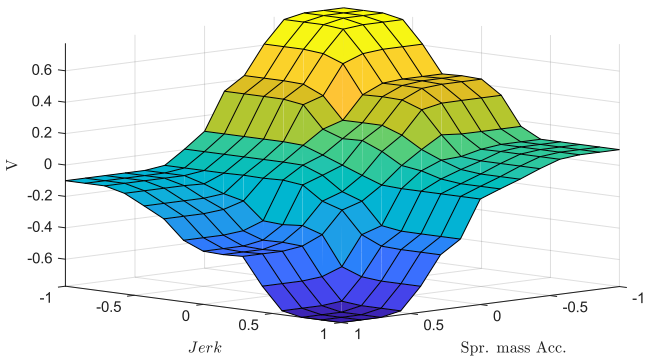

Figure 6.38: Fuzzy Control surface with input jerk and acceleration

The behavior of the controlled system with input jerk and acceleration shows more than twice the improvement in RMS with respect to what seen in the previous sections for track irregularities and impulse. This controller, thus, produces an ideal control signal that should be the reference one for the trained controller.

The proposed approach for training is displayed in Figure 6.40 where 4 out of 125 input classes combinations are reported. In such figures, the magenta points

RMS ratios	Rel.Speed and Acc.	Jerk and Acc.
Track irregularities	20.1	47.1
Track irr. and slab	24.0	56.1
ISO C Road Class	6.87	9.50

Table 6.5: Preliminary control performance comparison

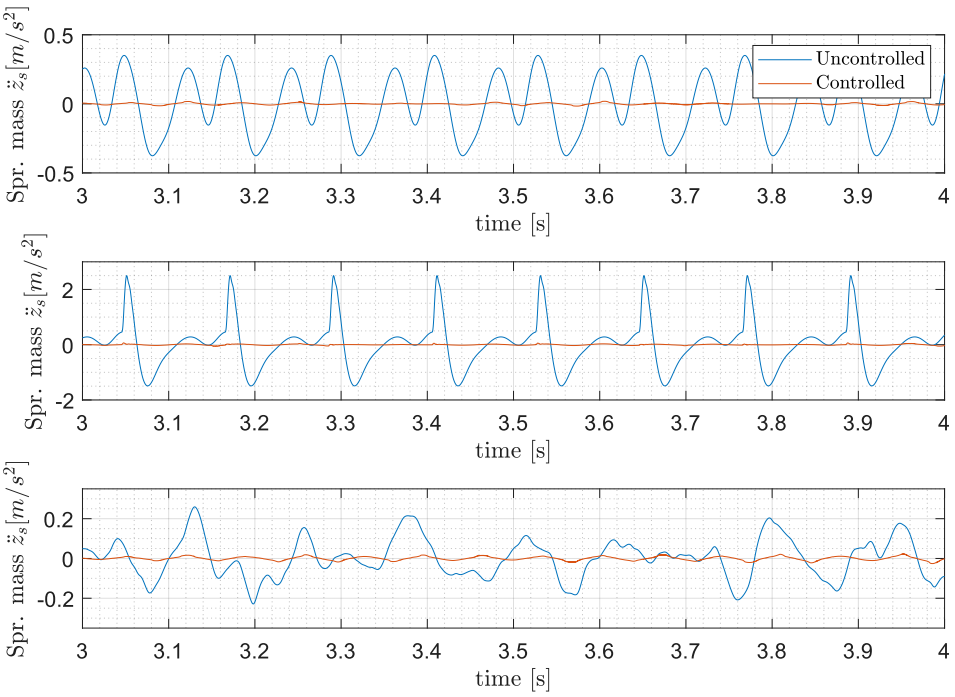

Figure 6.39: Jerk and acceleration response to various inputs. From top to bottom: (1) response to measured track irregularities; (2) Response to measured track irregularities with slab; (3) Response to ISO C-Road Class

represent the output voltage of the training FLC in the time steps when the inputs of the trained controlled are at the desired combination. The activated output class is simply obtained by averaging the value of such points. In most of the cases, this procedure will render a quite narrow distribution of points that can univocally lead to a rule to activated, like shown in the figure. However, there are three different possibilities.

1. The set of points is collected in a narrow band and the output class can be reliably identified (case in figure);

2. The set of points produces a certain average but its distribution is very wide,

in such case one must take care of that rule and flag it in case the table of rules needs optimization

3. The input combination does not find any correspondence in the training simulation, meaning that there is no points to average. In this case, one may choose a rule trying again to understand the physics of the corresponding combination of states risking to completely detach from the learned logic and to produce an outlying rule, or, one can place the rule trying to find a pattern between the neighboring ones.

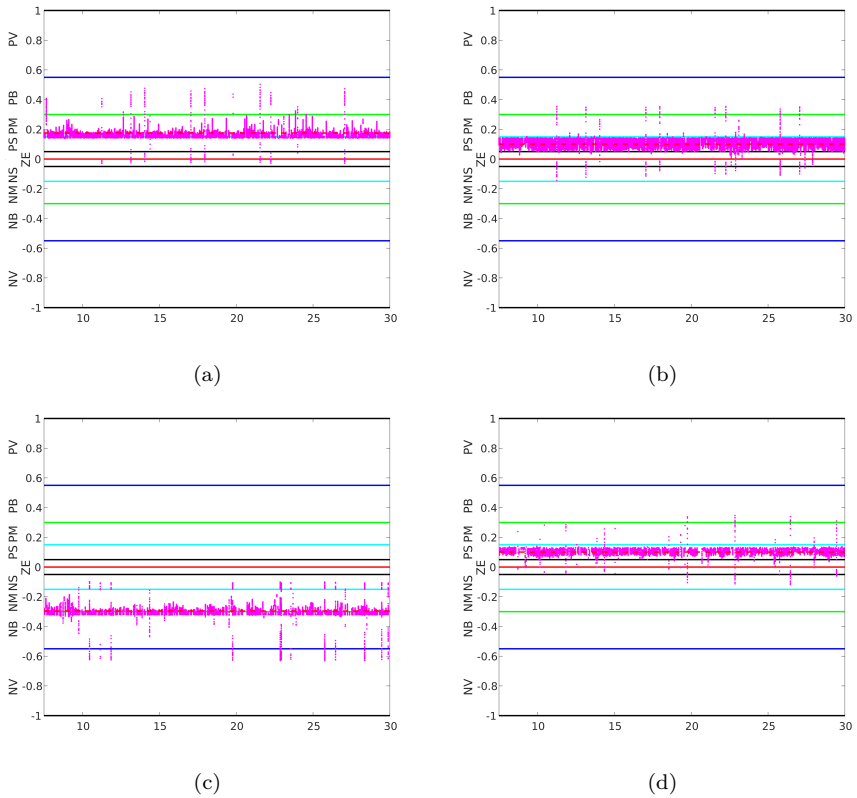

Figure 6.40: Training sets. They show the control action of the training surface during the training simulation in all of the trained surface input combinations (only 4 out of 125 are shown). There is a training set plot for each trained system rule.

The definition of a right disturbance in the training simulation is crucial and it must be chaotic enough to activate all possible combinations of inputs. For this reason a configuration of both track, slab and random irregularities was chosen to excite the system with various magnitudes and frequencies. An extract from the resulting table is reported here below. One can notice that the combination of inputs corresponding to rule '81' wasn't found in the training time simulation. The

best approach is to look at the neighboring rules from rule 82 to rule 85, where just the $\ddot{z}_{us}$ class changes, and it emerges that while $\ddot{z}_{us}$ grows from NS to PM, the output voltage goes from PM to NB. Therefore, one can confidently assume that rule 81 should have a PB as an actuation voltage to follow the same trend.

...

"78 - If $\ddot{z}_{us}$ is ZE and v_{rel} is NB and $\ddot{z}_s$ is PS, then the output V is NS"

"79 - If $\ddot{z}_{us}$ is PS and v_{rel} is NB and $\ddot{z}_s$ is PS, then the output V is NM"

"80 - If $\ddot{z}_{us}$ is PB and v_{rel} is NB and $\ddot{z}_s$ is PS, then the output V is NB"

"81 - If $\ddot{z}_{us}$ is NB and v_{rel} is NS and $\ddot{z}_s$ is PS, RULE NOT FOUND"

"82 - If $\ddot{z}_{us}$ is NS and v_{rel} is NS and $\ddot{z}_s$ is PS, then the output V is PM"

"83 - If $\ddot{z}_{us}$ is ZE and v_{rel} is NS and $\ddot{z}_s$ is PS, then the output V is NS"

"84 - If $\ddot{z}_{us}$ is PS and v_{rel} is NS and $\ddot{z}_s$ is PS, then the output V is NM"

"85 - If $\ddot{z}_{us}$ is PM and v_{rel} is NS and $\ddot{z}_s$ is PS, then the output V is NB"

...

It may also happen that one or some of the rules are completely wrong. Saying that a rule is "wrong" means either one of the following two cases:

1. The applied rule produces a control force with the right direction but not with the right magnitude to reduce the body acceleration (for instance the control voltage is PS instead of PV)

2. The applied rule can produce a control force in the wrong direction.

Relentless, the second scenario produces much worse results since the wrong direction of the control force enhances the oscillatory phenomena, going against the final task of improving comfort.

After having filled the table of rules, thus, a fast check on, at least, the control force sign must be made. In the case in example, during this second cross check, one would notice that the extrapolated rule 81 is actually "wrong" as it provides a PB voltage when the sprung mass acceleration is already PS, thus the control voltage is going to have a destabilizing effect if the rule is not changed. For this reason rule 81 is changed again to NM in order to contrast the sprung mass acceleration.

Mistakes in magnitude of the rules are much less relevant than those in sign since the normalizer logic can compensate for insufficient control force by increasing the dynamic gain.

The presence of "wrong" rules in the inference system can easily be spotted by increasing the static gain. As mentioned in the previous paragraphs, the static

gain statically scales the output of the fuzzy controller in order to give it enough "strength" to be able to impact the system's performance. When a wrong rule is fired and a very high static gain is applied, the single rule is able to destabilize the system and can be easily spotted by looking for the corresponding states of the inputs. This behavior can results in a sort of Self-Induced Instability.

6.9.2 Self Induced Instability

An independent subsection is dedicated to this phenomenon as it is a crucial event to understand. When a bad table of rules is defined the controller can easily bring the system into instability. The application of a wrong rule can produce a destabilizing force that produces strong and sudden variations in acceleration. The controller "is not aware" that such behaviors are provoked by itself and it "thinks" they come from external disturbances. The normalizer, detecting changes in acceleration magnitude, responds by increasing the dynamic gain. However, this poses an issue: if the input states once again fall within the range associated to incorrect rule/s, the controller enforces the wrong control action with an even greater strength, resulting in an even worse effect than before. This chain of events repeats cyclically and the system becomes unstable.

If the wrong rules are not so many, it is likely that the system will face phases of high response that then elapse due to the effects of neighboring correct rules.

An example of this behavior is displayed in Figure 6.41 where the system passes from a good controlled response to very high acceleration phases at around 2.45s and 2.84s.

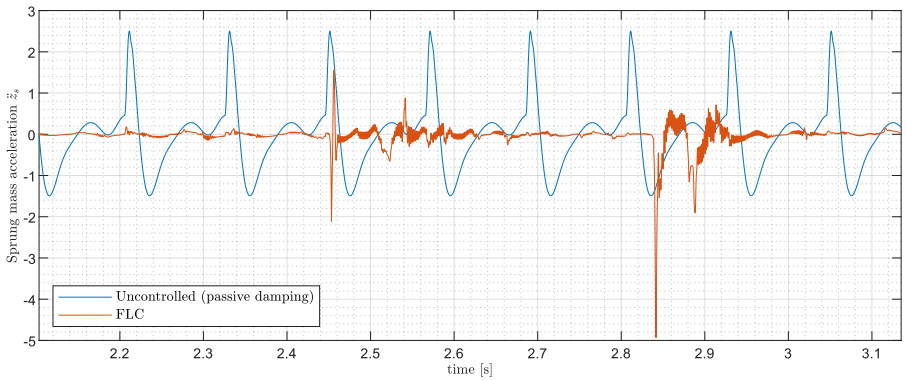

Figure 6.41: Destabilizing effect of wrong rules, at around 2.45s and 2.84s the acceleration response suffers the action of wrong rules

6.9.3 Results

The previous sections about trained inference systems served to highlight the hypothesis at the base of the approach and to discuss possible sources of errors and ways of spotting them. In this section, the trained inference system, starting from the Jerk-Acceleration control surface, is reported. Figure 6.42 shows the

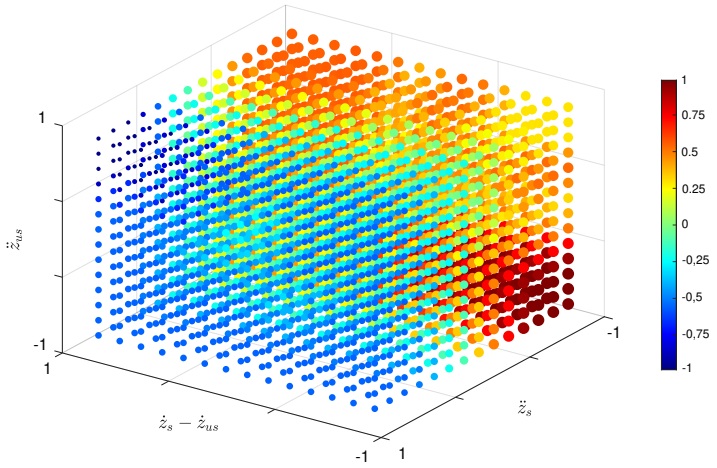

Figure 6.42: 4D control surface trained by 3D Jerk-Acceleration control surface

scatter plot representing the 4-D control surface working with input sprung and unsprung mass acceleration and relative velocity. Notice the substantial difference between this control surface and the one obtained by human logic in Figure 6.34. The results of 4D control surface will be reported in a different fashion as the comparison between response and control voltage of the trainer and trained signals are highlighted. The improvement in response will be again evaluated by the RMS ratio between the uncontrolled and controlled behavior. The zoomed view on the controlled response and control voltage of the electrodynamic system to track irregularities, track irregularities and slab and ISO C road class, are reported in Figures 6.43, 6.44, 6.45 respectively. The plots contain the data of the training system behavior and of the trained system behavior, while Table 6.6 contains the RMS ratios of all the analyzed control surfaces.

Remarkably, the approach proves to give advantages since, for every investigated case, the 4D trained surface provided better performance of the 2D user defined surface. The response of the trained system is not as good as that of the 3D trainer one. However, the result is indeed very promising as it allows to get very good control performance also by reducing user dependency.

RMS ratios	3D Rel.Speed and Acc.	3D Jerk and Acc.	4D by Logic	4D Surf. Trained
Track irregularities	20.1	47.1	15.5	25.2
Track irr. and slab	24.0	56.1	17.0	29.3
ISO C Road Class	6.87	9.50	5.2	8.2

Table 6.6: Comparison of the results with different control surfaces. From left to right: (1) 3D control surface derived with human logic; (2) 3D control surface with Jerk and acceleration derived; (3) 4D control surface with input sprung and unsprung mass acceleration and relative speed derived with human logic; (4) 4D control surface with input sprung and unsprung mass acceleration and relative speed trained by Jerk and acceleration 3D control surface.

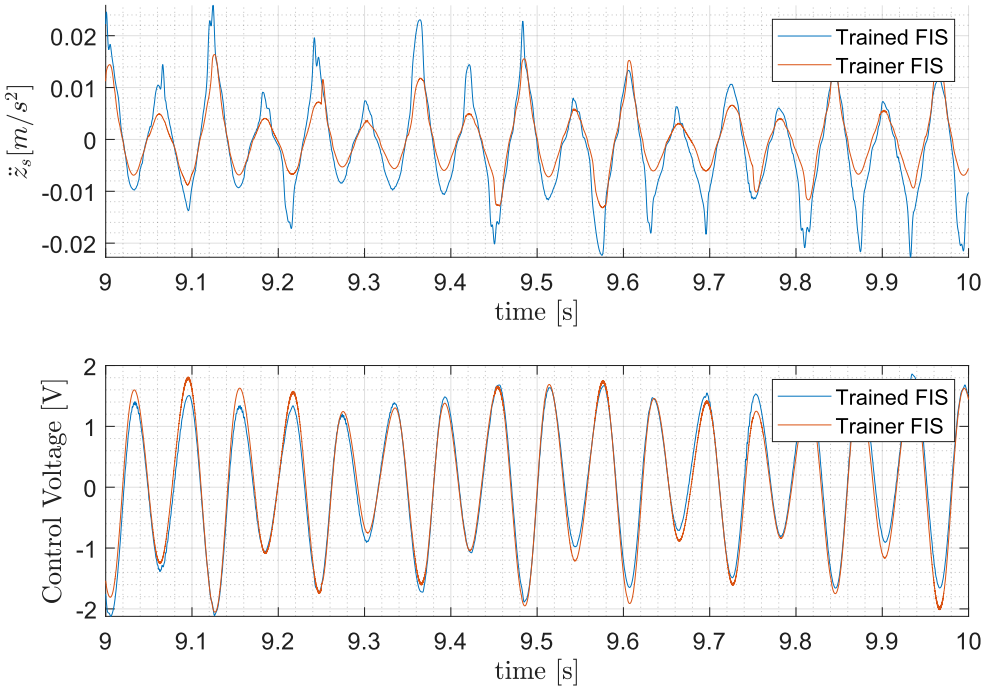

Figure 6.43: (top) Acceleration response of the sprung mass to input track irregularities for the controlled with Jerk-Acceleration trainer surface (orange) and controlled with 4D trained surface (blue); (bottom) Trainer (orange) vs trained (blue) control voltage

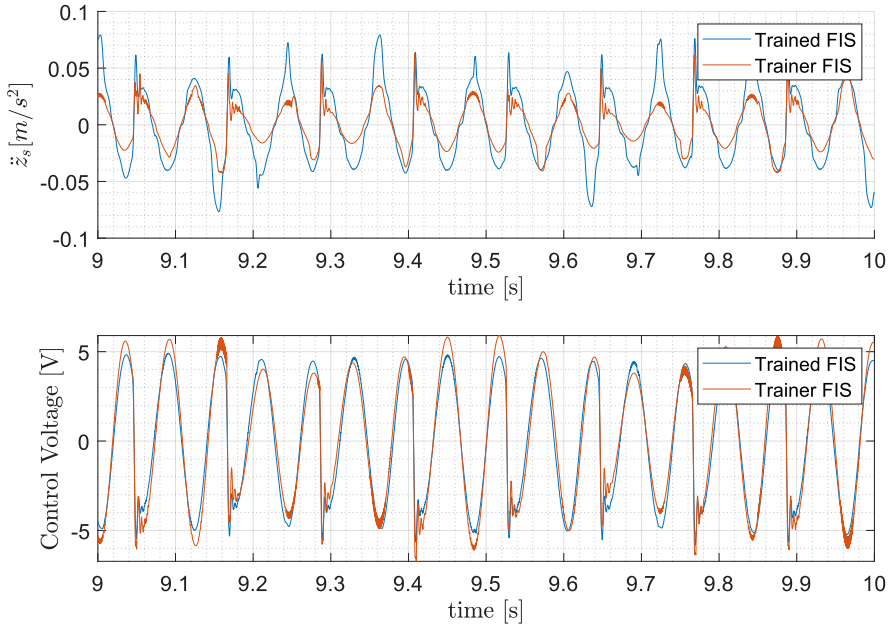

Figure 6.44: (top) Acceleration response of the sprung mass to input track irregularities and slab for the controlled with Jerk-Acceleration trainer surface (orange) and controlled with 4D trained surface (blue); (bottom) Trainer (orange) vs trained (blue) control voltage

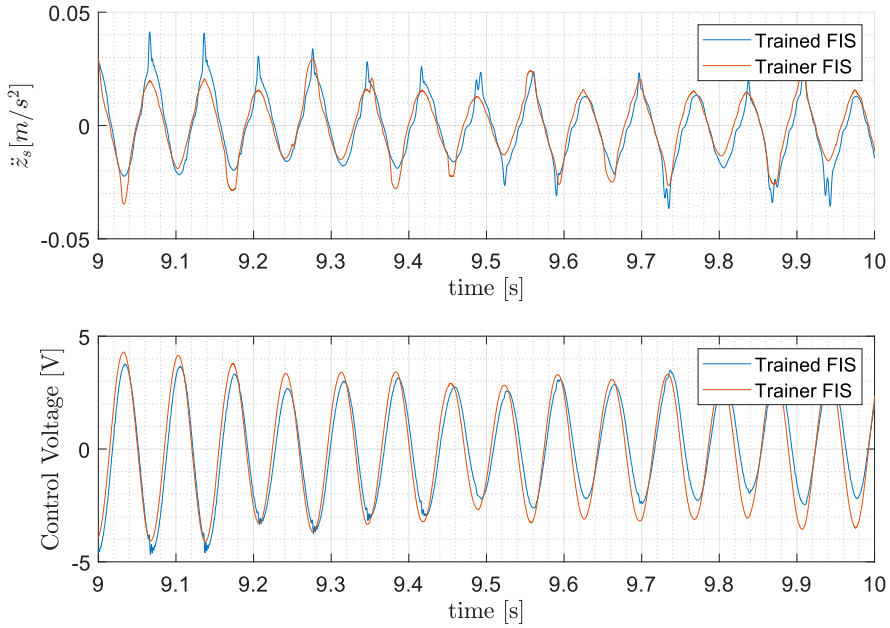

Figure 6.45: (top) Acceleration response of the sprung mass to input ISO C road class for the controlled with Jerk-Acceleration trainer surface (orange) and controlled with 4D trained surface (blue); (bottom) Trainer (orange) vs trained (blue) control voltage

Chapter 7

Final Remarks

7.1 Conclusions

This thesis work has covered the dynamic analysis, state estimation and Fuzzy logic control of an existing electrodynamic levitation test bench.

Dynamic analysis was performed using the classical dynamic tools in order to highlight the system's stability and its behavior when varying some of the major parameters. Parametric systems root loci plots, sensitivity analyses and frequency response functions were broadly discussed to depict an image of the system's dynamic identity. A feedback line was set up to mimic the effect of an additional damper between the two masses.

A further section dealt with developing a reduced order model, good enough to work inside of a Kalman Filter. The development of a Kalman Filter was necessary to produce an estimate of the relative velocity as it is not a measured state and it is needed for the task of controlling the system.

An adaptive rule-based controller working with fuzzy logic was proposed in order to improve passenger comfort within the sprung mass. The development of such controller required the implementation of an auxiliary block which was called "normalizer" that performs the task of adapting the controller rules to the magnitude of the phenomena.

At last, an approach was presented, yielding the possibility to start with reliable and easy to obtain tables of rules and to translate their control logic in other tables of rules working with different and more inputs. This approach goes in the direction of reducing the dependency of the controller from the designer's choice.

On an overall, reducing the arbitrary choices was a main target throughout the work. When choosing "accepted" fuzzy sets to classify inputs, or when reducing the number of membership functions to the minimum possible, as well as when the trainer/trained system approach was proposed, the idea was always that of

reducing the arbitrariness of the choices in order to have a more reliable controller configuration.

At the end there are, of course, still a few arbitrary parameters that must be set by the designer based on his expertise and trial and errors attempts.

The main aspects that can vary if the same controller is used in different systems, apart from the table of rules, are the Normalization Period as well as the tunable static gain value. Normalizer period has always been set to a constant since, in the whole work, the controller was applied to phenomena of similar frequencies. If the frequency of excitation was to be much higher, one should think about reducing the normalization period in order to have a more accurate depiction of the magnitude of the phenomenon. Another aspect about the normalizer concerns update time duration with respect to the normalization period that, in this work, was set to the 50% as a result of trial and error optimization.

Regarding the tunable static gain, its value has been proven to be quite easy to optimize.

7.2 Further work

There are many further margins of optimization for the proposed fuzzy logic approach.

The control strategy can be tested on many other systems to check its versatility and the user-friendliness. It is mostly important to evaluate the quantity of variations that must be done to adapt it to completely different systems.

Also, in this case, the controlled system was a quite simple quarter car model for which it is easy to schedule reliable rules. The application of rules should be tested on more complex systems.

Furthermore, a possible algorithm could be developed to allow for a self tuning of the normalization period. One can notice that, if the normalization period is very short, with respect to the period of the input wave, the normalized wave tends to a square wave ranging from -1 to 1. This fact can be used as a starting point for normalizer period scheduling.

Finally, other work can be made on the trainer/trained fuzzy logic controller approach, finding any other more optimized ways to classify inputs and outputs by even inverting the inference system if possible.

Trying to use the training algorithm to mimic the behavior of completely different kinds of controllers can produce a further proof of the efficacy of the approach.

Appendix A

Matrices

A.1 State space matrices of passive 1dof Electrodynamically levitated system

State space matrices of a 1 degree of freedom levitated system containing the electrical subsystem of the track. Used for the preliminary stability analysis of an electrodynamically levitated body.

$$\mathbf{z} = \begin{bmatrix} i_{d,1} & i_{q,1} & i_{d,2} & i_{q,2} & z_{in} & \dot{z}_{pm} & z_{pm} \end{bmatrix}^\top$$

$$\mathbf{y} = \begin{bmatrix} \ddot{z}_{pm} \end{bmatrix}^\top$$

$$\mathbf{u} = \begin{bmatrix} \dot{z}_{in} & f_{pm} \end{bmatrix}^\top$$

$$C_1 = \frac{\Lambda_0}{\gamma} e^{-z_{p,0}/\gamma}$$

$$\boldsymbol{A_{EDS}} = \begin{bmatrix} -\omega_{p,1} & \omega & 0 & 0 & 0 & \frac{C_1}{L_1} & 0 \\ -\omega & -\omega_{p,1} & 0 & 0 & -\omega\frac{C_1}{L_1} & 0 & \omega\frac{C_1}{L_1} \\ 0 & 0 & -\omega_{p,2} & \omega & 0 & \frac{C_1}{L_2} & 0 \\ 0 & 0 & -\omega & -\omega_{p,2} & -\omega\frac{C_1}{L_2} & 0 & \omega\frac{C_1}{L_2} \\ 0 & 0 & 0 & 0 & 0 & 0 & 0 \\ -\frac{2C_1}{m_0} & 0 & -\frac{2C_1}{m_0} & 0 & 0 & 0 & 0 \\ 0 & 0 & 0 & 0 & 0 & 1 & 0 \end{bmatrix}$$

$$\boldsymbol{B_{EDS}} = \begin{bmatrix} -\frac{C_1}{L_1} & 0 & -\frac{C_1}{L_2} & 0 & 1 & 0 & 0 \\ 0 & 0 & 0 & 0 & 0 & \frac{1}{m_0} & 0 \end{bmatrix}^\top$$

$$\boldsymbol{C_{EDS}} = \begin{bmatrix} 2\frac{C_1}{m_0} & 0 & -2\frac{C_1}{m_0} & 0 & 0 & 0 & 0 \end{bmatrix}$$

$$\boldsymbol{D_{EDS}} = \begin{bmatrix} 0 & 1/m_0 \end{bmatrix}^\top$$

A.2 Auxiliary state space matrices for the dynamic measuring device mechanical subsystem

Matrices used for the assembly of the full model. They represent the mechanical subsystem of the measuring device. They are composed with the 1dof levitated body to enrich the mechanical domain with levitation dynamics.

$$\mathbf{z} = \begin{bmatrix} \dot{z}_{us} & z_{us} & \dot{z}_s & z_s & i_{vc} \end{bmatrix}^\top$$

$$\mathbf{u} = \begin{bmatrix} f_{us} & f_s & V \end{bmatrix}^\top$$

$$\boldsymbol{A_M} = \begin{bmatrix} -\frac{c_{vc}+c_{us}}{m_{us}} & -\frac{k_s+k_{us}}{m_{us}} & \frac{c_{vc}}{m_{us}} & \frac{k_s}{mus} & -\frac{K_m}{m_{us}} \\ 1 & 0 & 0 & 0 & 0 \\ \frac{c_{vc}}{m_s} & \frac{k_s}{m_s} & -\frac{c_{vc}}{m_s} & -\frac{k_s}{m_s} & \frac{K_m}{m_s} \\ 0 & 0 & 1 & 0 & 0 \\ \frac{K_m}{L_{vc}} & 0 & -\frac{K_m}{L_{vc}} & 0 & -\frac{R_{vc}}{L_{vc}} \end{bmatrix}$$

$$\boldsymbol{B_M} = \begin{bmatrix} \frac{1}{m_{us}} & 0 & 0 & 0 & 0 \\ 0 & 0 & \frac{1}{m_s} & 0 & 0 \\ 0 & 0 & 0 & 0 & \frac{1}{L_{vc}} \end{bmatrix}^\top$$

A.3 Full model matrices

Matrices describing the full system. They comprise the voice coil domain, the mechanical domain as well as a two branched electrical subsystem for levitation dynamics.

$$\boldsymbol{z_{full}} = \begin{bmatrix} i_{1,d} & i_{1,q} & i_{2,d} & i_{2,q} & z_{in} & \dot{z}_{us} & z_{us} & \dot{z}_s & z_s & i_{vc} \end{bmatrix}^\top$$

$$\boldsymbol{u_{full}} = \begin{bmatrix} \dot{z}_{in} & f_{us} & f_s & V \end{bmatrix}^\top$$

$$\boldsymbol{y_{full}} = \begin{bmatrix} \ddot{z}_{us} & \ddot{z}_s & i_{vc} \end{bmatrix}^\top$$

$$\boldsymbol{A_{full}} = \begin{bmatrix} -\omega_{p,1} & \omega & 0 & 0 & 0 & \frac{C_1}{L_1} & 0 & 0 & 0 & 0 \\ -\omega & -\omega_{p,1} & 0 & 0 & -\omega\frac{C_1}{L_1} & 0 & \omega\frac{C_1}{L_1} & 0 & 0 & 0 \\ 0 & 0 & -\omega_{p,2} & \omega & 0 & \frac{C_1}{L_2} & 0 & 0 & 0 & 0 \\ 0 & 0 & -\omega & -\omega_{p,2} & -\omega\frac{C_1}{L_2} & 0 & \omega\frac{C_1}{L_2} & 0 & 0 & 0 \\ 0 & 0 & 0 & 0 & 0 & 0 & 0 & 0 & 0 & 0 \\ -\frac{2C_1}{m_0} & 0 & -\frac{2C_1}{m_0} & 0 & 0 & -\frac{c_{vc}+c_{us}}{m_{us}} & -\frac{k_s+k_{us}}{m_{us}} & \frac{c_{vc}}{m_{us}} & \frac{k_s}{mus} & -\frac{K_m}{m_{us}} \\ 0 & 0 & 0 & 0 & 0 & 1 & 0 & 0 & 0 & 0 \\ 0 & 0 & 0 & 0 & 0 & \frac{c_{vc}}{m_s} & \frac{k_s}{m_s} & -\frac{c_{vc}}{m_s} & -\frac{k_s}{m_s} & \frac{K_m}{m_s} \\ 0 & 0 & 0 & 0 & 0 & 0 & 0 & 1 & 0 & 0 \\ 0 & 0 & 0 & 0 & 0 & \frac{K_m}{L_{vc}} & 0 & -\frac{K_m}{L_{vc}} & 0 & -\frac{R_{vc}}{L_{vc}} \end{bmatrix}$$

$$\boldsymbol{B_{full}} = \begin{bmatrix} -\frac{C_1}{L_1} & 0 & -\frac{C_1}{L_2} & 0 & 1 & 0 & 0 & 0 & 0 & 0 \\ 0 & 0 & 0 & 0 & 0 & \frac{1}{m_{us}} & 0 & 0 & 0 & 0 \\ 0 & 0 & 0 & 0 & 0 & 0 & 0 & \frac{1}{m_s} & 0 & 0 \\ 0 & 0 & 0 & 0 & 0 & 0 & 0 & 0 & 0 & \frac{1}{L_{vc}} \end{bmatrix}^\top$$

$$\boldsymbol{C_{full}} = \begin{bmatrix} -\frac{2C_1}{m_0} & 0 & -\frac{2C_1}{m_0} & 0 & 0 & -\frac{c_{vc}+c_{us}}{m_{us}} & -\frac{k_s+k_{us}}{m_{us}} & \frac{c_{vc}}{m_{us}} & \frac{k_s}{mus} & -\frac{K_m}{m_{us}} \\ 0 & 0 & 0 & 0 & 0 & \frac{c_{vc}}{m_s} & \frac{k_s}{m_s} & -\frac{c_{vc}}{m_s} & -\frac{k_s}{m_s} & \frac{K_m}{m_s} \\ 0 & 0 & 0 & 0 & 0 & 0 & 0 & 0 & 0 & 1 \end{bmatrix}^\top$$

$$\boldsymbol{D_{full}} = \begin{bmatrix} 0 & \frac{1}{m_{us}} & 0 & 0 \\ 0 & 0 & \frac{1}{m_s} & 0 \\ 0 & 0 & 0 & 0 \end{bmatrix}$$

A.4 Reduced model matrices

Reduced matrices contain the mechanical and voice coil domain but do not encompass levitation dynamics, in fact, the 4 equations related to the in phase and quadrature current component are cancelled. The contribution of electrodynamic levitation is accounted for with an equivalent spring of stiffness k_p. This system is used for states estimation in the Kalman filter.

$$\boldsymbol{z_{red}} = \begin{bmatrix} z_{in} & \dot{z}_{us} & z_{us} & \dot{z}_s & z_s & i_{vc} \end{bmatrix}^\top$$

$$\boldsymbol{u_{red}} = \begin{bmatrix} \dot{z}_{in} & f_{us} & f_s & V \end{bmatrix}^\top$$

$$\boldsymbol{y_{red}} = \begin{bmatrix} \ddot{z}_{us} & \ddot{z}_s & i_{vc} \end{bmatrix}^\top$$

$$\boldsymbol{A_{red}} = \begin{bmatrix} 0 & 0 & 0 & 0 & 0 & 0 \\ \frac{k_p}{m_{us}} & -\frac{c_{vc}+c_{us}}{m_{us}} & -\frac{k_s+k_{us}}{m_{us}} & \frac{c_{vc}}{m_{us}} & \frac{k_s}{mus} & -\frac{K_m}{m_{us}} \\ 0 & 1 & 0 & 0 & 0 & 0 \\ 0 & \frac{c_{vc}}{m_s} & \frac{k_s}{m_s} & -\frac{c_{vc}}{m_s} & -\frac{k_s}{m_s} & \frac{K_m}{m_s} \\ 0 & 0 & 0 & 1 & 0 & 0 \\ 0 & \frac{K_m}{L_{vc}} & 0 & -\frac{K_m}{L_{vc}} & 0 & -\frac{R_{vc}}{L_{vc}} \end{bmatrix}$$

$$\boldsymbol{B_{red}} = \begin{bmatrix} 1 & 0 & 0 & 0 & 0 & 0 \\ 0 & \frac{1}{m_{us}} & 0 & 0 & 0 & 0 \\ 0 & 0 & 0 & \frac{1}{m_s} & 0 & 0 \\ 0 & 0 & 0 & 0 & 0 & \frac{1}{L_{vc}} \end{bmatrix}^\top$$

$$\boldsymbol{C_{red}} = \begin{bmatrix} \frac{k_p}{m_{us}} & -\frac{c_{vc}+c_{us}}{m_{us}} & -\frac{k_s+k_{us}}{m_{us}} & \frac{c_{vc}}{m_{us}} & \frac{k_s}{mus} & -\frac{K_m}{m_{us}} \\ 0 & \frac{c_{vc}}{m_s} & \frac{k_s}{m_s} & -\frac{c_{vc}}{m_s} & -\frac{k_s}{m_s} & \frac{K_m}{m_s} \\ 0 & 0 & 0 & 0 & 0 & 1 \end{bmatrix}$$

$$\boldsymbol{D_{red}} = \begin{bmatrix} 0 & \frac{1}{m_{us}} & 0 & 0 \\ 0 & 0 & \frac{1}{m_s} & 0 \\ 0 & 0 & 0 & 0 \end{bmatrix}$$

A.5 Modified Full model

Modified Full model matrices used for Kalman filtering implementation and FRFs. They contain the same information as the full model matrices but z_{in} is moved from the states vector to the input vector.

$$\boldsymbol{z_{fuld}} = \begin{bmatrix} i_{1,d} & i_{1,q} & i_{2,d} & i_{2,q} & \dot{z}_{us} & z_{us} & \dot{z}_s & z_s & i_{vc} \end{bmatrix}^\top$$

$$\boldsymbol{u_{fuld}} = \begin{bmatrix} z_{in} & \dot{z}_{in} & f_{us} & f_s & V \end{bmatrix}^\top$$

$$\boldsymbol{y_{fuld}} = \begin{bmatrix} \ddot{z}_{us} & \ddot{z}_s & i_{vc} \end{bmatrix}^\top$$

$$\boldsymbol{A_{fuld}} = \begin{bmatrix} \text{-}\omega_{p,1} & \omega & 0 & 0 & \frac{C_1}{L_1} & 0 & 0 & 0 & 0 \\ \text{-}\omega & \text{-}\omega_{p,1} & 0 & 0 & 0 & \omega\frac{C_1}{L_1} & 0 & 0 & 0 \\ 0 & 0 & \text{-}\omega_{p,2} & \omega & \frac{C_1}{L_2} & 0 & 0 & 0 & 0 \\ 0 & 0 & \text{-}\omega & \text{-}\omega_{p,2} & 0 & \omega\frac{C_1}{L_2} & 0 & 0 & 0 \\ \text{-}\frac{2C_1}{m_0} & 0 & \text{-}\frac{2C_1}{m_0} & 0 & \text{-}\frac{c_{vc}+c_{us}}{m_{us}} & \text{-}\frac{k_s+k_{us}}{m_{us}} & \frac{c_{vc}}{m_{us}} & \frac{k_s}{mus} & \text{-}\frac{K_m}{m_{us}} \\ 0 & 0 & 0 & 0 & 1 & 0 & 0 & 0 & 0 \\ 0 & 0 & 0 & 0 & \frac{c_{vc}}{m_s} & \frac{k_s}{m_s} & \text{-}\frac{c_{vc}}{m_s} & \text{-}\frac{k_s}{m_s} & \frac{K_m}{m_s} \\ 0 & 0 & 0 & 0 & 0 & 0 & 1 & 0 & 0 \\ 0 & 0 & 0 & 0 & \frac{K_m}{L_{vc}} & 0 & \text{-}\frac{K_m}{L_{vc}} & 0 & \text{-}\frac{R_{vc}}{L_{vc}} \end{bmatrix}$$

$$\boldsymbol{B_{fuld}} = \begin{bmatrix} 0 & \text{-}\omega\frac{C_1}{L_1} & 0 & \text{-}\omega\frac{C_1}{L_2} & 0 & 0 & 0 & 0 & 0 \\ -\frac{C_1}{L_1} & 0 & -\frac{C_1}{L_2} & 0 & 0 & 0 & 0 & 0 & 0 \\ 0 & 0 & 0 & 0 & \frac{1}{m_{us}} & 0 & 0 & 0 & 0 \\ 0 & 0 & 0 & 0 & 0 & 0 & \frac{1}{m_s} & 0 & 0 \\ 0 & 0 & 0 & 0 & 0 & 0 & 0 & 0 & \frac{1}{L_{vc}} \end{bmatrix}^\top$$

$$\boldsymbol{C_{fuld}} = \begin{bmatrix} \text{-}\frac{2C_1}{m_0} & 0 & \text{-}\frac{2C_1}{m_0} & 0 & \text{-}\frac{c_{vc}+c_{us}}{m_{us}} & \text{-}\frac{k_s+k_{us}}{m_{us}} & \frac{c_{vc}}{m_{us}} & \frac{k_s}{mus} & \text{-}\frac{K_m}{m_{us}} \\ 0 & 0 & 0 & 0 & \frac{c_{vc}}{m_s} & \frac{k_s}{m_s} & \text{-}\frac{c_{vc}}{m_s} & \text{-}\frac{k_s}{m_s} & \frac{K_m}{m_s} \\ 0 & 0 & 0 & 0 & 0 & 0 & 0 & 0 & 1 \end{bmatrix}$$

$$\boldsymbol{D_{fuld}} = \begin{bmatrix} 0 & 0 & \frac{1}{m_{us}} & 0 & 0 \\ 0 & 0 & 0 & \frac{1}{m_s} & 0 \\ 0 & 0 & 0 & 0 & 0 \end{bmatrix}$$

A.6 Modified reduced model matrices

This matrices contain the reduced version of the modified full model they were discretized and utilized for estimation in the kalman filter.

$$\boldsymbol{z_{redd}} = \begin{bmatrix} \dot{z}_{us} & z_{us} & \dot{z}_s & z_s & i_{vc} \end{bmatrix}^\top$$

$$\boldsymbol{u_{redd}} = \begin{bmatrix} z_{in} & f_{us} & f_s & V \end{bmatrix}^\top$$

$$\boldsymbol{y_{redd}} = \begin{bmatrix} \ddot{z}_{us} & \ddot{z}_s & i_{vc} \end{bmatrix}^\top$$

$$\boldsymbol{A_{redd}} = \begin{bmatrix} \text{-}\frac{c_{vc}+c_{us}}{m_{us}} & \text{-}\frac{k_s+k_{us}}{m_{us}} & \frac{c_{vc}}{m_{us}} & \frac{k_s}{mus} & \text{-}\frac{K_m}{m_{us}} \\ 1 & 0 & 0 & 0 & 0 \\ \frac{c_{vc}}{m_s} & \frac{k_s}{m_s} & \text{-}\frac{c_{vc}}{m_s} & \text{-}\frac{k_s}{m_s} & \frac{K_m}{m_s} \\ 0 & 0 & 1 & 0 & 0 \\ \frac{K_m}{L_{vc}} & 0 & \text{-}\frac{K_m}{L_{vc}} & 0 & \text{-}\frac{R_{vc}}{L_{vc}} \end{bmatrix}$$

$$\boldsymbol{B_{redd}} = \begin{bmatrix} \frac{k_p}{m_{us}} & 0 & 0 & 0 & 0 \\ 0 & 0 & 0 & 0 & 0 \\ \frac{1}{m_{us}} & 0 & 0 & 0 & 0 \\ 0 & 0 & \frac{1}{m_s} & 0 & 0 \\ 0 & 0 & 0 & 0 & \frac{1}{L_{vc}} \end{bmatrix}^\top$$

$$\boldsymbol{C_{red}} = \begin{bmatrix} -\frac{c_{vc}+c_{us}}{m_{us}} & -\frac{k_s+k_{us}}{m_{us}} & \frac{c_{vc}}{m_{us}} & \frac{k_s}{mus} & -\frac{K_m}{m_{us}} \\ \frac{c_{vc}}{m_s} & \frac{k_s}{m_s} & -\frac{c_{vc}}{m_s} & -\frac{k_s}{m_s} & \frac{K_m}{m_s} \\ 0 & 0 & 0 & 0 & 1 \end{bmatrix}$$

$$\boldsymbol{D_{redd}} = \begin{bmatrix} \frac{k_p}{m_{us}} & 0 & \frac{1}{m_{us}} & 0 & 0 \\ 0 & 0 & 0 & \frac{1}{m_s} & 0 \\ 0 & 0 & 0 & 0 & 0 \end{bmatrix}$$

Bibliography

[1] Kemal Armagan. «The fifth mode of transportation: Hyperloop». In: *IEEE Transactions on Applied Superconductivity* (Nov. 2020) (cit. on p. 1).

[2] Ju Lee Hyung-Woo Lee Ki-Chan Kim. «Review of Maglev Train technology». In: *Korea Railroad Research institute* (2002), pp. 185–210 (cit. on pp. 5–8).

[3] R. Galluzzi, S. Circosta, N. Amati, A. Tonoli, A. Bonfitto, T. A. Lembke, and M. Kertész. «Multi-domain Approach to the Stabilization of Electrodynamic Levitation Systems». In: *ASME: Journal of Vibration and Acoustics* Vol. 142 (Dec. 2020) (cit. on pp. 11, 16, 17, 21, 24, 31).

[4] N.Amati. «Modeling and experimental validation of electrodynamic maglev systems». In: *Journal of Sound and Vibration* (Jul 2023) (cit. on p. 11).

[5] Lorenzo Bosica. «Modeling and Identification of an Experimental Test Bench for the study of Electrodynamic Phenomena». In: (Dec. 2022) (cit. on pp. 14, 17, 25, 28, 31).

[6] Andrea Bo. «Modeling, control and characterization of an electrodynamic levitation test bench, Politecnico di Torino Master's Thesis». In: (July 2022) (cit. on p. 25).

[7] Arianna Conchin Gubernati. «Experimental test bench for electrodynamic levitation system characterization, Politecnico di Torino Master's Thesis». In: (July 2022) (cit. on p. 25).

[8] Kollmorgen. «Kollmorgen AKM Servo Motor selection guide www.kollmorgen.com/sites/default/files/Kollmorgen_AKM_Servomotor_Selection_Guide.pdf». In: () (cit. on p. 26).

[9] Marius PAKŠTYS. «A Study and Implementation of Stability in Electrodynamic Levitation Systems». In: (Oct. 2022) (cit. on pp. 27, 28, 104).

[10] Geeplus. «Geeplus technical library, Characteristics and Selection of Voice Coil Motors www.geeplus.com/characteristics-and-selection-of-voice-coil-motors/». In: () (cit. on p. 32).

[11] Geeplus. «Geeplus VM108-2P30 www.geeplus.com/wp-content/uploads/2019/08/Voice_Coil_motor_VM108-2P30.pdf». In: () (cit. on pp. 32, 34).

[12] Marchesiello S. Fasana A. «Meccanica delle vibrazioni». In: () (cit. on p. 37).

[13] R. E. Kalman. «A New Approach to Linear Filtering and Prediction Problems». In: *ASME–Journal of Basic Engineering, 82D* (Mar 1960) (cit. on pp. 63, 66).

[14] R. Faragher. «Understanding the Basis of the Kalman Filter Via a Simple and Intuitive Derivation». In: *IEEE Signal Processing Magazin 128* (Sep 2012) (cit. on p. 63).

[15] Viktorov V. Colombo F. «Automation of Mechanical systems». In: () (cit. on pp. 81–83).

[16] J.J.Robert. «Fuzzy control of active suspension system based on quarter car model». In: *Materialstoday:Proceedings* (Apr 2012) (cit. on p. 85).

[17] M. M. M. Salem and Ayman A. Aly. «Fuzzy Control of a Quarter-Car Suspension System». In: *International Science Index, Computer and Information Engineering Vol:3, No:5,* (2009) (cit. on p. 85).

[18] A. A. Castro G. Rill. *Road Vehicle Dynamics: Fundamentals and Modeling with MATLAB*. CRC Press, 2022 (cit. on p. 104).

[19] H. Eric Tseng Davor Hrovat. «State of the art survey: active and semi-active suspension control». In: *Journal of Vehicle Mechanics and Mobility* (May 2015).

[20] K.R. Borole M.P. Nagarkar G.J. Vikhe and V.M Nandedkar. «Active control of Quarter-Car suspension system using linear quadratic regulator». In: *International Journal of Automotive and Mechanical Engineering (IJAME)* (2011).

[21] M. Senthil Kumar and S. Vijayarangan. «Linear quadratic regulator controller design for active suspension system subjected to random road surfaces». In: *Journal of Scientific and Industrial Research* (Mar 2006).

[22] W. F. Wu Y. T. Fan. «Dynamic Analysis and Ride Quality Evaluation of Railway Vehicles - Numerical Simulation and Field Test Verification». In: *Journal of Mechanichs* (Sep 2006).

[23] M. Corno O. Galluppi G. Panzani A. Sinigaglia P. Capuano J. Cecconi S. Savaresi. *Design and Validation of a Full Body Control Semi-Active Suspension Strategy for a Supercar*. Tech. rep. Dipartimento di Elettronica, Informazione e Bioingegneria, Politecnico di Milano and Automobili Lamborghini, 2019.